SYNTHESIS AND MAGNETIC PROPERTIES OF Sn, Mn AND Mg SUBSTITUTED $Fe_xCr_{1.8-x}O_3$ NANO OXIDES

by

Kalengay Mbela

BSc (Hons) (University of Kinshasa), MSc (University of KwaZulu-Natal)

Submitted in fulfilment of the academic requirements for the degree of Doctor of Philosophy in Physics in the School of Chemistry and Physics, University of KwaZulu-Natal Durban, South Africa

May 2016

Abstract

The synthesis, structure characterization and magnetic properties of a series of (Sn, Mn, Mg)$_{0.2}$Fe$_x$Cr$_{1.8-x}$O$_3$ nano oxides have been studied. These alloys series were synthesized at low reaction temperature of about 100 °C using hydrothermal methods. Single-phase hexagonal corrundum structure and nanoparticle structure of the synthesized samples were confirmed by X-ray diffraction (XRD) and transmission electron microscopy (TEM). The refinement of XRD data was performed by Rietveld analysis using a model involving a combination of both interstitial and substitutional Mg^{2+}, Mn^{2+}, and Sn^{4+} ions in octahedral coordination. The structural and magnetic properties of Sn$_{0.2}$Fe$_x$Cr$_{1.8-x}$O$_3$ samples prepared using two different methods are compared. XRD analysis for the samples synthesized in a stirred pressure reactor and in a reflux indicate the basic corundum structure for the compositions. TEM experiment indicate a similar trend for both methods of preparation with a particle size for samples prepared in a pressure reactor slightly reduced compared to that synthesized in a reflux. No appreciable difference was observed on the magnetic properties of the two sets of samples. Particle sizes and chemical disorder are shown to play critical roles in influencing the properties of (Sn, Mn, Mg)$_{0.2}$Fe$_x$Cr$_{1.8-x}$O$_3$ nanomaterials. The ^{57}Fe Mössbauer spectra measured at room temperature are well fitted by two magnetic components that range from two sextets for Fe-rich nanomaterials to two doublets for Cr-rich ones. Increased Cr substitution is associated with increased negative exchange interactions. The analysis of the Mössbauer spectra show evidence of Fe^{3+} ions at lattice sites with and without Cr, Sn, Mn or Mg ion neighbors. The transition from sextets to doublets can also be attributed to increased chemical disorder of Fe^{3+} ions with increase in Cr content. The variation of coercive field with particles size reveals that the coercive field achieves a maximum at a critical particle size. These results show evidence of transformation from multi- to single-domain structures. The investigation of the structure

and magnetic properties of $Mg_{0.2}Fe_xCr_{1.8-x}O_3$ nano oxides confirmed the corundum structure in the alloys system. The interpretation of ZFC and FC magnetization results suggest evidence of spin freezing and this behavior at low temperature appears to be associated with increased magnetic hardness. The magnetic susceptibility at high temperature follow the Curie-Weiss relationship with large negative values of Weiss temperature constant, θ_p = -354 K and -722 K. These large negative values of θ_p are interpreted as a robustness of the antiferromagnetic interactions in this alloy system. The effect of annealing temperature on the exchange bias in $Mg_{0.2}Fe_xCr_{1.8-x}O_3$ was also investigated. The shift of the hysteresis curve along the field axis observed in the magnetization results are interpreted as the exchange bias effect. There is a strong correlation between the exchange bias field H_{EB} and the particle sizes D which leads to a critical particle size at about 33 nm. Finally the results on the structure and magnetic properties of $Mn_{0.2}Fe_xCr_{1.8-x}O_3$ nano oxides suggest that this alloy system is superparamagnetic at room temperature. The exchange bias effect is found to be different to that observed in the $Mg_{0.2}Fe_xCr_{1.8-x}O_3$ alloys. The magnetic susceptibility results follow the Curie-Weiss relationship with a negative Weiss temperature constant θ_p = -175 K, which is relatively small compared to that obtained for the $Mg_{0.2}Fe_xCr_{1.8-x}O_3$ alloys. The small value is interpreted as a weaker antiferromagnetic interaction in the material.

Preface

The experimental work described in this dissertation was carried out in the Condensed Matter Physics Laboratory, School of Chemistry and Physics, Westville Campus, University of KwaZulu-Natal, Durban under the supervision of Dr. Thomas Moyo.

The study represents original work by the author and have not otherwise been submitted in any form for any degree or diploma to any tertiary institution. Where use has been made of the work of others it is duly acknowledged in the text.

Declaration 1 - Plagiarism

I, Kalengay Mbela declare that

1. The research reported in this dissertation, except where otherwise indicated, is my original research.

2. This dissertation has not been submitted for any degree or examination at any university.

3. This dissertation does not contain other person's data, pictures, graphs or other information, unless specifically acknowledged as being sourced from other persons.

4. This dissertation does not contain other persons' writings, unless specifically acknowledged as being sourced from other researchers. When other written sources have been quoted, then:
   (a) Their words have been re-written but general information attributed to them has been referenced.
   (b) Where their exact words have been used, their writing has been placed in italics and inside quotation, and referenced.

5. This dissertation does not contain text, graphics or tables copied and pasted from internet, unless specifically acknowledged, and the source being detailed in the dissertation and in the reference sections.

Signed : ..... Date: 11 May 2016

Declaration 2 - Publications

1. Effects of annealing on exchange bias in $Mg_{0.2}Fe_xCr_{1.8-x}O_3$ compounds prepared via the hydrothermal route, K. Mbela, T. Moyo, S.E Nadir Osman, Journal of Materials Science: Materials in Electronics DOI 10.1007/s10854-016-4919-1 (2016) (Published online 3 May 2016).

2. Magnetic studies of $Mn_{0.2}Fe_xCr_{1.8-x}O_3$ compounds prepared via the hydrothermal route, K. Mbela, T. Moyo, M. Öztürk and N. Akdoǵan, Journal of Materials Science: Materials in Electronics .DOI 10.1007/s10854-016-4953-z (2016) (Published online 11 May 2016).

3. Magnetic studies of $Sn_{0.2}Fe_xCr_{1.8-x}O_3$ compounds prepared via the hydrothermal route, K. Mbela, T. Moyo, J. Z. Msomi, Journal of Magnetism and Magnetic Materials **385** (2015) 282-285.

4. Synthesis and magnetic properties of $Mg_{0.2}Fe_xCr_{1.8-x}O_3$ oxides, K. Mbela, T. Moyo, J. Z. Msomi, in Proceedings of SAIP 2012: the 57th Conference of the South African Institute of Physics, edited by Johan Janse van Rensburg (2014), 120-125. ISBN: 978-1-77592-070-0.

5. Synthesis and magnetic properties of $Mg_{0.2}Fe_xCr_{1.8-x}O_3$ nanoparticles, K. Mbela, T. Moyo, J. Z. Msomi, M. Öztürk and N. Akdoǵan, Journal of Magnetism and Magnetic Materials **330** (2013) 159-162.

6. Tin, Manganese Doped Chromium Iron Oxides of Composition α-$Sn_{0.2}Cr_{1.8-x}Fe_xO_3$, K. Mbela, T. Moyo, J. Z. Msomi, Journal of Superconductivity and Novel Magnetism **25** (2012) 2637-2641.

Dedication

Now unto him that is able to do exceedingly abundantly

above all that we ask or think,

According to the power that worketh in us,

For in him we live, and move, and have our being; ...

Unto him be glory...

By Christ Jesus throughout all ages.

Amen.

Eph 3:20, Act 17:28

Contents

Acknowledgments

The path leading to the realization of this work has left profound marks of loads of support from many namely friends, families, experts and my fellow christians believers. To all of these people I am very grateful and would like to use this occasion to thank them. I particularly thank Dr Thomas Moyo for giving me support, guidance and many opportunities for interaction with experts in this field. I also thank Dr Justice Msomi and Dr Hafiz Abdallah for the fruitful discussions leading to this accomplishment. The members of the Electron Microscope Unit, Westville Campus, University of KwaZulu-Natal and my colleagues in the School of Chemistry and Physics provided me with the appropriate working environment for carrying out my research. This work would not have been possible without the financial support provided by the University of KwaZulu-Natal and the magnetization measurement equipment grants provided by the National Research Foundation (NRF) of South Africa. I am also grateful to Professors N. Akdogàn and M. Öztürk for helping us with low temperature magnetization measurements at the Gebze Institute of Technology in Turkey. Finally, I would like to thank my parents and my family for their patience and understanding for the entire study period. May God bless you all.

List of Figures

List of Tables

Chapter 1

Introduction

1.1 Defining the nanoscale

Nanoscale materials are defined as substances in which at least one dimension is less than approximately 100 nm. A nanometer is one millionth of a millimeter and that is approximately 10^5 times smaller than the diameter of a human hair [1]. Nanomaterials are interesting because at this scale unique optical, magnetic, electrical and other properties emerge. These novel properties often originate from the high surface area to volume ratio in structures of this size. Surface effects, which are often negligible when studying bulk materials become significant. These emergent properties that are different for materials of the same chemical composition in their nano and bulk forms have the potential for significant impacts in several fields such as electronics, medicine, biotechnology, biomedical, material science, engineering, and environmental areas [2–5]. Nanoparticles have nanoscale dimensions in every direction. A variety of methods are used to prepare nanoparticles which include chemical vapor deposition [6], sputtering [7], microemulsion polymerization [8], mechanical milling [9, 10] and wet chemistry methods [11]. For size-dependent physical properties, highly monodispersed samples are desirable [12]. Several different classes of nanoparticles can be produced. Some of the most extensively studied magnetic nanoparticles are metals, nanoparticle of rare earth metals, magnetic alloys, ferrites and magnetic oxides [13, 14]. However

in this work we consider structural and magnetic properties of doped Cr_2O_3 or Fe_2O_3 nanoparticle oxides.

1.2 Brief overview of iron oxides

The term "iron oxide" can also be used as a generic name for iron hydroxides, oxyhydroxides and other related compounds and have been known for millenia [15]. Such minerals were used originally as pigments for paints during the Palaeolithic. Much later, the materials were used in magnetic compasses when they were discovered in China. This was in fact the first application of magnetic iron oxides, also known as *lodestones*, used by early navigators to locate the magnetic North. Iron oxides have received increasing attention due to their extensive applications such as magnetic recording media, catalysts, pigments, gas sensors, optical devices, and electromagnetic devices [16]. The oxides exist in a rich variety of structures (polymorphs) and hydration states. Among several crystalline modifications of anhydrous ferric oxides there are two common magnetic phases, namely, rhombohedral hematite (α-Fe_2O_3) and cubic maghemite (γ-Fe_2O_3). In the α-phase, all Fe^{3+} ions have an octahedral coordination, whereas in γ-phase having the structure of a cation-deficient AB_2O_4 spinel, the metal atoms A and B occur in tetrahedral and octahedral environments, respectively. The oxide α-Fe_2O_3 is antiferromagnetic at temperatures below 950 K [17], while above the Morin point (260 K) [18] it exhibits weak ferromagnetism. Hematite, the thermodynamically stable crystallographic phase of iron oxide with a band gap of 2.2 eV is a very attractive material because of its wide applications especially in catalysis, gas sensors, pigments, and paints [19]. Its nontoxicity is an attractive feature in these applications. In the present work, the study of mixed metal oxides has been undertaken in order to investigate the evolution of properties as a function of synthesis method, composition and temperature of the samples [16]. (Sn, Mn, Mg)$_{0.2}$Fe$_x$Cr$_{1.8-x}$O$_3$ are examples of

mixed oxides which we have produced and studied [20, 21]. These oxides have been produced by low temperature synthesis using a reflux method and a stirred pressure reactor. High-energy ball milling has been used to reduce the particle sizes. The nano oxides produced reveal interesting properties which are the subject of this thesis.

1.3 Crystal structure

Several iron oxides share the same crystal structure with other minerals. For instance, goethite is isostructural with diaspore (α-AlOOH), magnetite with spinel ($MgAl_2O_4$) and hematite with corundum (Al_2O_3) [22]. Thus, the denomination corundum oxides for the later case. The structure of pure corundum consists of octahedral sites within a trigonal crystal system in which metal cations fill two thirds of the octahedral sites and oxygen anions are present in one third of the octahedral sites. Each oxygen is shared between 4 octahedra. The unit cell parameters are as follows; $a = b = 4.75$ Å, $c = 12.982$ Å, $\alpha = \beta = 90°$, $\gamma = 120°$. Figure 1.1 shows a sketch of a corundum structure [23].

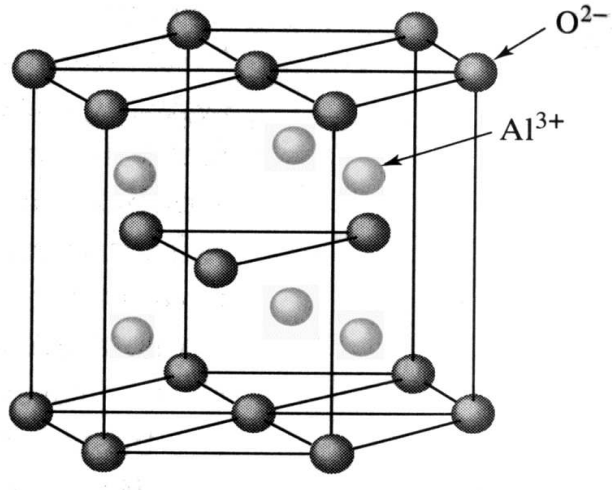

Figure 1.1: Crystal structure of corundum (metal gray, Oxygen black).

1.3.1 The octahedral site

In pure corundum structure six oxygen atoms surround each aluminium atom in the form of a slightly irregular octahedron due to the non-existent centre of symmetry. The three oxygen atoms above the metal atom are closer to each other than the three oxygen atoms below. Due to the large ratio of the radius of the oxygen (1.40 Å) anion to the radius (0.57 Å) of the metal cation, the metal cations are located between the closely packed oxygen anions as shown in Figure 1.2 [23].

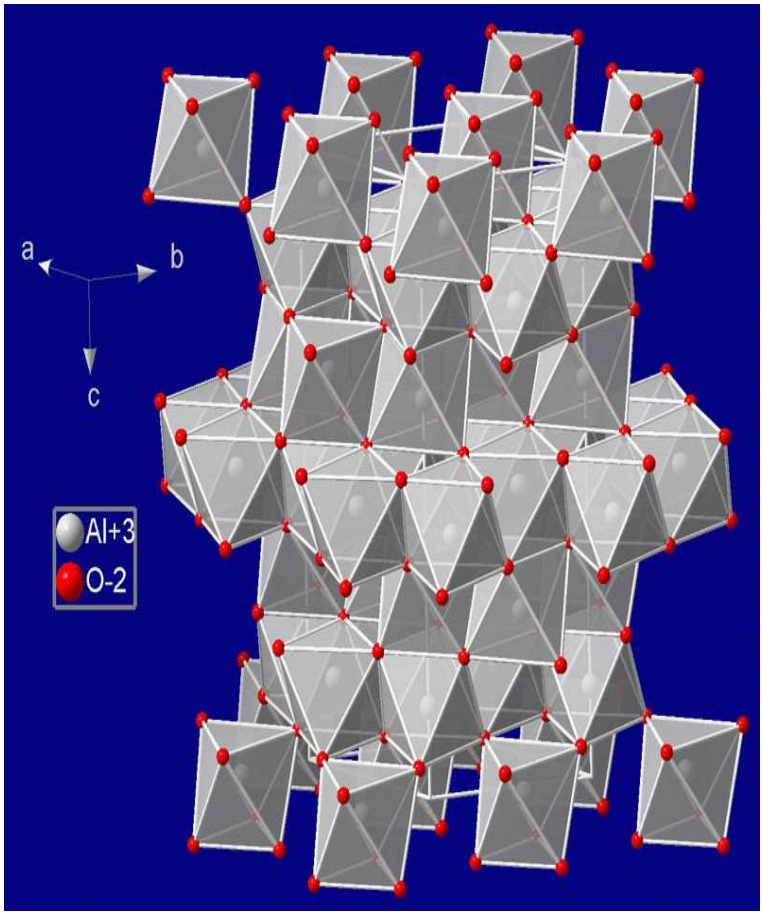

Figure 1.2: Crystal structure of Alumina (corundum). The octahedral sites are visible.

1.3.2 Cations distribution

Figure 1.3 shows the distribution of cations in the crystal structure of alumina (corundum). In terms of the ionic bonding, the positively charged metal ion is surrounded by six negatively charged oxygen ions. Each metal atom gives up three electrons to become a metal ion of valency 3^+ and does not have any unoccupied energy levels. Similarly, the oxygen atom receives two electrons to become an oxygen ion of valency 2^- and does not have any unoccupied energy levels [24]. This produces an electrostatic field around the metal cations, also known as a crystal field. The crystal fields within the corundum allow metal impurities to bind to the crystal because the chemical bonding between the corundum and the guest impurity will always involve the donation of electrons from the corundum to the metal impurity. For example, impurities such as titanium and iron will change the form of the corundum to a colored sapphire. A chromium impurity will transform the colorless corundum crystal into a red ruby. In pure corundum all the electrons in the crystal are paired. This disables the ability of the crystal to absorb any light and hence the absence of colour in pure corundum results [24].

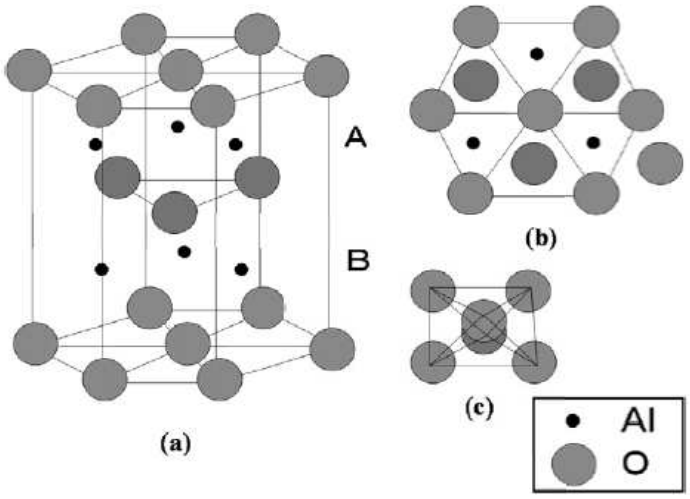

Figure 1.3: (a) Corundum structure in α-Al_2O_3, (b) top view of the corundum structure, and (c) octahedral structure of α-Al_2O_3.

1.4 Synthesis of metal oxides

The synthesis of single and mixed metal oxides by simple low cost methods and in high yield has been a challenge since the early development of Nanoscience. Various approaches have been developed so far for the commercial production of metal oxides. The oxides in the bulk and nanosize forms can be produced by solid state reaction and wet chemistry methods [25, 26]. Solid state reaction has been used intensely to produce mixed metal oxides in the bulk form. The starting materials in this technique are usually high purity metal oxides. This method involves prolonged double sintering at high temperatures of at least 1000 °C and as high as 1400 °C. The elevated temperatures might cause some of the constituent materials to evaporate thus unbalancing the stochiometry. Mixed metal oxides materials can also be made by high-energy ball milling where the mechanosynthesis of the nanostructures is promoted by the mechanical activation of the chemical reactions involved in the formation of the oxides. The oxide mixtures are milled for several hours in agate or hardened steel jars with an appropriate number of balls. Good quality samples and the desired phase form if the milling conditions such as grinding ball to sample mass ratio, the rotation speed of the jars and the atmosphere in the jars are well defined. Although nanoparticles can be directly produced by this method, as is the case for grinding in the conventional ceramic method, some sample is lost by sticking to the hardened steel jars and balls which may affect the stochiometric composition. During the grinding process undesired impurities from the grinding surface may also contaminate the sample. When milling in oxygen atmosphere, possible changes in stoichiometry of the sample can also occur due to the formation of metal oxides. Mixed metal oxides can also be synthesized by the combustion process where metal nitrates are mixed with a fuel such as urea and then heated up to generate an exothermic reaction after self-ignition of the mixture [9]. Co-precipitation methods are simple methods of synthesizing nanoparticles from

salts such as nitrates, chlorides, sulfates and perchlorates. With the appropriate ratios of the precursor salts, it is possible to obtain a narrow size distribution of spherical nanoparticles [25, 27, 28]. As an alternative method, the polyol process, uses polyols such as ethylene glycol. Polyols are boiling solvents, reducing agents and stabilizers that control the growth and prevent the aggregation of nanoparticles. This method is useful for the preparation of dispersed nanoparticles with tailored sizes and tuneable properties [28]. Thermal decomposition at appropriate conditions will yield monodispersed nanocrystals in one reaction without a further size-selection process. Large scale amounts of material can be produced because inexpensive reagents can be used [26]. The samples studied here were produced by hydrothermal method which involves aqueous solutions at atmospheric or higher vapor pressures. This technique is very effective in controlling the size and shape of nanocrystals. The starting materials are high-purity metal chlorides or nitrates mixed with a precipitating reagent such as NH_3, NaOH or KOH. The technique has the advantage of eliminating impurities compared to the synthesis by solid state reaction. A detailed discussion of the technique and equipment used is given in chapter 4.

1.5 Magnetic properties

There are various forms of magnetism that arise in solids depending on how the constituent magnetic moments interact with each other. The magnetic properties are determined by the magnetic interactions between magnetic moments which depend on the location of metal cations in the crystal structure [29]. Bulk antiferromagnets are magnetically inactive materials due to the antiparallel arrangement of spins. Antiferromagnetic (AF) order in metal oxides, such as hematite (α-Fe_2O_3, results from the superexchange interaction between the Fe^{3+} spins mediated by neighboring oxygen ions. A considerable fraction of the spins on the surface are uncompensated. However,

their contribution is insignificant in bulk materials. Bulk hematite present the Morin transition (T_M 260 K), which is the magnetic change from a high-temperature weakly ferromagnetic phase to a low-temperature antiferromagnetic phase caused by spin canting. The crystal structure of hematite is similar to that of corundum (Al_2O_3) and it can be described as a rhombohedral structure with R-3c space group. Moreover, it has been reported that the Morin transition depends on crystallite size, impurities, strain and defects [30–32]. In Figure 1.4 we show the Mössbauer spectrum of a bulk iron (III) oxide powder with particle size < 5 μm and purity ≥ 99 % (SIGMA-ALDRICH) (measured at room temperature in the Condensed Physics Laboratory (UKZN). In nanostructured

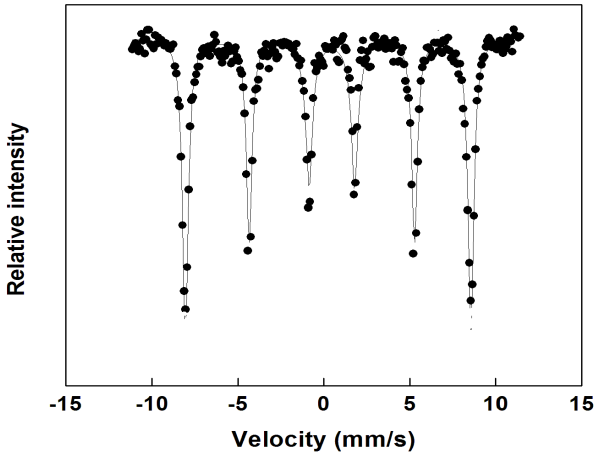

Figure 1.4: Room temperature Mössbauer spectrum of the bulk hematite (α-Fe_2O_3 powder.

magnetic materials, mixed metal interactions between nanoparticles play an important role. Long-range magnetic interactions can have a strong influence on the magnetic dynamics in a sample containing ferromagnetic or ferrimagnetic nanoparticles [33]. If nanoparticles are in close proximity, exchange interactions between surface atoms can be significant. An important example of magnetic proximity effects is exchange bias, which manifests itself as a shift in the hysteresis loop below the Curie temperature [34]. The magnetic properties of weakly interacting magnetic nanoparticles are strongly in-

fluenced by superparamagnetic relaxation at finite temperatures. Mössbauer studies of hematite (α-Fe_2O_3) [30–32] nanoparticles have shown that the superparamagnetic relaxation of antiferromagnetic nanoparticles can be significantly suppressed if the particles are in close proximity. This has been explained by exchange interaction between surface atoms of neighboring particles [30, 35]. André-Filho *et al.* [36] have studied the size dependence of the magnetic and hyperfine properties of nanostructured hematite (α-Fe_2O_3) powders prepared by the ball milling technique. They obtained well-resolved magnetic sextets at room temperature as shown in Figure 1.5. This implies that the thermal relaxation effects associated with the nanostructured samples are not present. Due to the assymmetric shape and the peaks broadening with the milling time, the fits of the spectra were carried out using a histrogram distribution of sextets for the milled samples. In Table 1 are listed the hyperfine parameters, the distribution width and spectral areas determined from the fits. In all samples, the inclusion of a sextet consistent with the presence of α-Fe is in agreement with the structural analysis [36].

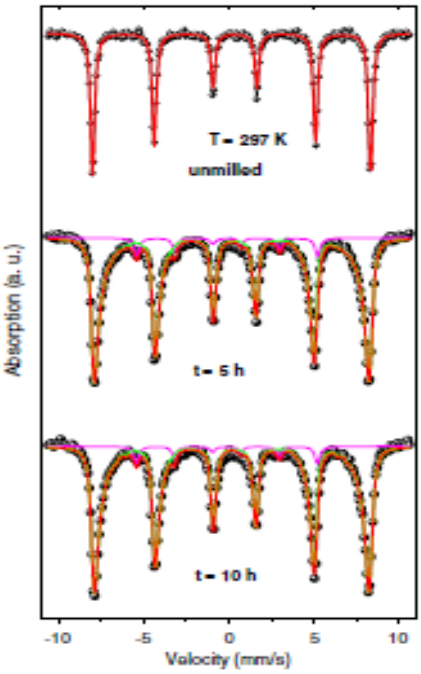

Figure 1.5: Room temperature Mössbauer spectra of the milled hematite powders.

Table 1.1: Hyperfine parameters from Mössbauer spectra recorded at room temperature for the Bulk hematite and milled powders.

$T = 300$ K	Hematite					α-Fe	Source
	δ mm/s ± 0.01	Δ mm/s ± 0.01	B_{hf} kOe ± 0.1	W (T)	f %	f %	
Bulk	0.36	-0.12	515.6		100		[Figure 1.4]
Milled (1 h)	0.36	-0.18	493.2	2.5	96	4	[34]
Milled (5 h)	0.35	-0.18	485.3	2.8	93	7	[34]
Milled (10 h)	0.36	-0.16	486.4	2.9	93	7	[34]

1.6 Some applications of iron based oxides

Iron based oxides nanoparticles show a wide variety of anomalous magnetic properties compared to their respective bulk materials. The magnetic properties of small particles are strongly influenced by finite-size effects [37]. The relevance of these effects increases with decreasing particle size. Finite size effects result from the quantum confinement of the electrons, whereas typical surface effects are related to the symmetry breaking of the crystal structure at the boundary of each particle [38]. Small magnetic particles exhibit unique phenomena such as superparamagnetism, quantum tunnelling and unusually large coercivities. Iron oxides can also be used as colouring and coating materials. The use of hematite and other iron oxides as natural red ceramic pigments has been practiced since prehistoric times. Iron oxides such as magnetite, hematite, maghemite and goethite are commonly used as pigments for black, red, brown and yellow colours respectively. Predominantly natural red iron oxides are used in primers for steel construction and reduction of corrosion problems in cars [39]. Iron oxide-based materials have been found to be good candidates for cheap and efficient

catalysts. Magnetite and hematite are widely used to enhance oxidation/reduction and acid/base reactions. The catalytic activities of Fe_2O_3 has been reported by Sohn and Jim [40]. Multi-walled carbon nanotubes have been synthesized using $Cr_{2-x}Fe_xO_3$ solid solutions as catalysts [41]. Iron and titanium mixed oxides have been found to be catalytically active for the reactions of cyclohexane oxidation [42], $\alpha-$pinene oxide isomerization, O-Cresol photo-degradation [15] and formation of dimethyl ether from methanol. Fe_2O_3 based nanomaterials have also been developed for selective catalytic reduction (SCR) of NO_x by NH_3 in diesel exhausts [43]. A number of studies have also focused on iron oxide Fe_2O_3 which in the gamma and cubic phases exhibits good sensing characteristics towards hydrocarbon gases, carbon monoxide and alcohols [38], [39, 44, 45]. The sensitivity of iron oxide-based sensors can be enhanced further by various doping schemes. A number of different dopants such as Pd, Sn, Ti and Zn have been used [46–48]. While doping is an important factor for controlling the sensing characteristics, the sensor structure and the thickness of its active layer play a significant role on its sensitivity. Iron oxide nanoparticles are also interesting due to their wide range of applications in fields such as magnetic storage, medicine, chemical industries and water purification.

1.7 Motivation for current work

Ferric oxide (α-Fe_2O_3), chromic oxide (α-Cr_2O_3) and their mixed compounds have application in many fields. They can be used as catalysts for high temperature water-gas shift reaction [49] and reduction of NO_x by NH_3 [50], as refractory materials [51] and sensing materials [52]. Their crystal structure is the same as that of corundum (Al_2O_3). α-Fe_2O_3 and α-Cr_2O_3 have different semiconducting and sensing properties. Their magnetic and structural properties are influenced by particle sizes [16, 19], degree of crystallinity [53], pressure [54] and doping [48, 55]. The effect of metal doping by tita-

nium [56, 57], tin [58, 59], manganese [60], aluminium [61], [62], gallium [63] and indium [64] on the electrical, magnetic and other physical properties of α-Fe_2O_3 (hematite) has been investigated for some time. It is generally proposed that the dopant metal ions substitute for Fe^{3+} in the corundum-related structure of α-Fe_2O_3 with the consequent formation of cationic and anionic vacancies. The difference in ionic radius between the dopant metal ion and that for Fe^{3+} will influence the structural characteristics and phase behavior of the doped system. The tin-doped α-Fe_2O_3 system has attracted interest because of its sensing properties for gases such as methane and carbon monoxide [46, 65, 66]. The microstructure of tin-doped α-Fe_2O_3, prepared by mechanical milling was examined by Jiang *et al.* [67] using Rietveld structure refinement of X-ray powder diffraction data and the results were interpreted in terms of the Sn^{4+} ions occupying interstitial octahedral sites in the α-Fe_2O_3 lattice. The properties of α-Cr_2O_3 can also be drastically changed by varying their size and introducing dopants [68–70]. Literature suggests that introducing dopants into the sensor material is an effective way to improve sensitivity and selectivity [71]. Formation of mixed oxides leads to the modification of the electronic structure of the system. Surface properties are expected to be influenced by new boundaries between grains of different chemical composition. It is anticipated that all these phenomena will contribute advantageously to the gas sensing mechanism [71]. Undoped and doped α-Cr_2O_3 gas sensors have been investigated for detection of toxic and combustible organic vapour. Ammonia sensing properties of Ti^{4+} doped α-Cr_2O_3 were first reported by Moseley and Williams [72]. Pokhrel *et al.* [73] prepared fine powders of $Cr_{2-x}Ti_xO_3$ and observed that these materials are excellent candidates for acetone monitoring. However, literature on gas sensors based on tin-chromium mixed oxides is rarely available [73], [74]. The substitution of Cr^{3+} by Fe^{3+} to form solid solutions of the type α-$Fe_{2-x}Cr_xO_3$ has been known for some time [39]. Although there have been several studies of the α-$Fe_{2-x}Cr_xO_3$ [39, 75, 76] system, there appears to have been little activity in the doping of these materials by tin. Berry

et al. [77] initiated a study of tin-doped oxides of the type α-Cr_2O_3 and α-$(FeCr)_2O_3$ and reported on their structural properties. Any systematic study of these compounds would be important. We have therefore initiated a study of these compounds to investigate how single phase formation is influenced by various factors such as the synthesis method, conditions and route. We aim to find the best substitutions to improve the properties of the iron oxides. The characteristics of the dopants are presented in Table 1.2 [78]. Therefore, we have extended our studies to include substitutions by Sn, Mg

Table 1.2: Characteristics of the dopants.

Dopant	Electronic configuration	Atomic radius (pm)	Valence	Possible ions
Mg	$[Ne]3s^2$	145	2	Mg^{2+}
Mn	$[Ar]\ 4s^2 3d^5$	161	7	Mn^{2+}, Mn^{4+}, Mn^{7+}
Sn	$[Kr]5s^2 4d^{10} 5p^2$	145	4	Sn^{2+}, Sn^{4+}

and Mn. In this respect, $Sn_{0.2}Fe_xCr_{1.8-x}O_3$, $Mg_{0.2}Fe_xCr_{1.8-x}O_3$ and $Mn_{0.2}Fe_xCr_{1.8-x}O_3$ have been synthesized by hydrothermal reaction in a reflux system and a pressure reactor from pure metal chlorides at about 100 °C. We are also interested in the study of the onset of single domain structure as a function of particle size and how it relates to the observed properties such as coercive fields, magnetization and exchange bias effects. The particle sizes can be modified by milling and by thermal annealing of the as-prepared samples [6, 79]. Reliable values of the particle sizes are therefore necessary. We have obtained these from the measurements of X-ray diffraction (XRD), transmission electron microscopy (TEM).

In the next chapter we explore some details of the origin and different varieties of

magnetic order in solids. The basic principles of Mössbauer spectroscopy technique are reviewed in chapter 3. The experimental details are presented in chapter 4. In chapters 5, 6, 7 and 8 we present the results and discussions and finally the general conclusions are provided in chapter 9.

Chapter 2

Magnetism and magnetic order in solids

2.1 Introduction

There are various forms of magnetism that arise depending on how the magnetic dipoles interact with each other. In this chapter we discuss the different types of magnetic order in solids and review the most important concepts. These concepts are helpful in understanding and interpreting the experimental data of the materials under investigation in chapters 5 to 8. For detailed discussions of the varieties of Magnetic order in Solids, the reader is referred to a classical review by Hurd [29] and more recent books [80, 81]

2.2 Origin of magnetic moments

It is well known that moving electrical charges produce magnetic fields. This is a universal phenomenon that occurs for charges moving in a wire or for electrons orbiting a nucleus. To understand the existence of magnetic moments in solids, an analysis of the atomic structure is needed. Each electron in an atom has associated magnetic moments that originate from two sources. One is related to orbital motion around the nucleus and the other is its intrinsic spin. Being a moving charge, an electron may be

considered to be a small current loop which gives rise to orbital magnetic moments. The other magnetic moment originates from the intrinsic spin which can be spin up or down with respect to the direction of motion [82]. Both situations are illustrated in Figure 2.1. It is easy to show the link between magnetic moment and angular

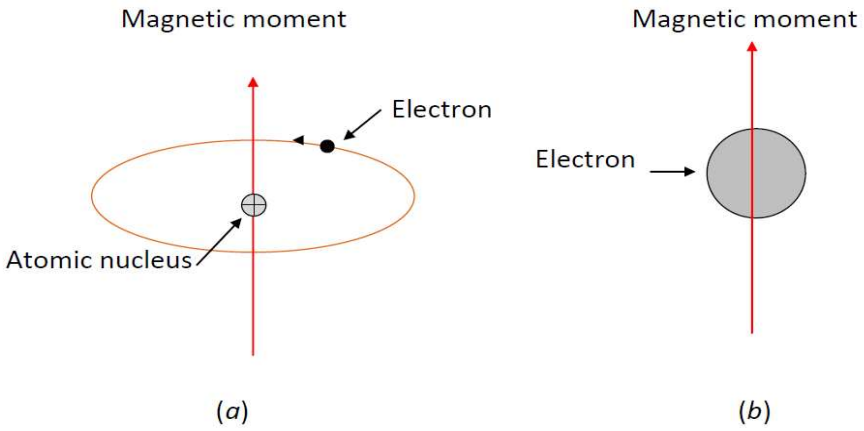

Figure 2.1: The magnetic moment associated with (a) an orbiting electron and (b) a spinning electron.

momenta of the electrons. Spin angular momentum usually dominates orbital angular momentum in determining the magnetic properties of a material [82]. In the following lines we are going to illustrate the existence of a magnetic moment due to an electron orbiting around the nucleus. An electron of mass m_e moving in a closed orbit of radius r would generate a current I associated with a magnetic moment defined as

$$\mu = IA \tag{2.2.1}$$

where A is the area of the closed loop with a magnitude of π r^2. If the electron with charge $(-e)$ moves at a frequency f (with an angular speed ω =2πf) then

$$I = -ef = -\frac{e\omega}{2\pi}. \tag{2.2.2}$$

The orbital magnetic moment can be written as

$$\mu = -\frac{er^2}{2}\omega = -\frac{em_e r^2}{2m_e}\omega = -\frac{e}{2m_e}l_z \tag{2.2.3}$$

where l_z is the orbital angular momentum given by $m_e r^2\omega$. In Quantum Mechanics, l_z is quantized in terms of the Planck's constant $\hbar = \frac{h}{2\pi}$ ($l_z = m_l\hbar$ where m_l = 0, 1, 2, 3 ...). The z-component of the orbital moment can be expressed as

$$\mu_z = -\left(\frac{e\hbar}{2m_e}\right) m_l = \mu_B m_l. \tag{2.2.4}$$

The most fundamental unit for magnetic moments is known as the Bohr magneton μ_B, which is defined as $\mu_B = \frac{e\hbar}{2m_e} = 9.274 \times 10^{-24}$ J/T. Similarly, the resultant spin momentum is given by $\mu_S = -g_S\mu_B m_s$, where g_S=2.0023. Spin magnetic moments may only be in up or in down directions with spin quantum numbers $m_s = \pm\frac{1}{2}$. The net magnetic moment for an atom is just the sum of the magnetic moments of each of the constituent electrons, including both orbital and spin contributions and taking into account moment cancellations. For light elements, like 3d-metals, according to the Hund's rules and Russel-Saunders coupling [82], first the orbiting electrons produce a resultant angular momentum

$$\overrightarrow{L} = \sum_{i=1}^{n} \overrightarrow{l_i}. \tag{2.2.5}$$

Similarly the spin angular momentum of the electrons of a light atom couple to give a resultant spin momentum

$$\overrightarrow{S} = \sum_{i=1}^{n} \overrightarrow{s_i}. \tag{2.2.6}$$

Both quantities $\overrightarrow{L}$ and $\overrightarrow{S}$ are required to minimize the atomic energy. The total angular momentum $\overrightarrow{J}$ of an atom is taken as the coupling of $\overrightarrow{L}$ and $\overrightarrow{S}$ through spin-orbit interaction [82, 83]. Using Hund's rules, the magnitude of the magnetic moment of an atom can be shown to be

$$\mu_J = \mu_B g\sqrt{J\,(J+1)}, \tag{2.2.7}$$

where the g factor is defined by

$$g = 1 + \frac{J(J+1) + S(S+1) - L(L+1)}{2J(J+1)}, \tag{2.2.8}$$

for a free atom [82, 83]. For an atom having completely filled electron shells or subshells, when all electrons are considered, there is total cancellation of both orbital and spin moments. Thus, materials composed of atoms having completely filled electron shells will not have permanent magnetic moments.

2.3 Magnetization and susceptibility

The magnetization $\overrightarrow{M}$ of a material is defined as the total magnetic moment per unit volume of a sample and can be expressed as

$$\overrightarrow{M} = \frac{1}{V} \sum_{i=1}^{N} \overrightarrow{\mu_i}. \tag{2.3.1}$$

This is a magnetic field dependant quantity which is sensitive to the temperature and the coupling between the magnetic moments. It is usually more convenient to express this physical quantity in terms of the mass of the sample because during measurements the volume of a sample may change due to thermal expansion and magnetostriction effects [83]. We can therefore write the magnetization per unit mass as

$$\overrightarrow{\sigma} = \frac{1}{m} \sum_{i=1}^{N} \overrightarrow{\mu_i}. \tag{2.3.2}$$

In the presence of an external applied magnetic field H, the magnetic moments within a material will tend to become aligned with the field and to reinforce it. We can then determine the magnetization experimentally. The magnetic flux strength and the flux density are related according to the equation

$$\overrightarrow{B} = \mu \overrightarrow{H} \tag{2.3.3}$$

where μ is the permeability of free space and $\overrightarrow{B}$ is the magnetic induction or magnetic flux density. The magnitude of $\overrightarrow{M}$ is proportional to the applied field as follows

$$\overrightarrow{M} = \chi \overrightarrow{H} \tag{2.3.4}$$

and χ is called the magnetic susceptibility. The susceptibility of a material represents the degree to which a material responds to an external applied magnetic field. It helps to classify materials of various types in broad groups. Materials with a negative susceptibility are called diamagnetic as shown in Figure 2.2 [83]. Other types of magnetic order exist which have a wide range of suceptibilities and are illustrated in Figure 2.3 [83].

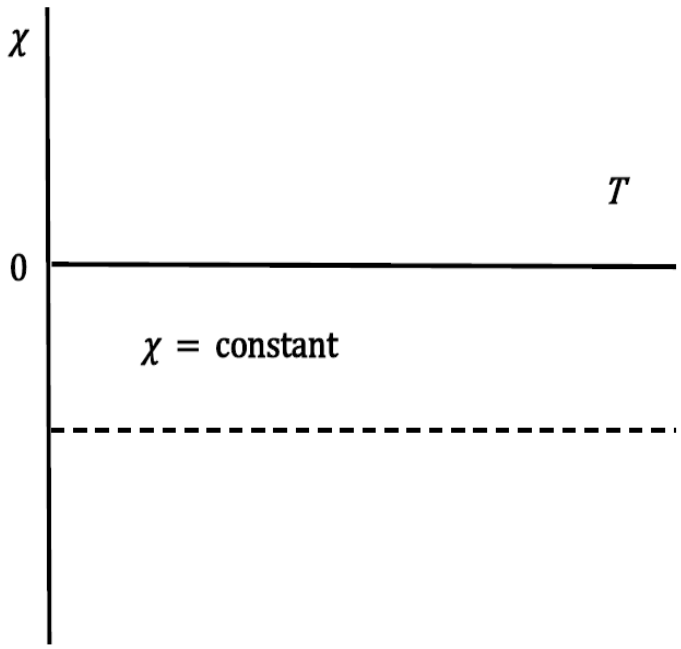

Figure 2.2: Graph of magnetic susceptibility versus temperature for a diamagnetic material.

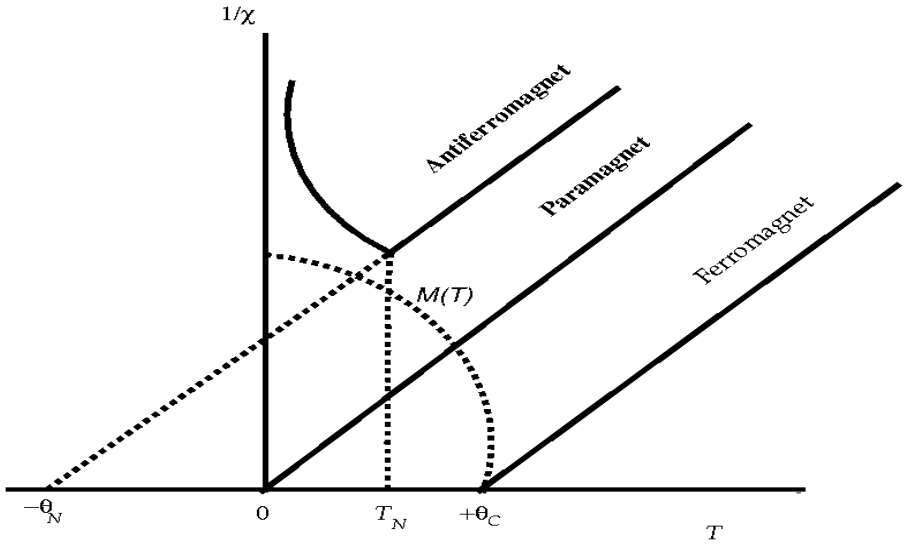

Figure 2.3: Variation of inverse magnetic susceptibilities with temperature for paramagnetic, ferromagnetic and antiferromagnetic materials.

2.4 Magnetic order

As we have stated previously, the magnetic susceptibility, χ is a useful property for characterising magnetic materials. Its temperature dependence (usually the inverse of the susceptibility) is a good characterization parameter. In the next sections, we discuss the different types of magnetic order that occur in solids in more detail.

2.4.1 Diamagnetism

Diamagnetism is a very weak form of magnetism that is non-permanent and persists only while an external field is being applied on a sample. It is induced by a change in the orbital motion of all electrons due to applied magnetic fields. The magnitude of the induced magnetic moment is extremely small and is in a direction opposite to that of the applied field. Figure 2.4 illustrates schematically the atomic magnetic dipole configurations for a diamagnetic material with and without an external field [84]. Here,

the arrows represent induced atomic dipole moments. Diamagnetism is found in all materials. But because it is so weak, it can be observed only when other types of magnetism are not so large. Typical values of the diamagnetic of susceptibilities are of the order -10^{-6} to -10^{-5} [83].

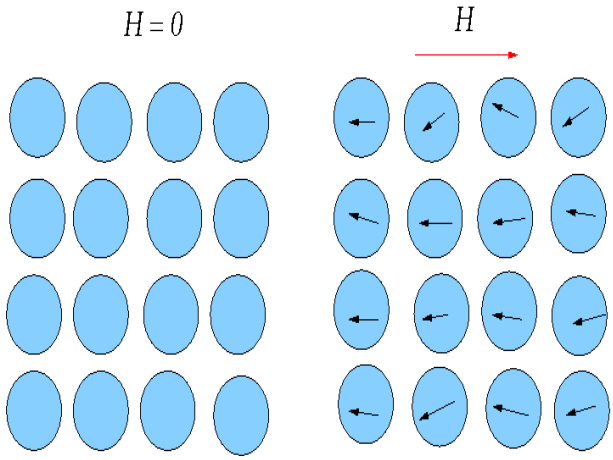

Figure 2.4: The atomic dipole configuration for a diamagnetic material with and without a magnetic field.

2.4.2 Paramagnetism

For some solid materials, each atom possesses a permanent magnetic moment by virtue of incomplete cancellation of electron spin and orbital magnetic moments. In the absence of an external magnetic field, the orientations of these atomic magnetic moments are random, such that the material possesses no net macroscopic magnetization. These atomic moments are free to rotate. Paramagnetism results when the moments preferentially align by rotation with an external field as shown in Figure 2.5. In the presence of a magnetic field B_0, magnetic moments will orient themselves in particular directions with possible energies

$$E_J = -\vec{\mu}_J.\vec{B}_0 = -gm_J\mu_B B_0, \tag{2.4.1}$$

where m_J is the magnetic quantum number with values in range -J<m_J<J.

In equilibrium, the probability for the occupation of each energy level E_{m_J} is given by

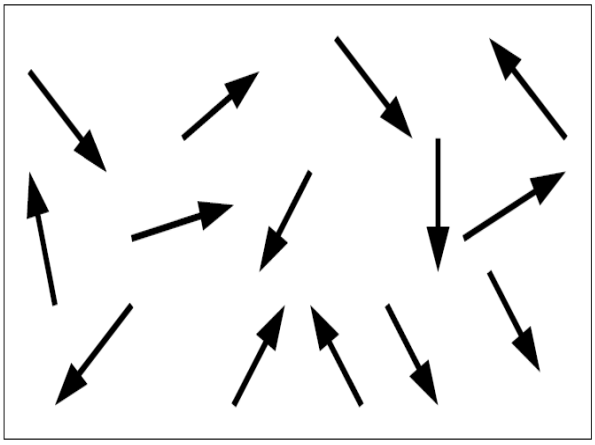

Figure 2.5: Magnetic structure in a paramagnet.

the Maxwell-Boltzmann distribution [84]

$$P(E_J) = \frac{e^{-g\mu_B m_J B_0/k_B T}}{\sum e^{-g\mu_B m_J B_0/k_B T}}, \tag{2.4.2}$$

where k_B is the Boltzman constant. We can show that the average magnetic moment is given by

$$< \mu_B >= g\mu_B J F(J,x), \tag{2.4.3}$$

where $F(J,x)$ is the Brillouin function defined as

$$F(J,x) = \left(1+\frac{1}{2J}\right)\coth\left[\left(1+\frac{1}{2J}\right)x\right] - \frac{1}{2J}\coth\left(\frac{x}{2J}\right). \tag{2.4.4}$$

For n non-interacting magnetic moments per unit volume, the magnetization becomes

$$M = n\langle\mu_B\rangle = ng\mu_B J F(J,x). \tag{2.4.5}$$

The parameter x is a dimensionless ratio of the Zeeman energy to the thermal energy given by

$$x = \frac{g\mu_B J B_0}{k_B T}. \tag{2.4.6}$$

For high temperature ($T \sim 300$ K) and low field ($B_0 \sim 1$ T), x becomes very small ($x \ll 1$) such that the Brillouin function is approximated by

$$F(J,x) \simeq \frac{x(J+1)}{3J}. \tag{2.4.7}$$

This gives

$$M = \frac{ng^2\mu_B^2 J(J+1)B_0}{3k_B T}. \tag{2.4.8}$$

Since the susceptibility is given by

$$\chi = \frac{\mu_0 M}{B_0} \tag{2.4.9}$$

and when substituting for M we get

$$\chi = \frac{n\mu_0 g^2\mu_B^2 J(J+1)}{3k_B T} = \frac{C}{T}. \tag{2.4.10}$$

This is known as the Curie law for susceptibility where

$$C = \frac{n\mu_0 g^2\mu_B^2 J(J+1)}{3k_B} \tag{2.4.11}$$

and C is called the Curie constant. However, when interactions between magnetic moments occur the Curie law is modified to the Curie-Weiss law expressed as

$$\chi = \frac{C}{T - \theta_p}. \tag{2.4.12}$$

θ_p is known as the paramagnetic Curie temperature.

2.4.3 Ferromagnetism

Some materials with permanent magnetic moments and strong interaction between them show spontaneous magnetization even in the absence of an applied magnetic field. This occurs in a wide range of materials which include some alloy and pure metals like Fe, Co, Ni and Gd [83–85]. Magnetic susceptibilities are very high for ferromagnetic materials compared to that of paramagnets typically $\chi_{FM} \sim 10^5\ \chi_{para}$ [83]. Permanent magnetic moments in ferromagnetic materials result from atomic magnetic moments of electrons in different orbits of constituent atoms. In ferromagnetic materials, coupling interactions cause the magnetic moments of adjacent atoms to align with

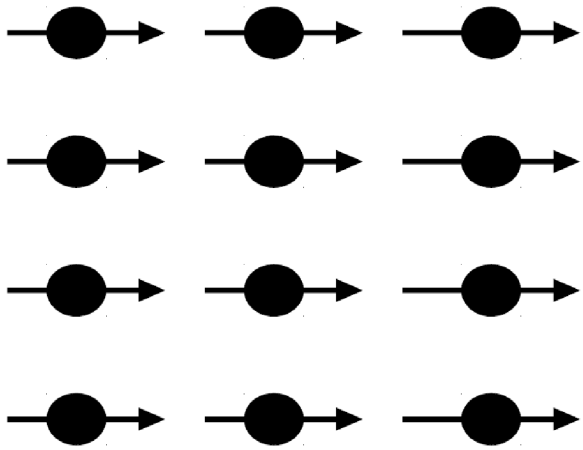

Figure 2.6: Mutual alignment of atomic dipoles for a ferromagnetic material, which will exist even in the absence of an external magnetic field.

one another, even in the absence of an external field. This is schematically illustrated in Figure 2.6. The order is perfect at absolute zero temperature. Increasing the thermal energy of the magnetic moments results in spin disorder due to thermal agitation. At the Curie temperature T_C the disorder of magnetic moments becomes complete. For $T > T_C$, a ferromagnet exhibits properties of a paramagnet with a susceptibility that obeys the Curie-Weiss law. However, the law fails in the vicinity of T_C where critical phenomena apply. The susceptibility near T_C is approximated by $\chi \sim (T - T_C)^{-\gamma}$ when approaching T_C from above and $\chi \sim (T_C - T)^{\beta}$ when approaching T_C from below. The parameters γ and β are called critical exponents and are calculated to be 1 and 0.5 respectively in the so-called mean-field approximation [86]. A strong internal magnetic field B_{in} is assumed to be responsible for aligning up magnetic moments. The spontaneous magnetization that results is taken to be proportional to B_{in} such that

$$B_{in} = \lambda M_s \tag{2.4.13}$$

where λ is referred to as the molecular field coefficient. The positive exchange interactions introduced in Quantum Mechanics are known to be responsible for the existence of B_{in}. The strength of the internal field can be roughly estimated from the magnetic

binding energy $\mu_B B_{in}$ and the thermal energy $k_B T_C$. The magnetic binding energy is responsible for the perfect alignment of moments at $T = 0$ K. At T_C where the magnetic order collapses we expect

$$B_{in} \sim \frac{k_B T_C}{\mu_B}. \tag{2.4.14}$$

B_{in} turns out to be much larger than the field that can be produced due to dipole fields of a permanent magnet. In the presence of external applied magnetic field B_0, the effective magnetic field in a sample is expressed by

$$\overrightarrow{B}_{eff} = \overrightarrow{B}_0 + \overrightarrow{B}_{in} = \overrightarrow{B}_0 + \lambda \overrightarrow{M}_s. \tag{2.4.15}$$

From equation 2.4.5 the magnetization of a ferromagnet in a applied field can be expressed as

$$M_s(B_0, T) = n\ g\ \mu_B\ J\ \ F(J, y) \tag{2.4.16}$$

where the ratio of the Zeeman energy to thermal energy is now defined as

$$y = \frac{g\ \mu_B\ J\ (B_0 + \lambda\ M_s)}{k_B T}. \tag{2.4.17}$$

The magnetization still stays finite even for $B_0 = 0$ since $B_{in} \gg B_0$. At absolute zero temperature ($T = 0$ K), the spontaneous magnetization per unit volume saturates to

$$M_s(0, 0) = n\ g\ \mu_B\ J. \tag{2.4.18}$$

For zero applied field ($B_0 = 0$) and $T > 0$, the reduced spontaneous magnetization of a ferromagnet can be expressed by

$$\frac{M_s(0, T)}{M_s\ (0, 0)} =\ \ F\ (J, y) \tag{2.4.19}$$

From this equation we can also expressed the reduced magnetization as

$$\frac{M_s(0, T)}{M_s(0, 0)} = \left(\frac{k_B\ T}{n\ g^2 \mu_B^2\ \lambda\ J^2} \right) y. \tag{2.4.20}$$

where in this case y is given by

$$y = \frac{g\ \mu_B\ J\ \lambda\ M_s\ (0,T)}{k_B T}. \tag{2.4.21}$$

The ferromagnetic state of a material can therefore be uniquely be described by satisfying two simultaneous equations 2.4.19 and 2.4.20.

2.4.4 Antiferromagnetism

Strong interaction between magnetic moments can give rise to antiparallel adjacent alignments. This is known as antiferromagnetic order. This occurs below the Néel temperature, T_N. Manganese oxide (MnO) is one material that displays this behavior which has ionic character, having both Mn^{2+} and O^{2-} ions. No net magnetic moment is associated with the O^{2-} ions. The Mn^{2+} ions possess a net magnetic moment that is predominantly of spin in origin. These Mn $^{2+}$ ions are arrayed in the crystal structure such that the moments of adjacent ions are antiparallel. This arrangement is represented schematically in Figure 2.7 [86, 87]. The opposing magnetic moments cancel

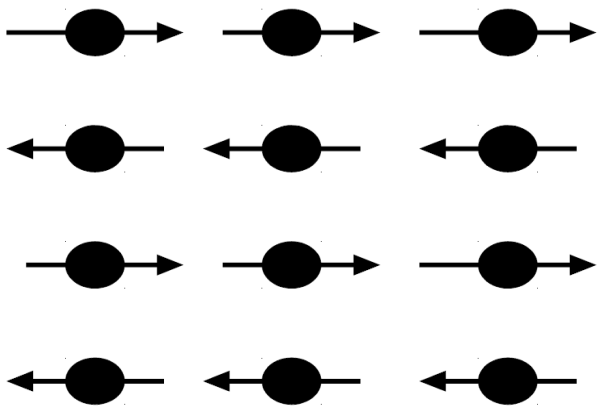

Figure 2.7: Magnetic structure in an antiferromagnet.

one another and as a consequence, the solid as a whole possesses no net magnetization. The antiparallel alignment of moments is due to negative exchange interactions

between moments and is observed only below the critical temperature T_N. The antiferromagnetic crystal can be divided into two atomic sublattices A and B. Below T_N the net saturation magnetization of an antiferromagnet is zero due to the moments that are aligned antiparallel. If the temperature is increased above absolute zero temperature ($T = 0$ K), saturation magnetization in each sublattice decreases with increase in temperature as in a ferromagnet [86]. At T_N, the magnetic moments become randomly oriented and the paramagnetic phase starts. Using the mean-field theory and the assumption that an internal field B_{in} exists as in a ferromagnetic, the internal magnetic fields at the respective sublattices can be written as [85, 86]

$$\overrightarrow{B}_{in}^{A} = \lambda_{AA}\overrightarrow{M}_A + \lambda_{AB}\overrightarrow{M}_B \tag{2.4.22}$$

and

$$\overrightarrow{B}_{in}^{B} = \lambda_{BA}\overrightarrow{M}_A + \lambda_{BB}\overrightarrow{M}_B, \tag{2.4.23}$$

where $\overrightarrow{M}_A$ and $\overrightarrow{M}_B$ are the sublattice magnetizations. The molecular field coefficients λ_{AB} and λ_{BA} correspond to the first nearest neighbors. The second nearest neighbors molecular field coefficient are given by λ_{AA} and λ_{BB} respectively. The internal field assumed to be dominated by interactions between first and second nearest neighbors. We also expect

$$\lambda_{AB} = \lambda_{BA} = -\lambda_1 \tag{2.4.24}$$

and

$$\lambda_{AA} = \lambda_{BB} = \lambda_2 \tag{2.4.25}$$

where λ_1 and λ_2 are both positive constants. Therefore, equations (2.4.22) and (2.4.23) can be rewritten in the form of

$$\overrightarrow{B}_{in}^{A} = \overrightarrow{M}_A\,(\lambda_1 - \lambda_2) \tag{2.4.26}$$

and

$$\overrightarrow{B}_{in}^{B} = \overrightarrow{M}_B\,(\lambda_1 - \lambda_2) \tag{2.4.27}$$

respectively. If we assume that the average magnetizations on A and B sublattices are $M_A = \frac{n}{2} < \mu_A >$ and $M_B = \frac{n}{2} < \mu_B >$, using equation (2.4.3) we can re-write the sublattice magnetizations as

$$M_A = \frac{n}{2}\ J\ g\ \mu_B\ F\ \ (J, y_A) \tag{2.4.28}$$

and

$$M_B = \frac{n}{2}\ J\ g\ \mu_B\ F\ \ (J, y_B) \tag{2.4.29}$$

where

$$y_A = \frac{J\ g\ \mu_B\ B_{in}^A}{k_B T} = \frac{J\ g\ \mu_B M_A\ \ (\lambda_1 - \lambda_2)}{k_B T} \tag{2.4.30}$$

and

$$y_B = \frac{J\ g\ \mu_B\ B_{in}^B}{k_B T} = \frac{J\ g\ \mu_B\ M_B\ \ (\lambda_1 - \lambda_2)}{k_B\ T}. \tag{2.4.31}$$

If the magnetizations on the two sublattices are the same ($M_A = M_B = M$) we get

$$M = \frac{n\ J\ g\ \mu_B F\ (J, y)}{2}. \tag{2.4.32}$$

At $T = T_N$, the magnetization becomes zero at each sublattice as in the case of a ferromagnet at T_C. We can easily show that T_N can be expressed by

$$T_N = \frac{n\ g^2 \mu_0\ \mu_B^2\ J\ (J+1)}{2\ k_B\ \mu_0} = \frac{(\lambda_1 - \lambda_2)C}{2\mu_0}, \tag{2.4.33}$$

where C is the Curie constant as before.

For $T > T_N$, the magnetization on each sublattice also depends on the applied external field B_0 such that the effective field on A and B sublattices is given by

$$\overrightarrow{B}_{eff}^A = \overrightarrow{B}_0 + \overrightarrow{B}_{in}^A = \overrightarrow{B}_0 - \lambda_2 \overrightarrow{M}_A - \lambda_1 \overrightarrow{M}_B \tag{2.4.34}$$

and

$$\overrightarrow{B}_{eff}^B = \overrightarrow{B}_0 + \overrightarrow{B}_{in}^B = \overrightarrow{B}_0 - \lambda_1 \overrightarrow{M}_A - \lambda_2 \overrightarrow{M}_B \tag{2.4.35}$$

respectively. We can also show that the susceptibility above T_N obeys the Curie-Weiss law written as

$$\chi = \frac{C}{T - \theta_p}, \tag{2.4.36}$$

where

$$\theta_p = -\frac{C\ (\lambda_1 + \lambda_2)}{2\mu_0}. \tag{2.4.37}$$

T_N and θ_p are therefore related as follows

$$\theta_p = -\frac{(\lambda_1 + \lambda_2)}{\lambda_1 - \lambda_2} T_N. \tag{2.4.38}$$

In the temperature range below T_N, the magnetic response of an antiferromagnetic material depends on the direction of the applied field B_0. The magnetization depends on whether the field is applied parallel or perpendicular to the alignment of the magnetic moments. This leads to parallel $\chi_\parallel$ and $\chi_\perp$ susceptibilities [86]. In powdered or poly-crystalline samples the average total susceptibility below T_N is given by [86]

$$\chi = \frac{1}{3}\chi_\parallel + \frac{2}{3}\chi_\perp. \tag{2.4.39}$$

2.4.5 Ferrimagnetism

Some ceramics also exhibit a permanent magnetization, termed ferrimagnetism. The macroscopic magnetic characteristics of ferromagnets and ferrimagnets are similar. The distinction lies in the source of the net magnetic moments. The principles of ferrimagnetism are illustrated with the cubic ferrites. Ferrimagnetism is known to be an intermediate magnetic state between ferromagnetism and antiferromagnetism and can be described using the two sublattice theory due to Néel [88]. The net magnetization can be written as

$$M = \lambda M_A - (1 - \lambda)\ M_B, \tag{2.4.40}$$

where $M_A \neq M_B$ as indicated in Figure 2.8. When $M_A = M_B$ we define the ferromag-

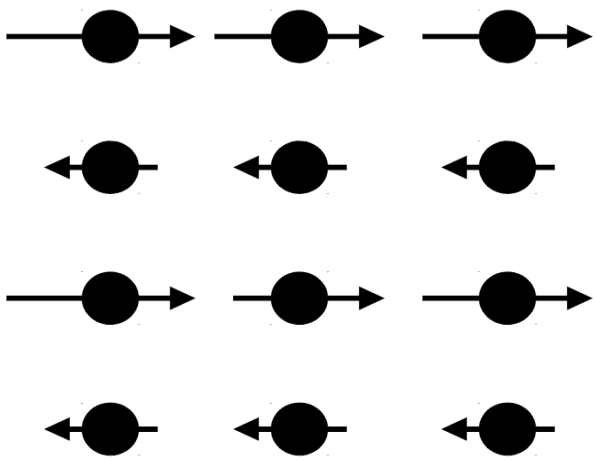

Figure 2.8: Magnetic structure in a ferrimagnet.

netic state corresponding to $\lambda = 0$ or 1 and antiferromagnetic state for $\lambda = \frac{1}{2}$. The ferrimagnetic state occurs when $\lambda \neq 0$, $\frac{1}{2}$ or 1. In ferrimagnets, the net magnetization is always non-zero for $T < T_C$ except in the special case when the magnetizations of the two sublattices may cancel out at a compensation temperature point $T_{comp} < T_C$.

2.4.6 Superparamagnetism

Superparamagnetism is a form of magnetism which appears in small ferromagnetic or ferrimagnetic nanoparticles. The magnetization of each particle can randomly point and flip in directions under the influence of temperature. The average time between flips is called the Néel relaxation time. In the absence of an external magnetic field and when the time used to measure the magnetization of the nanoparticles is much longer than the Néel relaxation time the magnetization of the sample averages to zero. Superparamagnets respond to an external magnetic field in a similar way to a paramagnet but the magnetic susceptibility in this case is much larger [83]. Because of the nanoparticle's magnetic anisotropy, the magnetic moment has usually only two stable orientations which are antiparallel to each other and separated by an energy barrier. The stable orientations define the nanoparticle's so-called "easy axes". At a finite temperature, there is a finite probability for the magnetization to flip and reverse

its direction. For a particle of volume V the Néel relaxation time τ_N is expressed by Néel-Arrhenius equation [88]

$$\tau_N = \tau_0 \exp\left(\frac{KV}{\kappa_B T}\right), \tag{2.4.41}$$

where τ_0 is a length of time that is characteristic of the material called the attempt time or attempt period and κ is the nanoparticle's magnetic anistropy energy density. KV is therefore the energy barrier associated with the magnetization flipping from its initial easy axes direction through a "hard plane", to another easy axes direction. Measurement of the magnetization of a nanoparticle can be made in a finite time τ_m. If $\tau_m \gg \tau_N$, the nanoparticle's magnetization will flip several times during the measurement and the measured magnetization will average to zero. If $\tau_m \ll \tau_N$, the magnetization will not flip during the measurement so the measured magnetization will be what the instantaneous magnetization was at the beginning of the measurement. In the former case, the nanoparticle will appear to be in a superparamagnetic state whereas in the latter case it will appear to be "blocked" in its initial state. The measurement time of the magnetization is therefore critical. The transition between superparamagnetism and blocked state occurs when $\tau_m = \tau_N$ at a temperature called the superparamagnetic blocking temperature T_B^{SP} [34, 89]. Experimentally, superparamagnets do not show hysteresis in the variation of their isothermal magnetization as a function of applied magnetic field [29]. The superparamagnetic state vanishes with the reduction in temperature. The magnetization curve shows a rapid transition with decreasing temperature of the sample. A transition temperature T_B called the blocking temperature can be defined which increases with increasing particle size [90]. In the superparamagnet region $T_B < T_C$, the magnetization response of the particles under the influence of an applied field H is given by [29, 90, 91], [92]

$$\frac{M(T)}{M_S(0)} = \coth\left(\frac{\mu H}{k_B T}\right) - \frac{k_B T}{\mu H} = L\left(\frac{k_B T}{\mu H}\right) \tag{2.4.42}$$

where L is the Langevin's function and μ is the moment of the superparamagnetic particle. Due to the collective excitations, the magnetizations of the nanoparticles can be expressed as [91, 93]

$$M(T) \approx M_S(0)\left(1 - \frac{k_B T}{2KV}\right). \tag{2.4.43}$$

2.5 Magnetic interactions

Magnetic moments in a solid can interact through two mechanisms namely dipole-dipole and exchange interactions. The dipole-dipole interactions can be shown to be too small to account for the origin of spontaneous magnetization. Exchange interactions which have Quantum Mechanical origin are responsible for the observed magnetic order. Magnetic moments that are so close that their wavefunctions overlap interact through direct exchange interaction. This interaction between magnetic moments with spins $\overrightarrow{S}_i$ and $\overrightarrow{S}_j$ can be expressed by the Heinsberg hamiltonian [94]

$$H_e = -J_{ij}\overrightarrow{S}_i.\overrightarrow{S}_j, \tag{2.5.1}$$

where J_{ij} is called the exchange integral which is positive for parallel aligned spins (ferromagnets) and negative for antiparallel aligned spins (antiferromagnets). Indirect exchange occurs through an intermediary when the interacting magnetic moments are far from each other. In metallic systems, the conduction electrons can act as intermediaries. This type of interaction is called the RKKY interaction named after Ruderman, Kittel, Kasuya and Yoshida [94]. In magnetic insulators, distant magnetic moments can interact through non-magnetic ions. This indirect exchange interaction is called superexchange interaction [95].

2.5.1 Magnetic domain structure

Any ferromagnetic or ferrimagnetic material that is at a finite temperature T below T_C is composed of small regions called domains in which there is a mutual alignment of magnetic moments in the same direction as illustrated in Figure 2.9 [88] . Each domain

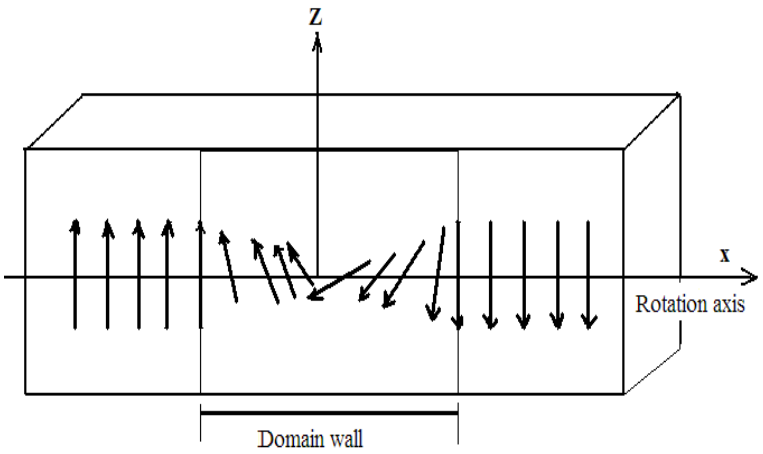

Figure 2.9: Schematic depiction of domains in a ferromagnetic or ferrimagnetic material.

is magnetized to its saturation magnetization. Adjacent domains are separated by domain boundaries or walls across which the direction of the magnetization gradually changes. Domains are usually microscopic in size and for a polycrystalline specimen, each crystalline grain, in general, consists of more than a single domain [95]. Thus in a macroscopic piece of material, there will be a large number of domains and all may have different magnetization orientations giving rise to a zero net magnetization of the sample. When an external field H is applied, the domains change in shape and size by the movement of domain boundaries. Schematic domain structures are represented in the insets (labeled U through to Z) at several points along the B versus H curve in Figure 2.10 [96]. Initially, the moments of the constituent domains are randomly oriented such that there is no net B (or M) field (inset U). The domains that are oriented in directions favorable to the applied field grow at the expense of those that

are unfavorably oriented (insets V through X). This process continues with increasing field strength until the macroscopic specimen becomes a single domain, which is nearly aligned with the field (inset Y). Saturation is achieved when this domain, by means of rotation, becomes oriented with the H field (inset Z).

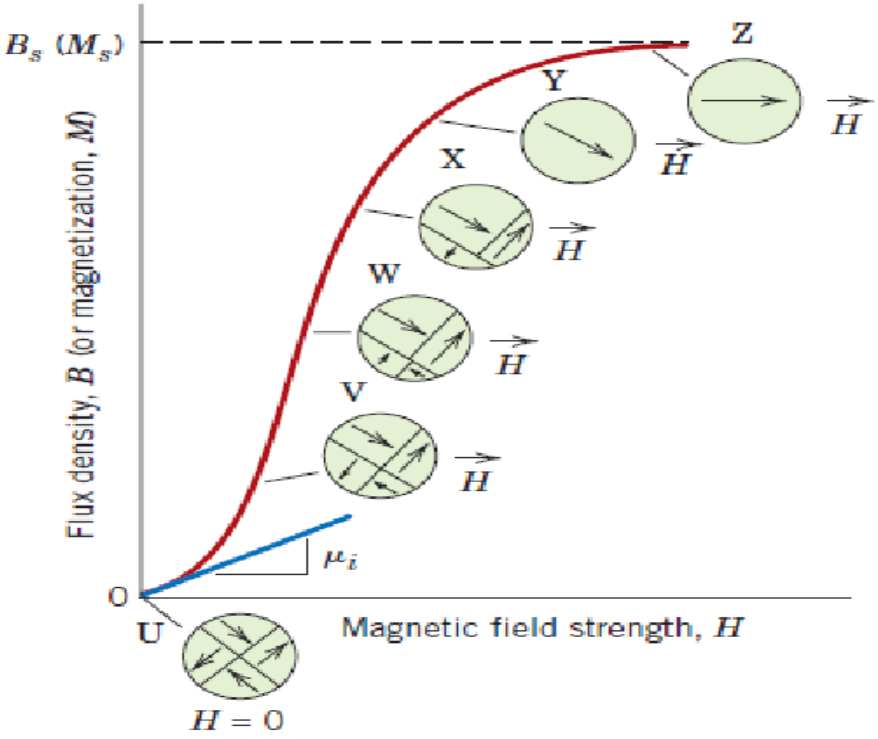

Figure 2.10: The B versus H behavior for a ferromagnetic or ferrimagnetic material that was initially unmagnetized.

2.6 Magnetization process

The magnetization process of a sample is influenced by both external influences and internal microstructure and can be explained by rotation of magnetic moments or by displacement of domain walls. The magnetization characterizes the order of the moments in response to both applied and internal fields. If we assume that a magnetically ordered material consists of domains and domains walls, in the presence of external

fields the magnetization is uniform in the domains and non-uniform in the domain walls. The principal measurements encountered here will involve isothermal measurements of magnetization as a function of applied magnetic field and are presented in the form of a hysteresis loop as shown in Figure 2.11 [96]. From a magnetization point S

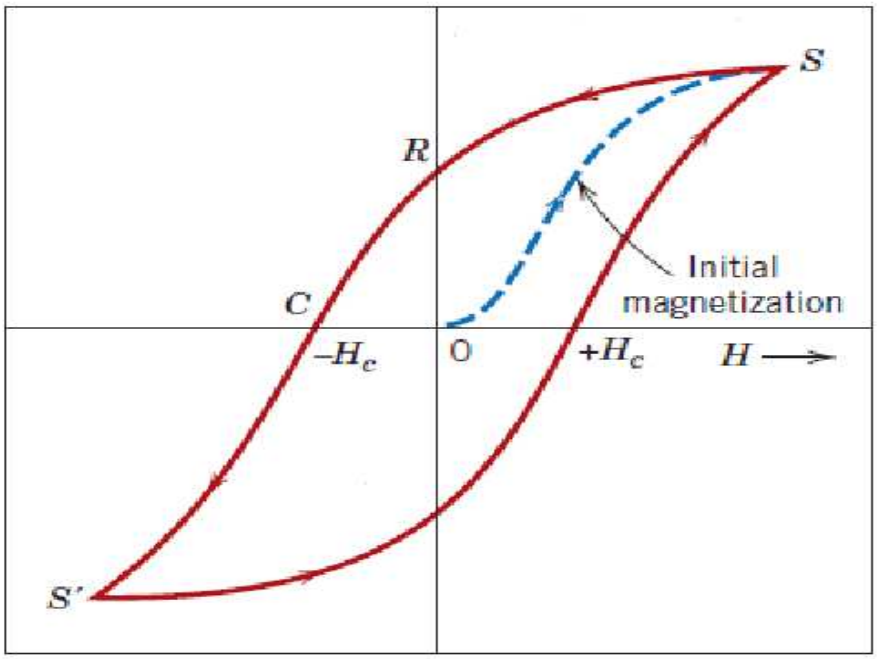

Figure 2.11: Variation of magnetization with applied field in a ferromagnet.

in Figure 2.11, as the field H is reduced, the curve does not retrace its original path. A hysteresis effect is produced in which the magnetization M lags behind the applied field H. At zero field (point R on the curve), there exists a residual field M_r that is called the remanence. Here the material remains magnetized in the absence of an external field. Upon reversal of the field direction from saturation, the process by which the domain structure changes is reversed. First, there is a rotation of the single domain with the reversed field. Next, domains having magnetic moments aligned with the new field will grow at the expense of the former domains [96]. To reduce the magnetization within the specimen to zero, a field of magnitude -H_C must be applied in a direction opposite to that of the original field. H_C is called the coercivity, or simply the coercive

field. Upon continuation of the applied field in this reverse direction, as indicated in the figure, saturation is ultimately achieved in the opposite sense, corresponding to point S'. A second reduction of the field to the point of the initial saturation (point S) completes the symmetrical hysteresis loop and also yields both a negative remanence (-M_r) and a positive coercivity (+H_C). The approach to saturation of the initial magnetization curve can be approximated by an empirical relationship of the form

$$M(H) = M_s(0)\left(1 - \frac{a}{H} - \frac{b}{H^2} - ...\right) + \chi H \tag{2.6.1}$$

where a and b are fit parameters and χ is the high-field susceptibility [96, 97]. The study of the hysteresis loop is important as it provides information about the domain wall movements. The bigger the coercive fields the harder it is to reverse the magnetization. From the hysteresis curve we can be able to distinguish between soft and hard magnets. In this work we will also give particular attention to the evolution of the coercive field with particle size.

2.7 Exchange bias

When a sample contains an interfaces between ferromagnetic, ferrimagnetic and antiferromagnetic phases is subjected to a magnetic field reversal, it may exhibit an additional unidirectional anisotropy due to magnetic coupling at the interface. This effect, called exchange bias (EB), was first discovered nearly 50 years ago in oxidized Cobalt nanoparticles [98]. Exchange bias has also been observed in many other magnetic materials. Although there has been some research in exchange bias in nanoparticles in the last decades, the bulk of exchange bias research has focused mainly on thin film systems [98].

2.7.1 Basic phenomenology of exchange bias

The phenomenolgy of exchange bias has been extensively described in different reviews published on the subject, [98–100]. The main indication of the existence of exchange bias is the shift of the hysteresis loop, H_{EB}, along the field axis after field cooling from above the Néel temperature, T_N, of the AFM (and below the Curie temperature, T_C, of the FM) in materials composed of FM-AFM interfaces. The transition from a shifted to a centred loop appears close to the Néel temperature of the AFM phase, confirming that it is the presence of the antiferromagnetic material which causes the exchange bias effect. In most systems, the horizontal shift is opposite to the cooling field direction and is therefore called negative exchange bias. Generally, the exchange bias field does not depend markedly on the amplitude of the cooling field. However, studies of FeF_2/Fe and MnF_2 [100] bilayers revealed a rather unusual behaviour. For large cooling fields the loops, instead of shifting towards negative fields (when cooled in a positive field), shifted to positive fields, i.e. in the same direction as the cooling field. This effect is then called positive exchange bias. Different theoretical models have been proposed to explain this effect [100, 101] which are all based on the existence of an antiferromagnetic coupling at the interface between the FM and the AFM layers. Note that for conventional negative exchange bias a ferromagnetic interfacial coupling has usually been assumed. Independent of the direction of the horizontal shift of the hysteresis loop, it is always accompanied by an increase of the coercivity H_c below the exchange bias blocking temperature T_B^{EB} which is linked to the anisotropy of the AFM layer. However, the coercivity is also affected by the thicknesses and microstructures of the FM and AFM layers. This increase of H_c is intuitively simple to understand. For an AFM with small anisotropy, when the FM rotates, it drags the AFM spins irreversibly, hence increasing the FM coercivity. For a large AFM anisotropy, the FM decouples because it cannot drag AFM spins, consequently the coercivity is reduced. A

consequence of the influence of the anisotropy is a peak of coercivity that often appears close to T_B and is due to the decrease of the AFM anisotropy close to T_B. The width of the peak is related to sample homogeneity which reflects the distribution of AFM anisotropies. An analogous peak effect is found in the AFM thickness dependence of H_c [102]. The effective AFM anisotropy is reduced with thickness. For thin AFM films, the exchange bias effect as well as the increase of H_c disappear. Figure 2.12 (a), shows an FM/AFM system at a temperature T that is below the Curie temperature (T_C) of the ferromagnet and above the exchange bias blocking temperature T_B^{EB} of the antiferromagnet ($T_B < T < T_C$). The hysteresis loop of the FM/AFM system at this temperature is equal to the hysteresis curve of the pure ferromagnet plus a small paramagnetic part from the AFM and is shown in 2.12 (b). The hysteresis loop is perfectly centred around the origin. The FM/AFM system is then cooled well below T_B in the presence of a magnetic field H (or in a state where the FM has a remanent magnetisation), which is usually aligned parallel to an easy axis of the FM 2.12 (d). The hysteresis loop of the FM/AFM system in this state is shifted along the field axis, generally in the direction opposite (negative) to the applied cooling field 2.12 (e). Additionally, the hysteresis loop shows a strong increase of the coercivity H_C. Figure 2.12 (c) shows a typical torque magnetometry curve of a ferromagnetic material with uniaxial anisotropy whereas a torque curve of an exchange biased FM/AFM system is shown in 2.12 (f). The uniaxial anisotropy of a ferromagnet gives rise to a sin 2θ behaviour of the torque signal 2.12 (c), whereas the sin θ behaviour of the FM/AFM system is a clear sign for a unidirectional anisotropy 2.12 (f). The energy functions of both systems are represented by the dotted lines in 2.12 (c) and 2.12 (f). It is apparent that in (c) two energy minima occur at $\theta = 0°$ and $\theta = 180°$ and in 2.12 (f) only one at $\theta = 0°$ [101].

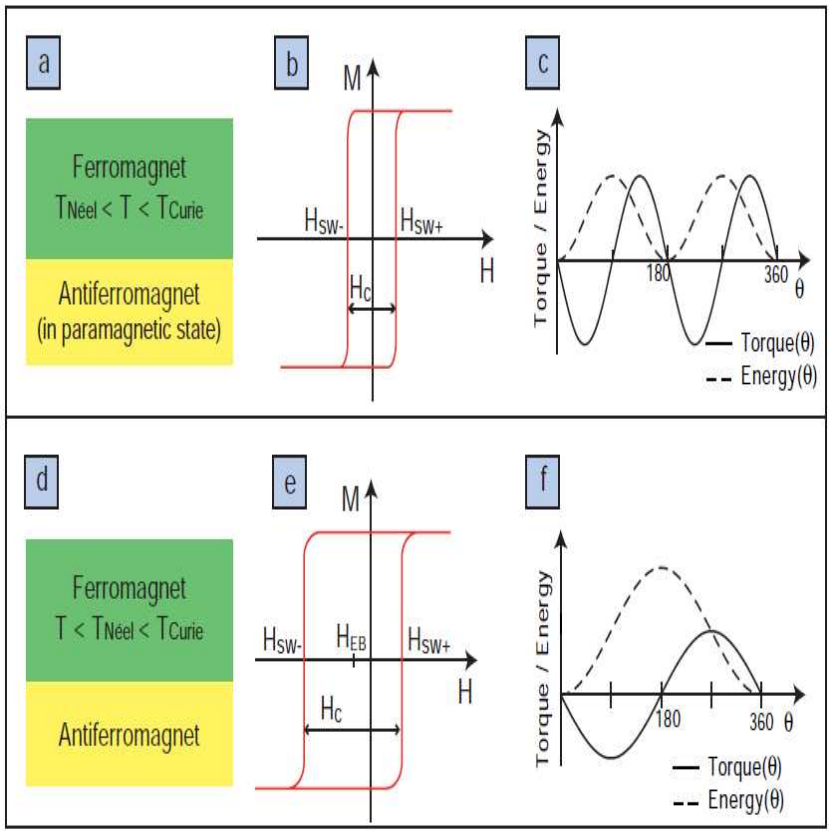

Figure 2.12: Comparison of the magnetic properties of an FM/AFM system at a temperature T with $T_B<T< T_C$ (a), and the same system after field-cooling below the AFMs Néel temperature (d) (with $T <T_B<T_C$). The system (a) shows a normal ferromagnetic hysteresis loop (b) and an uniaxial anisotropy, indicated by a $\sin(2\theta)$ behavior of the torque measurements (d). System (d), after field cooling below T_B, shows a horizontally shifted loop with increased coercivity (e), and an unidirectional anisotropy with a $\sin\theta$ behaviour of the torque measurement.

2.7.2 Training effect

The training effect was first discovered in 1966 by Paccard *et al.* [103] shortly after the discovery of the exchange bias shift by Meiklejohn and Bean. This phenomenon is observed in FM/AFM systems when they are field cycled. In this case, the exchange bias field is found to vary with the number of hysteresis loops. If several consecutive hysteresis loops are measured, the shift H_{EB} of consecutive loops will decrease. It can thus be characterised by the change of the switching fields, H_{sw-} and H_{sw+}, with the

number of hysteresis cycles. H_{sw-} (H_{sw+}) define the field at which the sample magnetisation switches from positive to negative (or negative to positive) values (see Figure 2.13). This empirical variation of the switching fields with the number of consecutive hysteresis loop measurements can be subdivided into three different types. In the first type of exchange biased systems called Type I, the hysteresis loop shrinks from both sides, which means H_{sw-} increases and H_{sw+} decreases. This behaviour of the switching fields corresponds to the one observed by Paccard *et al.* [103]. If both switching fields, H_{sw-} and H_{sw+} increase, the training effect is denoted as Type II [103]. It is not very surprising that an intermediate case between Type I and Type II systems was also found and is denoted as Type 0 training effect [101]. In Type 0 systems H_{sw-} increases, as in Type I and II, and H_{sw-} stays constant. This behaviour is mainly be observed in antiferromagnetic metallic systems such as FeMn and IrMn. The behaviour of Type I, II and 0 training effect in FM/AFM systems is illustrated in Figure 2.13 (a) to (c) respectively. For each Type, the first (red), the second (orange) and fifth (yellow) of the consecutively measured hysteresis loops are shown. Experimentally, it is often found that $H_{EB\infty} \propto 1/\sqrt{n}$ where n indicates the order of consecutive loops measured. It is important to stress that the training effect is more important in antiferromagnetic polycrystalline samples and is very small or non-existent in systems based on single crystals [103].

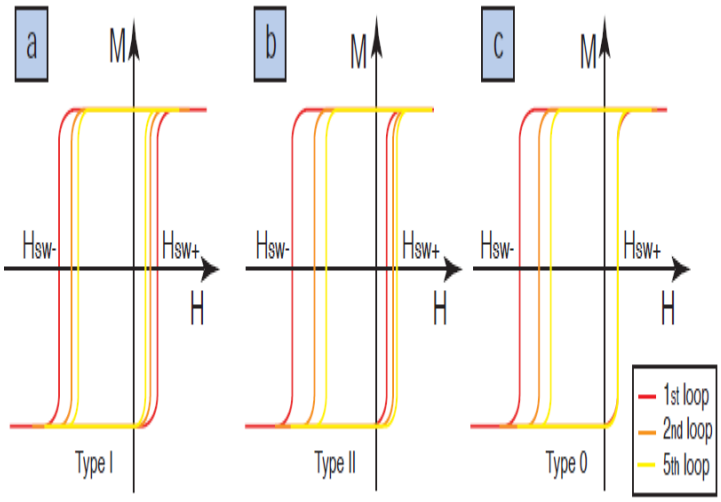

Figure 2.13: Type I, II and 0 training effect for the first (red), second (orange) and the fifth (yellow) hysteresis loop measurement.

Chapter 3

Mössbauer Spectroscopy

3.1 Introduction

Mössbauer spectroscopy is a spectroscopic technique based on the Mössbauer effect discovered by Rudolf L. Mössbauer in 1957 [104]. The technique probes tiny changes in the energy levels of an atomic nucleus in response to its environment. Scientists in different fields such as Physics, Chemistry and Geology use these tiny energy changes to provide useful information about the chemical bonding, structure and magnetic properties of materials [104, 105]. Mössbauer spectroscopy has been widely used in the study of bulk as well as the surface properties of materials [106]. Mössbauer spectroscopy can also be used to study nanostructured materials. It can also provide information on dynamic properties such as superparamagnetic relaxation, diffusion and mechanical vibrations of Mössbauer isotopes in samples. Mössbauer spectroscopy is now a well established experimental technique in the investigation of solids. In a Mössbauer experiment a suitable radioactive source is used as a spectroscopic probing tool. This is achieved by changing the energy of the emission spectrum of the source with respect to that of the absorber (specimen) by moving the source towards and away from the absorber. This tunes the absorber in and out of resonance making it possible to scan through the different absorption lines and measure the hyperfine interactions. In this chapter we present some of the basic principles of the technique.

3.1.1 Mössbauer effect

The phenomenon of the emission or resonant absorption of gamma ray photons without loss of energy due to recoil and without thermal broadening is known as the Mössbauer effect. The important factors which must be considered in order to understand the physical basis of the Mössbauer effect and the importance of recoilless emission of gamma rays are discussed below.

3.1.1.1 Natural line width

Consider the emission of γ-ray photons from an atom corresponding to a transition to the ground state. The emitted gamma rays have a very small spread of energies. The uncertainty in energy corresponds to the width Γ of the nuclear state and can be obtained from the Heisenberg uncertainty relation

$$\Delta E.\Delta t \geq \hbar \tag{3.1.1}$$

where $\hbar = \dfrac{h}{2\pi}$ and h is the Planck's constant and Δt is the time interval to measure the energy E which is in the order of the meanlife τ of the state under consideration. Weiskopf and Wigner showed [107] that by setting $\Delta t \cong \tau$, the approximate width $\mathit{\Gamma} = \Delta\ E$ of a level is given by $\mathit{\Gamma} = \hbar/\tau$ where $\mathit{\Gamma}$ represents the full width of the transition spectral line at half maximum. Further, Weidkopf and Wigner found that the spectral line has a Lorentian or Breit-Wigner shape described by

$$I(E) = (\text{constant})\frac{\mathit{\Gamma}/2\pi}{(E - E_\circ)^2 + (\mathit{\Gamma}/2)^2} \tag{3.1.2}$$

where $I(E)$ is the transition energy intensity and $E_\circ$ represents the most probable transition energy. The width of the transition line is governed by the mean lifetime τ of the excited state. In Mössbauer spectroscopy, the lifetime of excited states range from $\approx 10^{-6}$ to 10^{-11} s, and for ^{57}Fe the mean lifetime for the first excited Mössbauer state is $\tau = 1.43 \times 10^{-7}$ s. The resulting value for the linewidth $\mathit{\Gamma}$ is 4.55×10^{-9} eV.

3.1.1.2 Nuclear resonance

When atoms are held tightly as in solids, the gamma radiation emitted by their nuclei are very close to being recoil-free. This corresponds to the transition energy between the nuclear ground state and the excited state. When the photon carrying the full nuclear transition energy strikes another identical nucleus also embedded in a tight crystalline structure, absorption may occur. Since the absorption in general can occur only for a nucleus in the ground state, only a γ-ray emitted in a transition to the ground state is useful for practical application of the Mössbauer effect. The principle of the Mössbauer effect is illustrated in Figure 3.1 [106]. If a spectral line for the emission

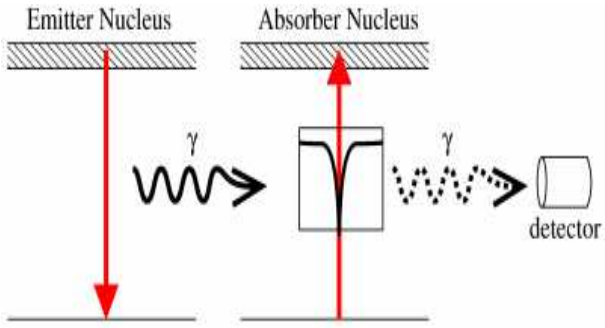

Figure 3.1: Recoiless emission and absorption of a γ-ray.

and absorption processes coincide at the same energy position E_0, then the maximum resonance absorption occurs. The resonance absorption cross-section is given by the Breit-Wigner formula

$$\sigma = \frac{\sigma_\circ \Gamma^2}{[\Gamma^2 + 4(E - E_\circ)^2]} \tag{3.1.3}$$

where $\sigma_\circ$ is the maximum cross-section and is given by

$$\sigma_\circ = \frac{\lambda^2}{2\pi} . \frac{2I_e + 1}{2I_g + 1} . \frac{1}{\alpha + 1} \tag{3.1.4}$$

where I_e and I_g are the nuclear spin quantum numbers for the excited and ground states, respectively. λ is the wavelength of the γ-ray and α is the internal conversion

coefficient (for ^{57}Fe, $\alpha = 8.21$). The nucleus remains in the excited state of energy $E_\circ$ for the mean lifetime after the absorption process and then undergoes a transition back to the ground state by emission of either a γ-ray or conversion electron due to internal conversion (the transfer of the photon energy to an electron in the innermost electron shells of the atom). This process is referred to as nuclear resonance fluorescence.

3.1.1.3 Recoil energy loss

Consider a γ-ray (photon) emitted from an excited nucleus of mass M (initially at rest). This process gives rise to a recoil imparted to the emitting nucleus. As a result the nucleus moves in the opposite direction to the γ-ray emission with a velocity, say $\overrightarrow{v}$ as shown in Figure 3.2 [105, 106]. The kinetic recoil energy is given by $E = \frac{1}{2}Mv^2$. Applying the conservation of momentum to the above process gives

$$p_n = -p_\gamma = -\frac{E_\gamma}{c} \tag{3.1.5}$$

where p_n and p_γ are the linear momenta of the nucleus and the γ-ray, respectively and $E_\gamma = E_\circ$ - E_R. Taking into consideration the large mass of the nucleus and using non-relativistic approximations gives

$$E_R = \frac{p_n}{2M} = \frac{E_\gamma^2}{2Mc^2}. \tag{3.1.6}$$

For $E_R \ll E_\circ$, we can set $E_\gamma \approx E_\circ$ in equation (3.1.6) which reduces to

$$E_R = \frac{E_\circ^2}{2Mc^2}. \tag{3.1.7}$$

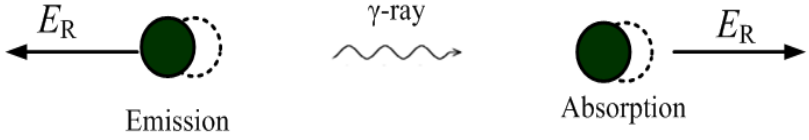

Figure 3.2: Recoil energy E_R received by an isolated nucleus on gamma ray emmission or absorption.

Evaluating equation (3.1.7) into numerical form results in

$$E_R(\text{eV}) = 5.37 \times 10^{-4} \frac{E_\circ^2}{A}, \tag{3.1.8}$$

where A is the atomic mass of the decaying nucleus. For ^{57}Fe, the Mössbauer transition between the first excited state and the ground state ($E_\circ = E_e$ - E_g = 14.4 keV) results in $E_R = 1.95 \times 10^{-3}$ eV.

3.1.1.4 Thermal broadening

During the decay process, the recoil effect causes a displacement from $E_\circ$ by an amount E_R shown in Figure 3.3 [106]. In the absorption process, for the γ-ray to be absorbed by a nucleus requires a total energy of $E_\gamma = E_\circ + E_R$ to make up for the transisition from the ground state to the excited state and the recoil effect. The transition lines for absorption and emission are separated by $2E_R$, which is 10^6 times larger than the natural line width ($\Gamma = 4.55\text{x}10^{-9}$ eV), as a result, the γ-ray emission line does not overlap the absorption line, and the nuclear resonance absorption is not observable. The atoms of a gas are continuously in motion with large velocities. If γ-ray emission occurs while the nucleus (atom) is moving at a velocity v_n in the direction of γ-ray propagation then the γ-ray of energy E_γ receives a Doppler energy E_D given by

$$E_D = \frac{v_n}{c} E_\gamma \tag{3.1.9}$$

which is added to E_γ

$$E_\gamma = E_\circ - E_R + E_D. \tag{3.1.10}$$

The mean Doppler broadening can be determined from [106]

$$\overline{E}_D = E_\gamma \left(\frac{2E_K}{Mc^2} \right)^{\frac{1}{2}} \tag{3.1.11}$$

where E_k is the mean kinetic energy of the moving nucleus (or atom) given by

$$E_K = \frac{1}{2} M v_n^2 = \frac{3}{2} k_B T. \tag{3.1.12}$$

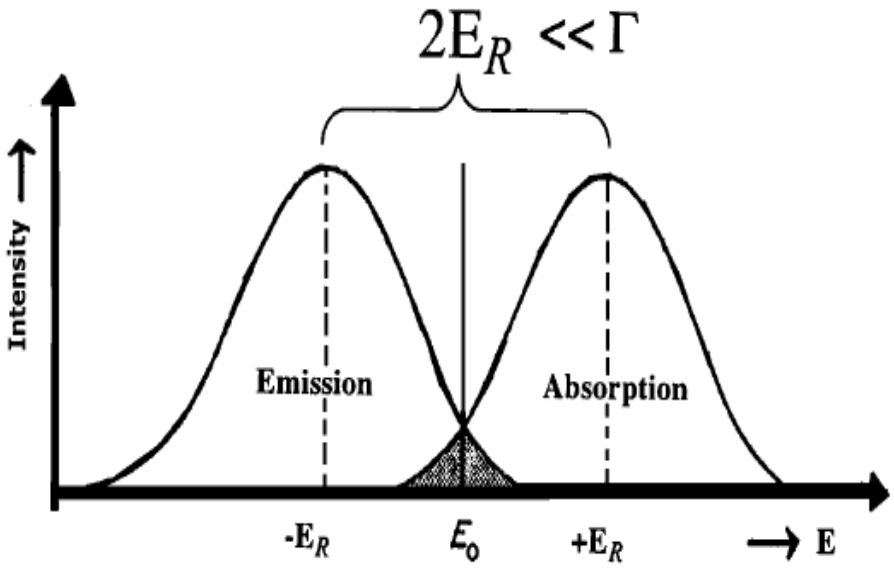

Figure 3.3: Schematic diagram of the recoil effect showing the transition lines for emission and absorption.

Consider an Einstein solid with $3N$ vibrational modes (N is the number of atoms in the solid) each having the same frequency ω_E. The solid is characterized by the quantum numbers of its oscillators and any changes in its state is a result of an increase or decrease in one or more of the quantum numbers. This corresponds to the absorption or emission of quanta of energy $\hbar\omega_E$ which in solids is of the order of 10^{-2} eV. The emission of γ-rays is accompanied by the transfer of integral multiples of this photon energy ($0\hbar\omega_E$, $\pm\hbar\omega_E$, $\pm 2\hbar\omega_E$, ...) to the lattice. Therefore, the fraction of events, f, which takes place without lattice excitation, provided $E_R \ll \hbar\omega_E$ is given by

$$E_R = (1 - f)\hbar\omega_E \tag{3.1.13}$$

and

$$f \cong 1 - \frac{E_R}{\hbar\omega_E} = 1 - k^2 < x^2 > \tag{3.1.14}$$

where $< x^2 >$ is the expectation value of the squared vibrational amplitude in the x-direction and k is the propagation vector [108]. The above equation can be written

in the following general form

$$f = exp\Big(- \frac{E_R}{\hbar\omega_E}\Big) = exp(-k^2 < x^2 >). \tag{3.1.15}$$

From the debye model for solids [106], the recoil-free fraction can be written as

$$f = exp\Big[- \frac{6E_R}{k_B\theta_D}\{\frac{1}{4} + \Big(\frac{T}{\theta_D}\Big)^2 \int_{\circ}^{\theta/T} \frac{x}{e^x - 1}dx\}\Big]. \tag{3.1.16}$$

For $T \ll \theta_D$, the above equation reduces to

$$f = exp\Big(\frac{-6E_RT}{k_B\theta_D^2}\Big), \tag{3.1.17}$$

where $\theta_D = \hbar\omega/\mathrm{k}_B$ is the Debye temperature. The recoil-free fraction, f is referred to as the Debye-Waller factor or Lamb-Mössbauer factor. This factor increases with decreasing recoil energy loss, E_R, decreasing temperature, T and increases with increasing Debye temperature, θ_D. θ_D may be considered as a measure of the strength of the bonds between Mössbauer atom and the lattice. The f-value for the 14.4 keV γ-transition in ^{57}Fe at 0 K can be determined from the above equations to be 0.91.

3.1.2 Hyperfine interactions

Hyperfine interactions are interactions between a nucleus and its surrounding environment that arise from the interactions between the static magnetic and electric moments of the nucleus with the electron charge and spin distributions in its immediate vicinity. These interactions influence the nuclear levels and thus also the transition energies, in a characteristic way and allow valuable information about the absorbing atom and its surrounding to be obtained. These include isomer shift (δ), magnetic quadrupole interaction (Δ) and magnetic hyperfine interaction (H) as illustrated in Figure 3.4 [106].

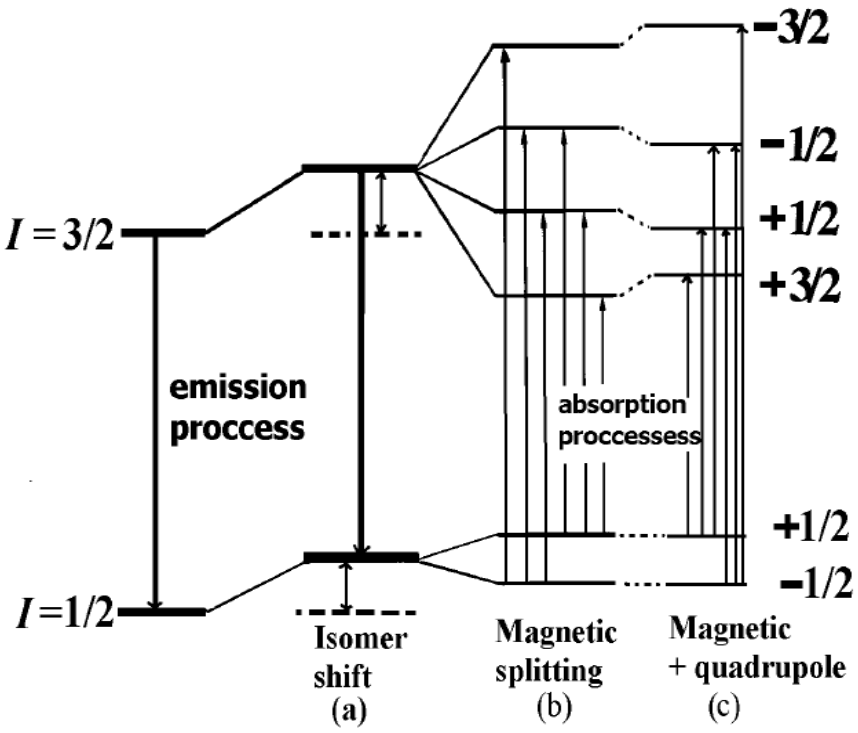

Figure 3.4: Effects of isomer shift, electric quadrupole splitting and magnetic hyperfine splitting on the nuclear energy levels of a free atom.

3.1.2.1 Isomer shift

The isomer shift of absorption lines in a Mössbauer spectrum arises due to the non-zero volume of the nucleus and the electron charge density due to s-electrons within it leading to an electric monopole (Coulomb) interaction which alters the nuclear energy levels. The volume of the nucleus in its ground and excited states are different and the s-electron densities are affected by the chemical environment. This relationship between s-electron density and nuclear radius is given by

$$\delta = \frac{2}{5}\pi Z e^2 \Big(|\varphi_s(0)|_E^2 - |\varphi_s(0)|_A^2 \Big) \Big(\langle R_e^2 \rangle - \langle R_g^2 \rangle \Big) \tag{3.1.18}$$

where $\langle R_g^2 \rangle$ and $\langle R_e^2 \rangle$ are the mean square radii of the ground and excited state nuclear states, $|\varphi_s(0)|_E^2$ and $|\varphi_s(0)|_A^2$ are the electron densities at the emitting and absorbing nuclei and Z is the atomic number [104, 105, 109]. Any difference in the s-electron environment between emitter and absorber thus produces a shift in the resonance

energy of the transition. This shift cannot be measured directly and so a suitable reference is necessary, such as a specific source or an absorber. The isomer shift is good for probing the valence state of the Mössbauer atom. As the wavefunctions of the s-electrons penetrate into outer shells, changes in these shells will directly alter the s-electron charge density at the nucleus. For example, Fe^{2+} and Fe^{3+} have electron configurations of ($3d^6$) and ($3d^5$) respectively. The ferrous ions have less s-electron density at the nucleus due to the greater screening of the d-electrons. This produces a positive isomer shift greater in ferrous iron than in ferric.

3.1.2.2 Quadrupole splitting

The existence of an electric quadrupole interaction is one of the most useful features of Mössbauer spectroscopy. The theory is closely related to that used in nuclear quadrupole resonance spectroscopy [104]. A nucleus that has a spin quantum number $I > \frac{1}{2}$ has a non-spherical charge distribution. The magnitude of the charge deformation, Q, is given by

$$eQ = \int \rho r^2 (3cos^2\theta - 1) dr \tag{3.1.19}$$

where e is the charge of the proton, ρ is the charge density in a volume element $d^3\overrightarrow{r}$ at a distance r from the center of the nucleus and making an angle θ to the nuclear spin quantisation axis. The sign of Q indicates the shape of the deformation. Negative Q is due to the nucleus being flattened along the spin axis, an elongated nucleus gives a positive Q. An assymetric charge distribution around the nucleus causes an assymetric electric field at the nucleus, characterised by a tensor quantity called the Electric Field Gradient (EFG), $\bigtriangledown\overrightarrow{E}$. The electric quadrupole interaction between these two quantities gives rise to a splitting in the nuclear energy levels. The interaction between nuclear moment and EFG is expressed by the Halmitonian

$$\overrightarrow{H_{Eq}} = -\frac{1}{6} eQ \bigtriangledown^2 \overrightarrow{E} \tag{3.1.20}$$

where $\bigtriangledown^2\overrightarrow{E}$ may be written as [108]

$$V_{ij} = \frac{\partial^2 V}{\partial x_i \partial x_j} \tag{3.1.21}$$

$x_i, x_j = x, y, z$ where V is the electrostatic potential. There are two contributions to EFG i) lattice contributions from charges on distant ions and ii) valence contributions due to incompletely filled electron shells. If a suitable coordinate system is chosen the EFG can be represented by three principal axes V_{xx}, V_{yy} and V_{zz}, if an asymmetry parameter is defined using these axes as [104]

$$\eta = \left(\frac{V_{xx} - V_{yy}}{V_{zz}}\right) \tag{3.1.22}$$

where $|V_{xx}| \geq |V_{yy}| \geq |V_{zz}|$ so that $0 \leq \eta \leq 1$. The EFG can be specified by two parameters: V_{zz} and η. The Hamiltonian for the quadrupole interaction can be rewritten as

$$H_{Eq} = \frac{e^2qQ}{4I(2I-1)}\left[3I_z^2 - I(I+1) + \frac{\eta}{2}(I_+^2 + I_-^2)\right] \tag{3.1.23}$$

where I_+ and I_- are shift operators and I_z is a spin operator [85, 109]. The excited state of ^{57}Fe has a spin $I = 3/2$. The EFG has no effect on the $I = 1/2$ ground state but does remove degeneracy in the excited state, splitting it into two sub-states $m_I = \pm 1/2$ and $m_I = \pm 3/2$ states are higher in energy for positive V_{zz}. The energy eigenvalues for $I = 3/2$ have exact solutions given by

$$E_{Eq} = \frac{e^2qQ}{4I(2I-1)}\left[3m_I^2 - I(I+1)\right](1 + \frac{\eta^2}{3})^{\frac{1}{2}} \tag{3.1.24}$$

whilst the energies for higher spin states require analytical methods to calculate the energies. The now non-degenerate excited states give rise to a doublet in the Mössbauer spectrum as illustrated in Figure 3.4. The separation between the lines, Δ, is known as the quadrupole splitting and is given by

$$\Delta = \frac{e^2qQ}{2}\left(1 + \frac{\eta^2}{3}\right)^{\frac{1}{2}} \tag{3.1.25}$$

with the lines intensities being equal for polycrystalline samples.

3.1.3 Magnetic Hyperfine Splitting

Magnetic hyperfine splitting is caused by the dipole interaction between the nuclear spin moment and a magnetic field i.e. Zeeman splitting. The effective magnetic field experienced by the nucleus is a combination of fields from the atom itself, from the lattice through crystal field effects and from external applied fields. This can be considered for now as a single field, B, whose direction specifies the principal, z axis. The Hamiltonian for the magnetic hyperfine dipole interaction is given as

$$H = -\mu.B = -g\mu_N I.B \tag{3.1.26}$$

where μ_N is the nuclear Bohr magneton, μ is the nuclear magnetic moment, I is the nuclear spin and g is the nuclear g-factor [85]. This Hamiltonian yields eigenvalues of

$$E_M = -g\mu_N B m_I \tag{3.1.27}$$

where m_I is the magnetic quantum number representing the z component of I (where $m_I = I, I-1, ..., -I$). The magnetic field splits the nuclear level of spin I into $(2I+1)$ equispaced non-degenerate substates. This and the selection rule of $\Delta m_I = 0, \pm 1$ produces splitting and a resultant spectrum for a $3/2 \rightarrow 1/2$ transition in the case of ^{57}Fe.

Chapter 4

Experimental techniques

4.1 Introduction

Mixed metal oxides can be produced by solid state reaction and high energy ball milling from high purity oxides. Wet chemical methods such as sol-gel [110], hydrothermal [25], [26], glycothermal [9], citrate precursor [82, 83] and combustion methods [8, 82, 83] can also be used to produce better quality materials from salt solutions. The samples studied here were made by using hydrothermal techniques. High energy ball milling was used to reduced the particle sizes of the samples. The single phase corundum structure in all the synthesized samples was confirmed by X-ray diffraction. The magnetic properties were studied using ^{57}Fe Mössbauer spectroscopy, vibrating sample magnetometer (VSM) and superconducting quantum interference device (SQUID) magnetometer. The experimental procedures for synthesis and measurement of certain basic properties are presented in this chapter.

4.2 Hydrothermal Process

The hydrothermal process is one of the common techniques of synthesizing compounds from aqueous solutions of metal salts. The starting materials in this method are high-purity metal chlorides or nitrates and a precipitating reagent such as ammonia, sodium

hydroxide or potassium hydroxide. The stirring, reaction temperature, pressure and washing stage play important roles in obtaining homogeneous and single-phase crystallization of the compounds. We have prepared (Sn, Mn, Mg)$_{0.2}$ Cr$_{1.8-x}$ Fe$_x$ O$_3$ compounds by hydrothermal technique. The starting materials were $SnCl_2.6H_2O$ (99%), $MnCl_2$ (99.99%), $MgCl_2$ and $FeCl_3.6H_2O$ (99%) which were supplied by Sigma Aldrich. The stoichiometric compositions were calculated to yield a target mass of 5.0 g. The chlorides were mixed in deionised water by a magnetic stirrer for about 30 minutes. The precipitation reagent were added drop-wise to the salt mixtures until complete precipitation. The precipitate was washed several times over Whatman GF/F microfiber filters by deionised water until all the chloride ions were removed as confirmed by using a standard solution of $AgNO_3$. The precipitate was finally dispersed in about 400 ml of deionised water. The samples were synthesized in a model 4843 PARR pressure reactor as shown in Figure 4.1 or in an open glass reflux system at atmospheric pressure as shown in Figure 4.2 [111].

submitted

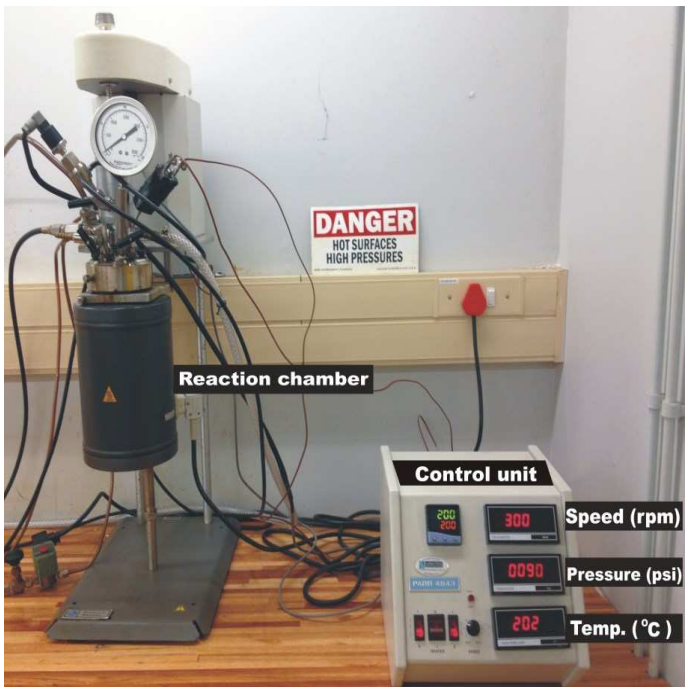

Figure 4.1: The stirred pressure reactor with a PARR 4843 controller.

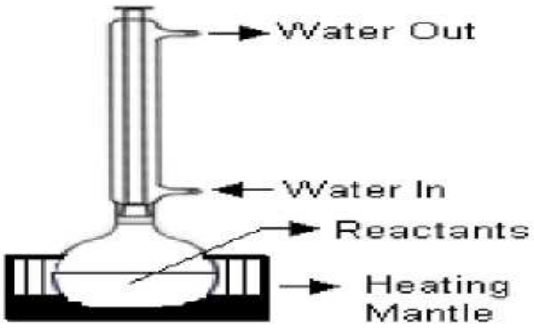

Figure 4.2: Diagram of reflux apparatus.

The reactor was operated at a soak temperature of 100 °C for 3 hours at a stirring speed and pressure of 300 rpm and 120 psi respectively. The operating schedule and the set-up configurations of the PARR 4843 pressure reactor are shown respectively in Figure 4.3 and in Table 4.1 [111]. The cooled final product was finally filtered over fresh Whatman microfiber and rinsed with 200 ml of ethanol. The ethanol drives out the water from the sample and is easier to remove from the sample by drying. The synthesized oxides were dried under 250 W infrared light for 3 hours. The dried samples were homogenized into fine powder using an agate mortar and pestle. A typical mass of 4.73 g of the oxides was produced. The difference in the target mass and actual mass recorded was a result of some samples being lost during the synthesis process. The sample was finally sintered at 600 °C for 12 hours in order to achieve single phase formation.

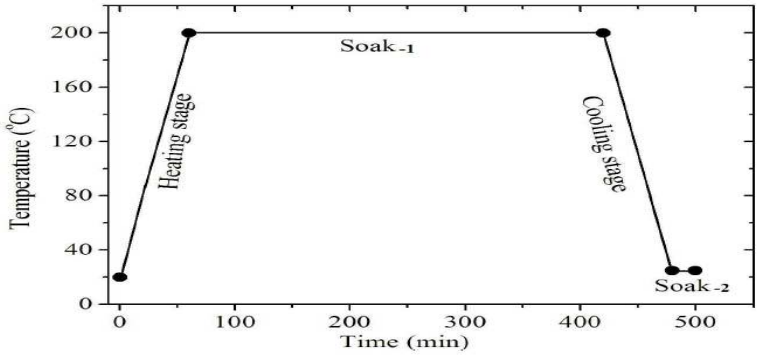

Figure 4.3: The operation schedule of the PARR 4843 pressure reactor.

Table 4.1: The general and special set-up configurations of the PARR 4843 controller for the pressure reactor.

(i) general fixed settings.				
$Level_1$	$Level_2$	$Level_3$	$Level_A$ $level_C$	
tune: off	SP1.P: 97	SP1:d: ssd	An.hi: 997	
bAnd: 9.9	hAnd: off	SP2:d: rLK	An.Lo: 0	bAud: 9600
int.t: 4.8	PL.1: 100	Burn: uP.SC	hi.in: 50.0	dAtA: 18nl
aEr.t: 100	PL.2: 100	rEU.d: lr.2d	lo.10.0	abuC: off
aAC: 1.5	SP2.A: Cool	rEU.L: in.2n	dECP: 0000	
CYC.t: 20	SP2.b: none	SPAn: 0.0	SP3.A: none	
oFSt: 0	diSP: 1o	2Ero: 0.0	SP3.b: none	
SP.LK: off	hi.SC: 800	ChEK: off	SET.3: 0	
SEt.2: 0	LO.SC: 0	rEAd: UAro, 0.0	hK5.3: 2.2	
Bnd.2: 2.0	inPt: tCL	tECh: CtA, 0.0	brn.3: UP.SC	
CYC.2: on.off	unit: psi	UEr: 954.0	rEU.3: 3d	
		rSEt: none		
(ii) Special variable settings.				
$Level_1$	$Level_2$	$Level_3$	$Level_A$ $level_C$	
Run: (on or off)	Type: Spr	Type: Soak or	Type: Spr	Type Soak
FAiL: rSET, CONT	Sprr: 200	Step or Loop or	SPrr: 200 degree	Sin: 10 min
or hold	t.SP: 150	CALL or E.op	t.SP: 25 degree	E.oP: none
St.U: PU	hb.U: off	Edit: dEL	hb.U: off	
SPru: hour		Sint: 360 (6hrs)		
or 60 s		E.op: none		

4.3 High-energy ball milling

High-energy ball milling is a simple and effective method for producing compounds and alloys by mechanical synthesis method. In this technique the required proportions of the starting materials are mixed and sealed in hardened steel vials with steel balls. Agents like stearic acid or acetone may be added to the mixture or simply dry milled [112]. The milling time required to form the sample depends on the ball to sample mass ratio, the speed at which the vials are rotated and ease of phase formation of the target material. We have used a Retsch planetary ball mill type PM 400 MA shown in Figure 4.4 for particle size reduction for some of our samples. This facility has four grinding stations and can be operated to a maximum speed of 300 rev/min. The recommended

speed is 200 rev/min for long grinding periods. The grinding environment consists of 250 ml hardened steel vials with an appropriate number of balls that depends on the sample size. We have used suitable covers of the vials available to allow for grinding in air or inert gas atmosphere. The ball to sample mass ratio used was 20:1. The sample size in each vial was about 2 g. A typical grinding schedule was for a total time of at least 4 hours at a speed of 200 rev/minute. At conveniently selected times (for example 1, 2, 3 and 4 hours) about 0.2 g of sample was removed in order to study the effect of particle size reduction [112].

Figure 4.4: Retsch PM 400 planetary ball mill used at the Condensed Physics laboratory, UKZN.

4.4 X-ray Powder Diffraction

X-ray powder diffraction (XRD) is a rapid analytical technique primarily used for phase identification of a crystalline material and can provide information on unit cell dimensions and quality of the sample. X-ray diffraction is based on constructive interference of monochromatic X-rays in a crystalline sample. These X-rays are generated by a cathode ray tube, filtered to produce monochromatic radiation, collimated to concen-

trate, and directed towards the sample. The interaction of the incident rays with the sample produces constructive interference when the condition for Bragg's law

$$n\lambda = 2dsin\theta \tag{4.4.1}$$

is satisfied. n is an integer related to the order of the diffraction, λ is the x-ray wavelength, d is the perpendicular distance between lattice planes and θ is the Bragg's angle [113]. The XRD measurements were performed on a Philips X-ray diffractometer type PW 1710. A typical sample size for XRD measurement was 0.20 g. This was loaded on a standard sample holder by using a glass slide. The top of the powder was flattened without pressing by the edge of a glass slide. The diffractometer uses a monochromatic beam of CoKα radiation with an average wavelength 1.7903 Å. The XRD measurements were scanned in the range of 2θ from 20° to 80° in steps of 0.01°. The lattice parameters were obtained by refinement of XRD data by a Rietveld analysis (FullProf Suite for Windows). The peak broadening of the most intense 311 peak was used to estimate the crystallite average sizes by the Scherrer formula [114]

$$D = \frac{K\lambda}{\beta cos\theta}, \tag{4.4.2}$$

where K is a crystal shape factor near unit and β is the full width at half maximum (FWHM) of the peak. We used a K value of 0.9 ± 0.1 corresponding to nearly spherical crystallites with corundum structure. Figure 4.5 shows a schematic diagram of the mechanical assembly of an Empyrean PAN analytical diffractometer type PW 1710 with CoKα radiation source operated over a 2θ range from 10^o to 80^o. ω is the angle of incidence of the X-rays [115]. The XRD machine used for the current set of measurements is shown in Figure 4.6. Most modern X-ray diffractometers include software for peak profile fitting. This software greatly helps in calculating the intensities, positions, widths, shapes of the peaks and takes into account the broadening of the peaks. To apply the proper correction for the instrumental broadening, the shape of the peak has to be chosen. The two most commonly assumed line shapes are the Lorentzian and

Gaussian [116]. The instrumental broadening was corrected using a Lorentzian line shape in our case.

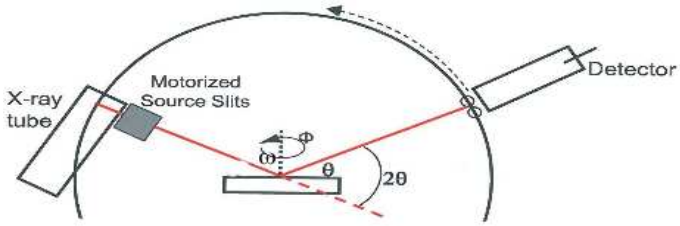

Figure 4.5: Mechanical assembly of a typical 2θ coupled X-ray diffractometer.

Figure 4.6: PW 1710 Empyrean PANalytical X-ray diffractometer, Geology (WC), UKZN.

4.5 Rietveld refinement details

Rietveld refinement of these compositions were carried out using the XRD data with a Rietveld refinement program FULLPROF [117]. Rietveld refinement has nothing to do with structure determination. To start refining a structure an initial model (even if incomplete) is necessary. This model is supposed to be obtained from a crystal structure solver program or by any other means. Special tutorial documents on Rietveld refinement are included in the distribution of FullProf. The best to start working with FullProf is to edit a previously existent PCR-file and modify it as wished. The background was fitted with 6-Cofficient polynomial function, while the peak shapes were described by pseudo-Voigt profiles. In all the refinements, scale factor, lattice parameters, positional coordinates (x, y, z) and thermal parameters were varied. Occupancy parameters of all the ions were kept fixed during refinement. No correlation between the positional and thermal parameters was observed during refinement and as such it was possible to refine all the parameters together. For more information on how to use the programme, the Commission on Powder Diffraction of the International Union of Crystallography has published some guidelines for Rietveld refinement [117]. The PCR file used in the present work is given Table 4.2.

Table 4.2: PCR file for the as-prepared samples of $Sn_{0.2}Fe_xCr_{1.8-x}O_3$.

COMM $Sn_{0.2}Fe_xCr_{1.8-x}O_3$																		
! Current global Chi2 (Bragg contrib.) = 80.21																		
! Files => DAT-file: smooth1.dat, PCR-file: C3Cr																		
!Job	Npr	Nph	Nba	Nex	Nsc	Nor	Dum	Iwg	Ilo	Ias	Res	Ste	Nre	Cry	Uni	Cor	Opt	Aut
0	5	1	0	0	0	0	0	0	0	0	0	0	0	0	0	0	0	1
!Ipr	Ppl	Ioc	Mat	Pcr	Ls1	Ls2	Ls3	NLI	Prf	Ins	Rpa	Sym	Hkl	Fou	Sho	Ana		
0	0	1	0	1	0	4	0	0	-3	10	1	1	0	0	1	1		
! Lambda1	Lambda2	Ratio	Bkpos	Wdt	Cthm	muR	AsyLim	? Rpolarz		2nd-muR								
1.540500	1.544400	0.49700	10.000	6.0000	0.8000	0.0000	100.00	0.0000	0.0000									
Cr2O3(Sn)																		
!																		
!NCY	Eps	R_{at}	R_{an}	R_{gl}	Thmin	Thmax	PSD	Sent0										
10	0.10	1.00	1.00	1.00	1.00	20.0600	0.010002	80.0000	0.000	0.000								

2 !Number of refined parameters

! Zero	Code	SyCos	Code	SySin	Code	Lambda	Code	MORE	− >Patt 1
-0.04654	21.0	0.00000	0.0	0.00000	0.0	0.000000	0.00	0	
! Background	coefficients	/codes	for Pattern 1	(Polynomial	of 6th degree)				
0.000	0.000	0.000	0.000	0.000	0.000				
0.00	0.00	0.00	0.00	0.00	0.00				

! Data for PHASE number: 1 ==> Current R Bragg for Pattern 1: 80.48

Cr2O3(Sn)

!	0	0	0	0	0	577175.000	0	5	0
	R -3 c < −−Space group symbol								
!Atom	Typ	X	Y	Z	Biso	Occ	In	Fin	Nt	Spc/Codes
Cr1	Cr+3	0.00000	0.00000	0.34690	0.50000	9.32500	0	0	0	0
		0.00	0.00	0.00	0.00	0.00				
Fe	Cr+3	0.00000	0.00000	0.34690	0.50000	1.86500	0	0	0	0
		0.00	0.00	0.00	0.00	0.00				
Sn1	Sn+4	0.00000	0.00000	0.34690	0.50000	0.54000	0	0	0	0
		0.00	0.00	0.00	0.00	0.00				
Sn2	Sn+4	0.00000	0.00000	0.00000	0.50000	0.27000	0	0	0	0
		0.00	0.00	0.00	0.00	0.00				
O1	O-2	0.30800	0.00000	0.25000	0.50000	18.00000	0	0	0	0
		0.00	0.00	0.00	0.00	0.00				

!− − − − − − − > Profile Parameters for Pattern 1

0.67842E-08	0.00010	0.00000	0.00000	0.00000	0.00000	0	
11.00000	0.000	0.000	0.000	0.000	0.000		
!U	V	W	X	Y	GauSiz	LorSiz	Size-Mode
0.020000	-0.010000	0.020000	0.000000	0.000000	0.000000	0.000000	0
0.000	0.000	0.000	0.000	0.000	0.000	0.000	
! a	b		c	alpha	beta	gamma	Cell Info
4.969601	4.969601	13.617000	90.000000	90.000000	120.000000		
0.00000	0.00000	0.00000	0.00000	0.00000	0.00000		
! Pref1	Pref2	Asy1	Asy2	Asy3	Asy4		
0.00000	0.00000	0.00000	0.00000	0.00000	0.00000		
0.00	0.00	0.00	0.00	0.00	0.00		
! 2Th1/TOF1		2Th2/TOF2		Pattern to plot			
20.060		80.000		1			

4.6 Transmission Electron Microscopy

Transmission electron microscopy (TEM) is a technique that uses a beam of elecrons transmitted through ultra-thin specimens. An image of the atomic arrangement is formed through the interaction of the transmitted electrons with the specimen. TEM is capable of imaging at a significantly high resolution than light microscopes owing to the small de Broglie wavelengths of the electrons. This enables the instrument's user to examine fine details even as small as a single column of atoms [118]. TEM forms a major analysis method in a wide range of fields such as biological sciences, material science and nanotechnology. TEM has been extensively used to examine the structure and the crystalline defects such as cracks, dislocations in the compounds such as metals, alloys, ceramics, glasses, polymers, semiconductors and mixtures of these materials [119]. TEM appears in several types of equipment such as high-resolution electron microscopy (HRTEM), scanning transmission electron microscopy (STEM) and atomic electron microscopy (AEM). When extended to HRTEM, information on individual atomic planes or columns of the atoms can be obtained. In TEM, images of the samples can be obtained on suitably prepared thin specimens by appropriate lenses which gather information from very small regions of the sample. The images are formed from the interaction of electrons with the sample. The specimen must be thin enough to transmit electrons and to allow enough intensity of electrons to fall on a fluorescent screen. The maximum resolution of a TEM is limited by the wavelength of the probing source and the aperture of the system. A TEM facility consists of four main components namely an electron optical column, vacuum system, electronics and control software. We have used a type Jeol-JEM 1010 shown in Figure 4.7 to study the microstructure and to estimate the particle sizes of some of our samples. A small sample size of about 0.0002 g was dispersed in ethanol and vibrated in a 80Hz\40 Watt transistorized sonic cleaner for 3 minutes. A copper thin film sample holder with

diameter of about 0.0005 mm is dipped into the dispersed sample and loaded in the equipment in order to produce scanned images of the sample.

Figure 4.7: Joel-JEM-1010 high-resolution transmission electron microscope, EM Unit (WC), UKZN.

4.7 Mössbauer measurements

4.7.1 Experimental set-up

The basic experimental set-up for Mössbauer Spectroscopy consists of several components as shown by the block diagram in Figure 4.8. A suitable radioactive source is used as a spectroscopic tool. This is achieved by changing the energy of the emission spectrum of the source with respect to that of the absorber (specimen) by moving the source towards and away from the absorber. This is equivalent to Doppler shifting the energy of the γ-rays. This tunes the absorber in and out of resonance making it possible to scan through the different absorption lines and measure the hyperfine interactions. There are different approaches used to measure γ rays at different energies (velocities). In a constant velocity Mössbauer spectrometer [104], [120], the transmitted photons through a sample in a fixed time interval are measured at constant velocity. The Mössbauer spectrum is accumulated as constant velocity is changed. In this way the spectrum is scanned stepwise, one velocity at a time. The constant velocity spectrometer consists of γ ray detection system, a timer and a scaler for registering accumulated counts at each velocity. Although this is considered to be less expensive than the velocity-sweep experiment, it is tedious to operate unless it is fully automated. Moving the source at constant velocity with high reproducibility and stability while restricted to small amplitude of movement is also not easy to achieve. ^{57}Fe Mössbauer spectroscopy employed here uses a conventional spectrometer with a ^{57}Co source sealed in Rh matrix which is vibrated at constant acceleration. The Mössbauer spectrum develops with time as counts are accumulated as a function of the velocity of the source. The Mössbauer spectra were calibrated against a natural iron (α-Fe) absorber foil with thickness of about 0.025 mm and purity 99.5%. Isomer shifts are calculated with respect to the α-Fe absorber. At least 1 million passes were recorded for one spectrum to be analyzed. The accumulated data at room temperature were interpreted as spectra

and displayed on the output screen of the computer using MCS-32 software version 2.13 (Ortec). The data were fitted using Recoil Mössbauer analysis software [121].

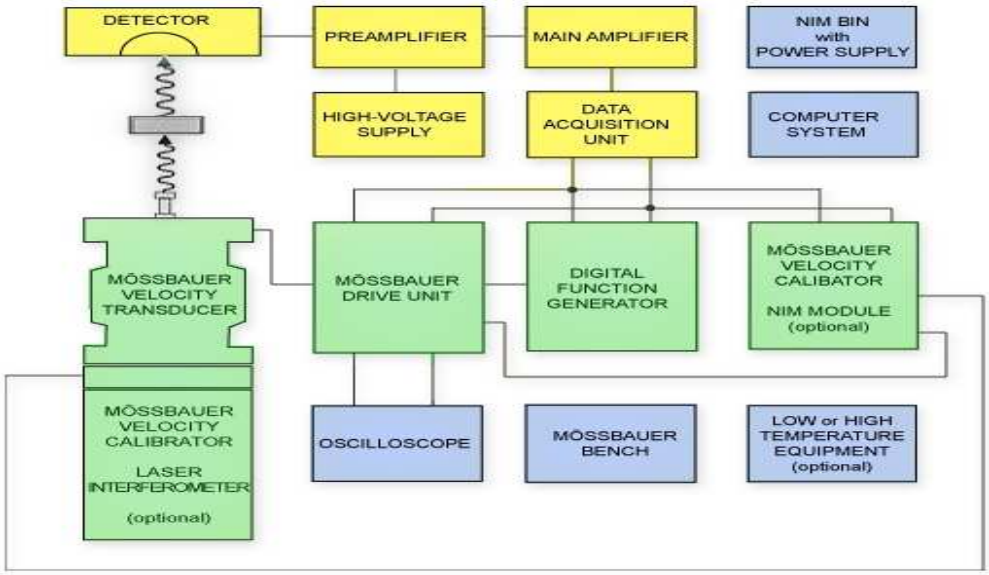

Figure 4.8: Experimental set-up of a Mössbauer spectrometer.

4.8 Magnetization measurements

4.8.1 Vibrating sample magnetometer

A vibrating sample magnetometer (VSM) is an instrument that is widely used to measure magnetic properties. In Figure 4.9 we show the LakeShore model 735 VSM equipment used in this work [122]. The system consists of a 735 VSM controller and the vibrating head mounted above the Janis helium cryostat. The bottom neck of the cryostat is centered between the pole faces of the electromagnet. Pick-up coils are mounted on the faces of the poles of the electromagnet. Other critical components of the system include a 642 bipolar electromagnet power supply, 340 temperature controller, 450 Gaussmeter, a NESLAB ThermoFlex 2500 chiller and a National Instrument IEEE-488 interface card installed in a desktop computer for data collection. The principle of operation of a VSM is based on Faraday's law of induction which defines the induced

voltage produced in the pick-up coils that is proportional to the magnetization of the sample. In Faraday's law

$$\frac{d\Phi}{dt} = -E \tag{4.8.1}$$

where $\frac{d\Phi}{dt}$ is the rate of change of magnetic flux and E is the induced voltage. This induced voltage is proportional to the magnetic moment of a sample and hence its magnetization. A VSM works by detecting the voltage induced by a varying field associated with a vibrating sample. The calibration was done with a standard high-purity (99.995 %) spherical nickel sample of known saturation magnetization (M_S = 54.7 emu/g) [123]. After the calibration, the sample to be measured was placed in a cylindrical sample holder which is screwed to the lower end of a vibrating sample rod. The rod was gently lowered into the sample space to the final position of the sample between the pick-up coils. The data was collected using the interface card and the data acquisition software installed on the computer [124]. The $M - H$ curves obtained were then analyzed using Origin software for windows.

Figure 4.9: Lakeshore 735 vibrating sample magnetometer, Condensed Matter Physics Lab (WC), UKZN.

4.8.2 Mini cryogen free system

A mini cryogen free system (CFS)(purchased from Cryogenic Ltd,UK) used in this work consists of a cryo-cooler system, variable temperature insert (VTI), electronics rack, measurement systems software installed on a desktop computer and superconducting magnet. The operating system is similar to that of the VSM for magnetization measurements. However, it has the potential to measure magnetic fields up to 5 tesla with a temperature range of 1.6 K to 700 K. The VTI provides the option of varying the sample temperature. In addition the CFS has inserts for high temperature VSM, AC susceptibility, resistivity and Hall effect measurements. Only the VSM low temperature option was used in the present set of measurements. The calibration for magnetization measurement on this system was done using yttrium iron garnet sphere. Procedures such as evacuating the VTI, helium gas inlet, helium dump, vacuum, and recharging the dump were carried out to avoid possible contamination in the helium dump and sample space by air. The procedures are discussed in manuals. The operation of the system is carried out by software commands using a LabVIEW graphical programming software interface. Only procedures such as disconnection-reconnection of hoses and sample mounting are done manually. Figure 4.10 shows the set up of the mini cryogen-free VTI system used for measurements. The sample preparation and loading is different from that of the LakeShore VSM. A small amount of 0.005 g of sample is required for measurements. The sample was loaded into a Perspex cone and held fixed by cotton wool to avoid torque. The loaded Perspex cone was guided into an 80 mm length of straw through a slit made at a position of about 20 mm on the straw. The position of the sample in the cone was fixed around the 20 mm position which was firmly held together with the straw by a piece of Kapton tape.

Figure 4.10: Mini cryogen-free VTI system, Condensed Matter Physics Lab (WC), UKZN.

The straw was then screwed to the probe rod using the adaptor provided on the rod and mounted into the airlock position shown in Figure 4.11. The lowering of the sample probe into the sample space was prompted by series of commands from the sample load option in the software menu. The sample load option was selected from the menu window. This prompted an automatic series of commands such as flushing the air space with helium gas, setting the sample space up to operating pressure and vibration of the sample rod. After the centring of the sample, the required temperatures and fields for measurements were entered using the edit sequence command from the menu window. Finally the measurements were executed using the execute sequence command. The low temperature magnetizations are performed under field cooling (FC) and zero field cooling (ZFC). For the ZFC magnetization curve, the sample is first cooled in a zero field from room temperature to the lowest temperature. Then a magnetic field is applied and the magnetization can be measured as a function of temperature while warming the sample to room temperature. In FC, the sample is cooled in a field to the lowest temperature. The magnetization curve is obtained in the same field while increasing the temperature of the sample. Three magnetization setups were used in the present work. This was based on available resources during the course of the study.

Figure 4.11: VTI VSM probe attached to a sample, Condensed Matter Physics Lab (WC), UKZN.

Chapter 5

Structure and magnetic properties of $Sn_{0.2}Fe_xCr_{1.8-x}O_3$ nano oxides

In this chapter we present work that has been published in the Journal of Magnetism and Magnetic Materials 385 (2015) 282-285. $Sn_{0.2}Fe_xCr_{1.8-x}O_3$ nano oxides were produced by hydrothermal process. The following results are presented: (XRD) and TEM measurements confirming the single corundum structure and nanophase structure. The variation of coercive field with particles size reveals that the coercive field achieves a maximum at a critical particle size. These results show evidence of transformation from multi-domain to single-domain structure.

5.1 Introduction

In this chapter, we investigate the structural and magnetic properties of $Sn_{0.2}Fe_xCr_{1.8-x}O_3$ alloys synthesized via hydrothermal route. These alloys are derived from the structure of hematite (α-Fe_2O_3) which has attracted the attention of chemists and physicists alike for many years [22]. The crystal structure is that of corundum (α-Al_2O_3) with a closed-packed oxygen lattice and Fe^{3+} cations in octahedral sites. This alloy is antiferromagnetic below the Morin transition at $T = 250$ K and undergoes a transition above the Morin temperature to a weak ferrimagnetic state as a result of spin cant-

ing, before finally becoming paramagnetic at high temperatures $T \geq 948$ K [18], [125]. The introduction of dopants modifies the magnetic properties of the alloy. The dopant metal ions substitute for Fe^{3+} in the corundum-related structure of α-Fe_2O_3 with the consequent formation of cationic and anionic vacancies [48], [55]. The difference in ionic radii between the dopant metal ion and that for Fe^{3+} will influence the structural characteristics and phase behavior of the doped system. The tin-doped α-Fe_2O_3 alloys have been found to exhibit sensing properties for gases such as methane and carbon monoxide [46, 65]. It is well known that small particle size and large surface area can improve the performance of materials used as sensors or catalysts and that the particle size and surface area are related directly to the preparation method and conditions. Below a critical size the domain structure of the particles changes from multidomain to single domain behavior [126] resulting into interesting magnetic properties [127, 128]. In general, upon reduction in the size D, ferromagnetic materials become magnetically harder and exhibit increased coercivity. However, below a certain size, the coercivity is observed to decrease and soft magnetism begins to prevail. This appears to be a common feature for metal oxides [126, 128, 129] and Fe-based alloys [130]. In Fe-based mechanically alloyed nanocrystalline materials, the coercive field H_C is found to follow a D^6 power law relation [130], while other size dependences of H_C have also been observed in iron oxides [127], [128].

Hematite α-Fe_2O_3 has shown potential as a photoanode for water splitting because it possesses several desirable properties [49, 131]. The synthesis and characterisation of tin-doped iron oxides and tin-doped chromium oxides have been reported previously [77, 132, 133]. Although there have been several studies of the α-$Fe_{2-x}Cr_xO_3$ [39, 75, 76] system, there appears to have been little activity in the doping of these materials by tin. Berry *et al.* [77] have examined the magnetic interactions in tin-doped α-$Cr_2Fe_xO_3$ by ^{57}Fe and ^{119}Sn-Mössbauer spectroscopy. Following this work, we present a more detailed account of magnetic interactions in $Sn_{0.2}Fe_xCr_{1.8-x}O_3$. We

have investigated how single phase formation is influenced by various factors such as the synthesis method, conditions and route. In this respect, $Sn_{0.2}Fe_xCr_{1.8-x}O_3$ nanomaterials have been synthesized by hydrothermal reaction in a reflux system and a pressure reactor from pure metal chlorides at about 100 °C. We have also examined the onset of the single domain structure as a function of particle size and how it relates to the observed properties such as coercive fields and magnetization. The reduction in particle size was achieved by milling of the as-prepared samples [9].

5.2 Experimental details

$Sn_{0.2}Fe_xCr_{1.8-x}O_3$ alloys with x ranging from 0.3 to 1.3 were produced by the low temperature synthesis based on the hydrothermal process in a stirred pressure reactor (Figure 4.1) and in a reflux system (Figure 4.2) [111]. All the samples were subjected to thermal annealing in air for 12 hours at 600 °C. Three additional samples were produced by milling the sample of composition $Sn_{0.2}Fe_{1.5}Cr_{0.3}O_3$ for 1 hour, 2 hours and 3 hours respectively. The particle size reductions were performed by mechanical milling using a Retsch MP 400 planetary ball mill. Details for the synthesis methods used to produce different samples have been discussed in chapter 4. All samples were characterized by X-ray diffraction (XRD) using Co$K\alpha$ radiation with wavelength of 1.7903 Å on a Phillips diffractometer (type: PW1710). A Jeol model JEM-1010 transmission electron microscopy (TEM) was used to obtain the morphology of the samples. The ^{57}Fe Mössbauer spectra of the as-prepared samples were recorded at about 300 K in zero field using a conventional constant acceleration Mössbauer spectrometer with a ^{57}Co source sealed in rhodium matrix. A standard natural iron foil was used to calibrate the spectra in terms of the transmitted intensity against velocity of the source. The magnetization measurements at room temperature were performed using a Lakeshore model 735 vibrating sample magnetometer (VSM).

5.3 Results and discussion

5.3.1 X-ray diffraction and transmission electron microscopy measurements

The XRD measurements were scanned in the range $20° \leq 2\theta \leq 80°$ in steps of 0.01°/s. The XRD patterns of the as-prepared samples of $Sn_{0.2}Fe_xCr_{1.8-x}O_3$ with $0.3 \leq x \leq 1.3$ are shown in Figure 5.1 for samples made in a pressure reactor.

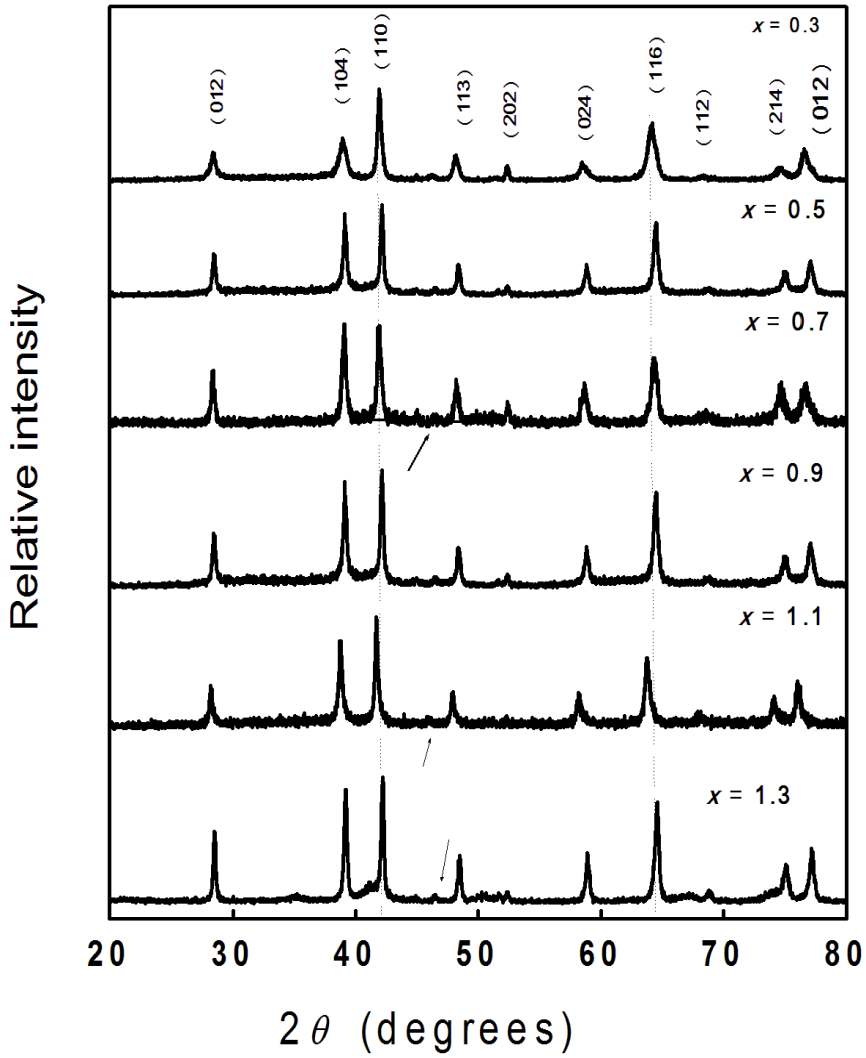

Figure 5.1: XRD patterns recorded for $Sn_{0.2}Fe_xCr_{1.8-x}O_3$ synthesized in a stirred pressure reactor at 100 °C and 120 psi. The arrows show small impurities.

The patterns recorded from the samples were characteristic of the corundum related structure of these materials despite the presence of small impurities peaks. The XRD patterns were different from those recorded from pure $\alpha-Fe_2O_3$ and α-Cr_2O_3 [134]. In particular, the relative intensities of the two peaks characterising the (104) and (110) reflections in the region of 33°-36° in 2θ were reversed. This was strongly suggestive of pronounced preferred orientation in the samples typical of an acicular habit [134], with elongation along $\langle 001 \rangle$ providing an intensity enhancement of the (h k 0) reflections. The results are similar to those recorded from tin-doped α-Fe_2O_3 [66], α-Cr_2O_3 [133] and tin-doped α-$(FeCr)_2O_3$ [77]. It appears that in solid solutions of the type α-$Fe_x(Cr_{1.8-x}O_3)$ tin occupies similar sites as it does in both α-Fe_2O_3 and α-Cr_2O_3 [20]. The refinement of XRD patterns was then performed by a Rietveld analysis according to an identical model to that was previously used to refine the diffraction data of tin-doped α-Fe_2O_3 [133] and α-Cr_2O_3 [20]. The structure of $\alpha-Fe_2O_3$ has Fe^{3+} ions distributed in an ordered fashion in 2/3 of the octahedral sites within a framework of hexagonally close-packed O^{2-} ions. Chains of face sharing octahedra are directed along the c axis, and the Fe^{3+} ions within each chain form pairs as shown in Figure 5.2. It is was shown [133] that for such structures, the data cannot be fitted to a simple model in which Sn^{4+} substitute for Fe^{3+} with charge balance being achieved by an appropriate number of cations vacancies. Such a simple model would introduce face-sharing of SnO_6 and FeO_6 octahedra which would create high cation repulsions. The model that we use involves tin ions substituting on two of the octahedral Fe^{3+} sites in corundum related α-Fe_2O_3. Elimination of Fe^{3+} cations from the octahedra adjacent to the Sn^{4+} creates two additional octahedral sites that do not involve face sharing and which are therefore amenable to occupation by additional Sn^{4+} ions. The structure is formed by defect clusters comprising a chain of three tin ions which all avoid face-sharing repulsions as shown in Figure 5.3. The cluster is electrically neutral since 4 Fe^{3+} ions are replaced by 3 Sn^{4+} ions. In the final stage of the refinements, the

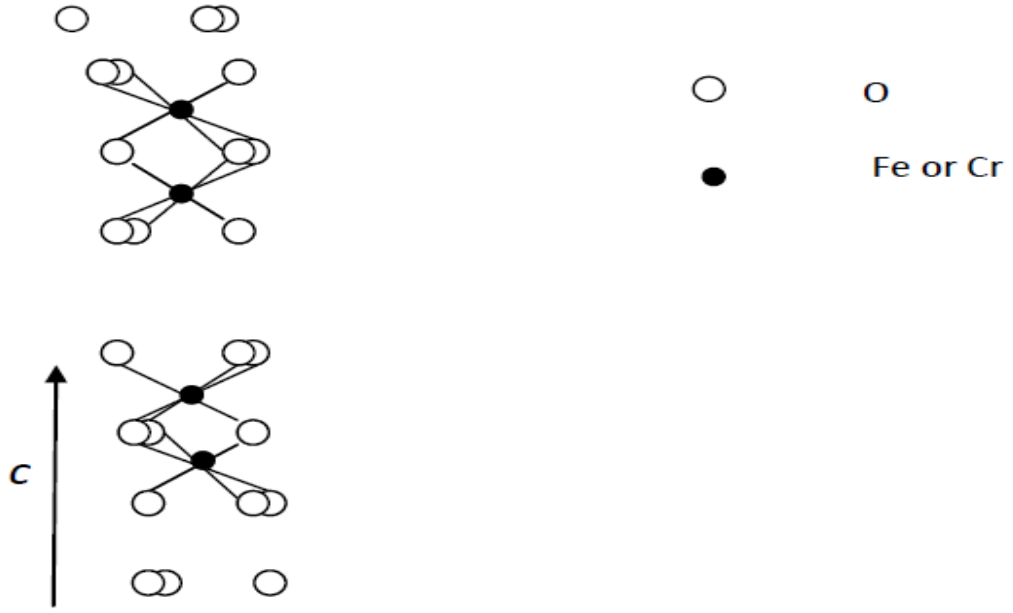

Figure 5.2: Linking of FeO_6 or CrO_6 octahedra along c in α-Fe_2O_3 or α-Cr_2O_3.

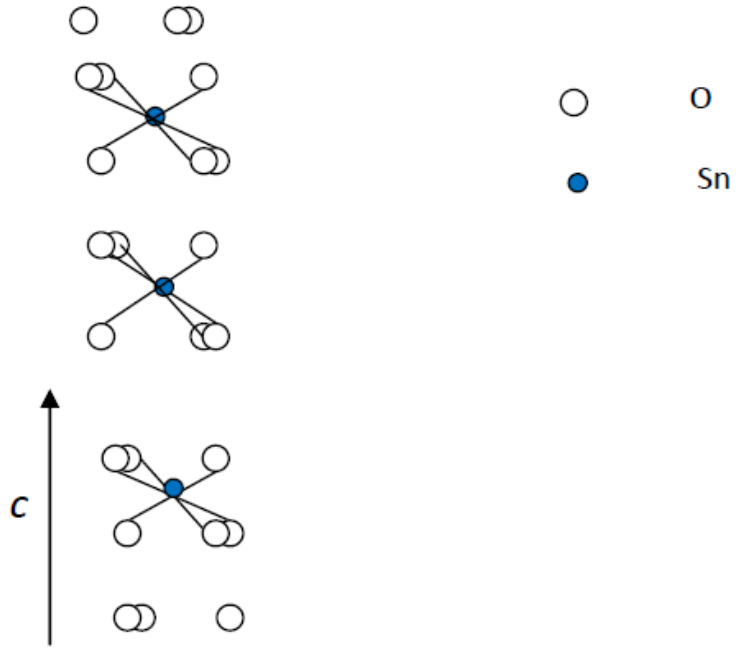

Figure 5.3: Structural model involving the substitution of $4Fe^{3+}$ or $4Cr^{3+}$ ions by 3 Sn^{4+} ions.

cation site occupancies were constrained in accordance with the model. Representative measured data and refinement results for $Sn_{0.2}Fe_{0.3}Cr_{1.5}O_3$ are shown in Figure 5.4, where the black circles indicate the experimental data, red solid line indicates the Rietveld refinement fit by Fullprof analysis software. The green curve at the bottom reveals the difference between the fit and the experimental data. The complete set of final refined parameters are shown in Table 5.1. The structural parameters show

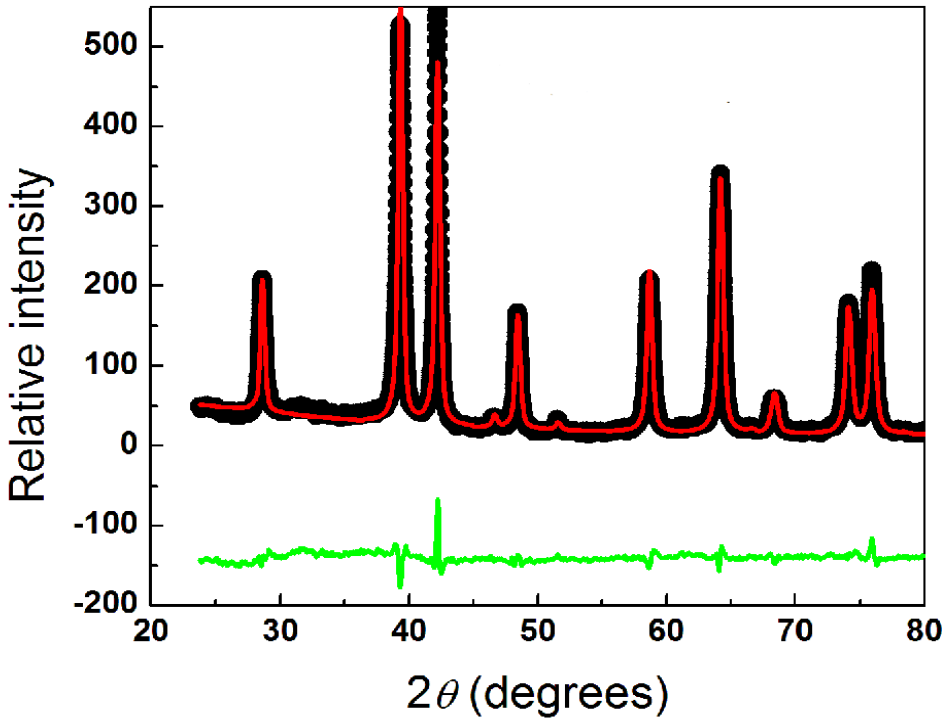

Figure 5.4: Experimental powder X-ray diffractogram of $Sn_{0.2}Fe_{0.3}Cr_{1.5}O_3$ (black symbols), Rietveld refinement fit (solid red line) and difference curve (green line).

little deviation from those of ideal α-Fe_2O_3 and α-Cr_2O_3 [134], which suggests that the defect clusters can be incorporated into the corrundum structure with very little lattice strain.

Figure 5.5 shows the variations of the XRD patterns of $Sn_{0.2}Fe_xCr_{1.8-x}O_3$ for samples made in a reflux system. The main intensity peaks correspond to reflections from (012), (104), (110), (113), (024), (116), (018), (214) and (300) planes which characterize the

Table 5.1: Refined Structural Parameters for samples made in a pressure reactor.

Atom	x/a	y/b	z/c	$U_{iso}\times 100/\mathring{A}^2$	Occupancy
			$Sn_{0.2}Fe_{0.3}Cr_{1.5}O_3$		
Cr1	0.00000	0.00000	0.3463(2)	0.500(0)	9.016(2)
Fe	0.00000	0.00000	0.3463(2)	0.500(0)	1.696(2)
Sn1	0.00000	0.00000	0.3463(2)	0.500(0)	0.447(3)
Sn2	0.00000	0.00000	0.00000	0.000(0)	0.500(0)
O1	0.3217(1)	0.00000	0.2500(0)	0.500(0)	18.000(0)
R_{wp} (%)	14.4		R_{exp} (%)	9.5	
			$Sn_{0.2}Fe_{0.5}Cr_{1.3}O_3$		
Cr1	0.00000	0.00000	0.35173(2)	0.500(0)	8.594(2)
Fe	0.00000	0.00000	0.35173(2)	0.500(0)	2.118(2)
Sn1	0.00000	0.00000	0.35173(2)	0.500(0)	1.290(3)
Sn2	0.00000	0.00000	0.00000	0.000(0)	0.500(0)
O1	0.3217(1)	0.00000	0.2500(0)	0.500(0)	18.000(0)
R_{wp} (%)	12.9		R_{exp} (%)	9.3	
			$Sn_{0.2}Fe_{0.7}Cr_{1.1}O_3$		
Cr1	0.00000	0.00000	0.34690(0)	0.500(0)	9.055(0)
Fe	0.00000	0	0.34690(0)	0.500(0)	2.415(0)
Sn1	0.00000	0.00000	0.34690(0)	0.500(0)	0.270(0)
Sn2	0.00000	0.00000	0.00000	0.000(0)	0.500(0)
O1	0.3217(1)	0.00000	0.250(0)	0.500(0)	18.000(2)
R_{wp} (%)	14.4		R_{exp} (%)	10.8	
			$Sn_{0.2}Fe_{0.9}Cr_{0.9}O_3$		
Cr1	0.00000	0.00000	0.34690(0)	0.500(0)	10.260(0)
Fe	0.00000	0.00000	0.34690(0)	0.500(0)	1.207(0)
Sn1	0.00000	0.00000	0.34690(0)	0.500(0)	0.270(0)
Sn2	0.00000	0.00000	0	0.000(0)	0.500(0)
O1	0.30800(0)	0.00000	0.2500(0)	0.500(0)	18.000(0)
R_{wp} (%)	13.4		R_{exp} (%)	10.5	
			$Sn_{0.2}Fe_{1.1}Cr_{0.7}O_3$		
Cr1	0.00000	0.00000	0.34689(0)	0.500(0)	9.658(0)
Fe	0.00000	0.00000	0.34689(0)	0.500(0)	1.810(0)
Sn1	0.00000	0.00000	0.34689(0)	0.500(0)	0.269(0)
Sn2	0.00000	0.00000	0.00000	0.000(0)	0.500(0)
O1	0.3217(1)	0.00000	0.250(0)	0.500(0)	18.000(0)
R_{wp} (%)	12.4		R_{exp} (%)	7.5	
			$Sn_{0.2}Fe_{1.3}Cr_{0.5}O_3$		
Cr1	0.00000	0.00000	0.35392(2)	0.284(0)	9.178(0)
Fe	0.00000	0.00000	0.35392(2)	0.284(0)	2.051(0)
Sn1	0.00000	0.00000	0.35392(2)	0.284(0)	0.384(0)
Sn2	0.00000	0.00000	0.00000	0.000(0)	0.500(2)
O1	0.30779(1)	0.00000	0.250(0)	0.117(0)	18.000(0)
R_{wp} (%)	14.5		R_{exp} (%)	9.6	

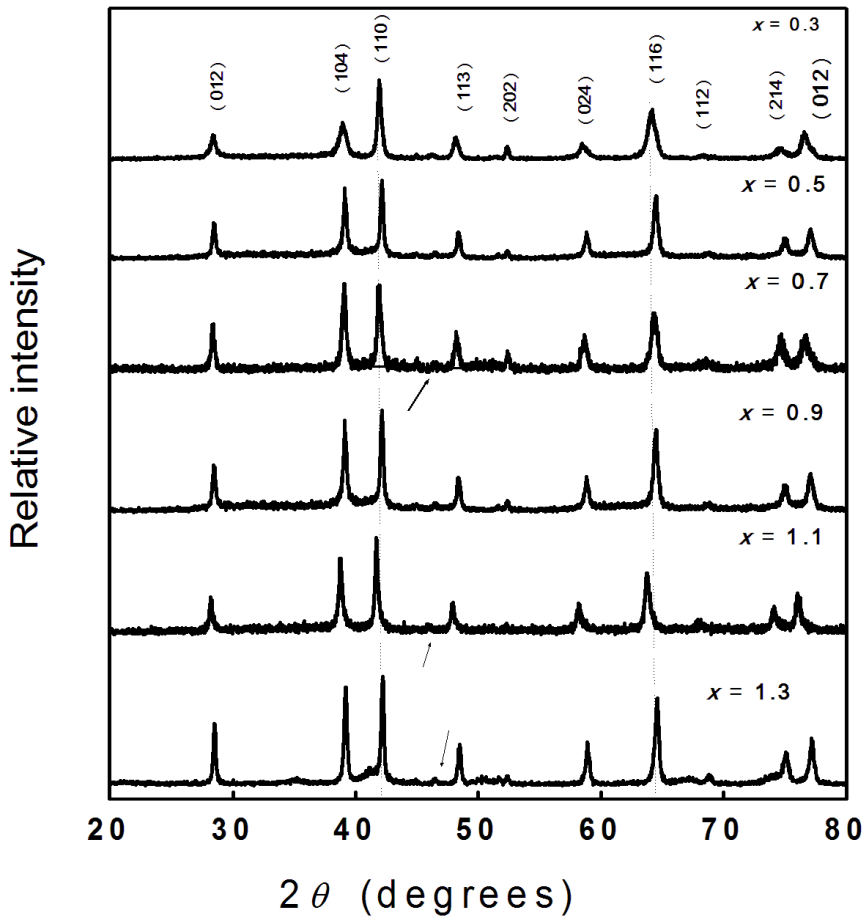

Figure 5.5: XRD patterns recorded for $Sn_{0.2}Fe_xCr_{1.8-x}O_3$ synthesized in a reflux system at 100 °C .

corundum structure as indicated in Figures 5.1 and 5.5. The measured data was refined using Fullprof software against the theoretical parameters from the model used previously [134]. The results indicate very small changes in unit cell size between the samples made in a reflux glass condenser and those made in a pressure reactor. Direct measurement of the particle size and powder morphology for the as-prepared samples were also performed by transmission electron microscopy (TEM). The TEM images in Figure 5.6 show that the samples consist of small nanosized particles. The calculated D_{XRD} and measured D_{TEM} values appear to be in good agreement. The lattice parameters, the average particle diameters as calculated from XRD data (D_{XRD}) and observed by TEM measurements (D_{TEM}) are shown in Table 5.2.

Table 5.2: Particle size (D_{XRD}), (D_{TEM}) and lattice parameters for as-prepared $Sn_{0.2}Fe_xCr_{1.8-x}O_3$ samples.

x	Reflux					Pressure reactor				
	$a = b$ (Å) $\pm 10^{-3}$	c (Å) $\pm 10^{-3}$	V ($Å^3$) $\pm 10^{-3}$	D_{XRD} (nm) ± 0.4	D_{TEM} (nm) ± 2	$a = b$ (Å) $\pm 10^{-3}$	c (Å) $\pm 10^{-3}$	V ($Å^3$) $\pm 10^{-3}$	D_{XRD} (nm) ± 0.4	D_{TEM} (nm) ± 2
0.1	4.961	13.602	290.30	29.34	28	4.971	13.617	289.29	28.41	28
0.3	4.990	13.696	289.77	27.06	26	4.954	13.817	289.22	26.52	28
0.5	4.985	13.643	294.35	35.13	34	4.985	13.643	294.02	34.83	34
0.7	4.986	13.635	289.34	26.31	25	4.953	13.630	289.24	25.32	25
0.9	5.024	13.778	292.34	37.58	31	4.981	13.631	291.78	31.5	32
1.1	4.997	13.640	290.23	31.25	30	4.953	13.635	289.87	30.9	25
1.3	4.986	13.638	288.54	28.75	28	4.953	13.637	287.89	28.5	25

The errors in D_{XRD} are calculated using the formula

$$\frac{\delta D_{XRD}}{D_{XRD}} = \sqrt{\left(\frac{\Delta K}{K}\right)^2 + \left(\frac{\Delta \lambda}{\lambda}\right)^2 + \left(\frac{\Delta \beta}{\beta}\right)^2 + \left(\frac{\Delta \theta}{\theta}\right)^2} \tag{5.3.1}$$

based on the Scherrer formula. The shape of the crystallite are not uniform. It is realistic to assume $\Delta K \simeq \pm 0.1$. This makes a significant contribution to the calculated error in Table 5.2. The volume of the samples do not significantly change despite the incorporation of Fe^{3+} with smaller ionic radii into the sites of Cr^{3+} with larger ionic radii. The general trend of D for the different samples shows similar patterns for the samples made by reflux and in a pressure reactor. The samples made in a pressure reactor appear to have a slightly reduced particle size than those made in a glass reflux system. Considering the uncertainties, except for the sample $x = 0.9$, the D-values are similar and there is no difference between samples prepared in reflux and in

pressure reactor. This argument is also supported by the TEM data, which show similar values between the samples. The D-values obtained from TEM also agree with those estimated from XRD data, except for samples with x =0.9 and 1.1, but with values in acceptable range discrepancy. T. Nguyen *et al.* [135] have studied the nucleation and growth of nanoparticles. This theory gives a basic outline of how to control particle formation within solution by elucidating the key controllable parameters: reaction temperature, supersaturation, time and the surface energy which can be controlled indirectly through the choice of surfactants. Each material will nucleate and grow depending on its reaction conditions and even a small change in condition, such as pH, can lead to a completely different mechanisms [136].

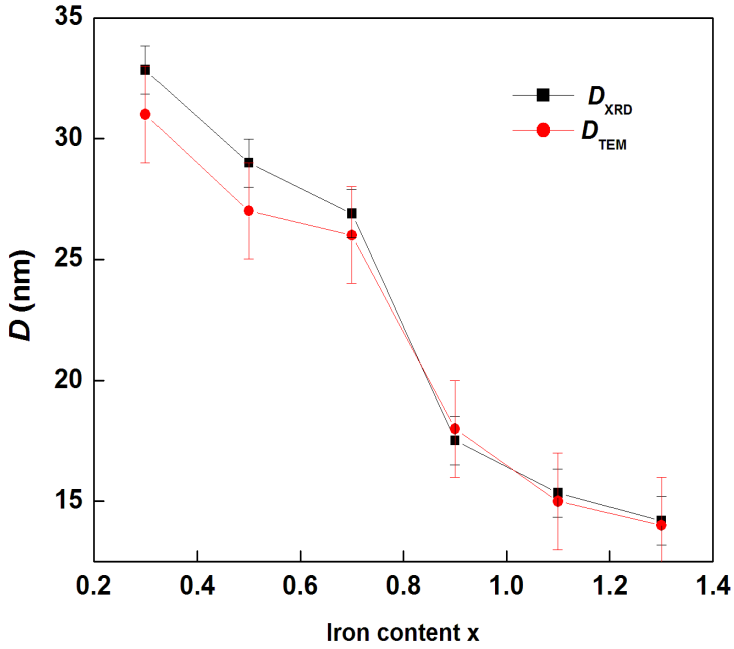

Figure 5.6: Variation of particle size with iron content for the as-prepared samples of $Sn_{0.2}Fe_xCr_{1.8-x}O_3$.

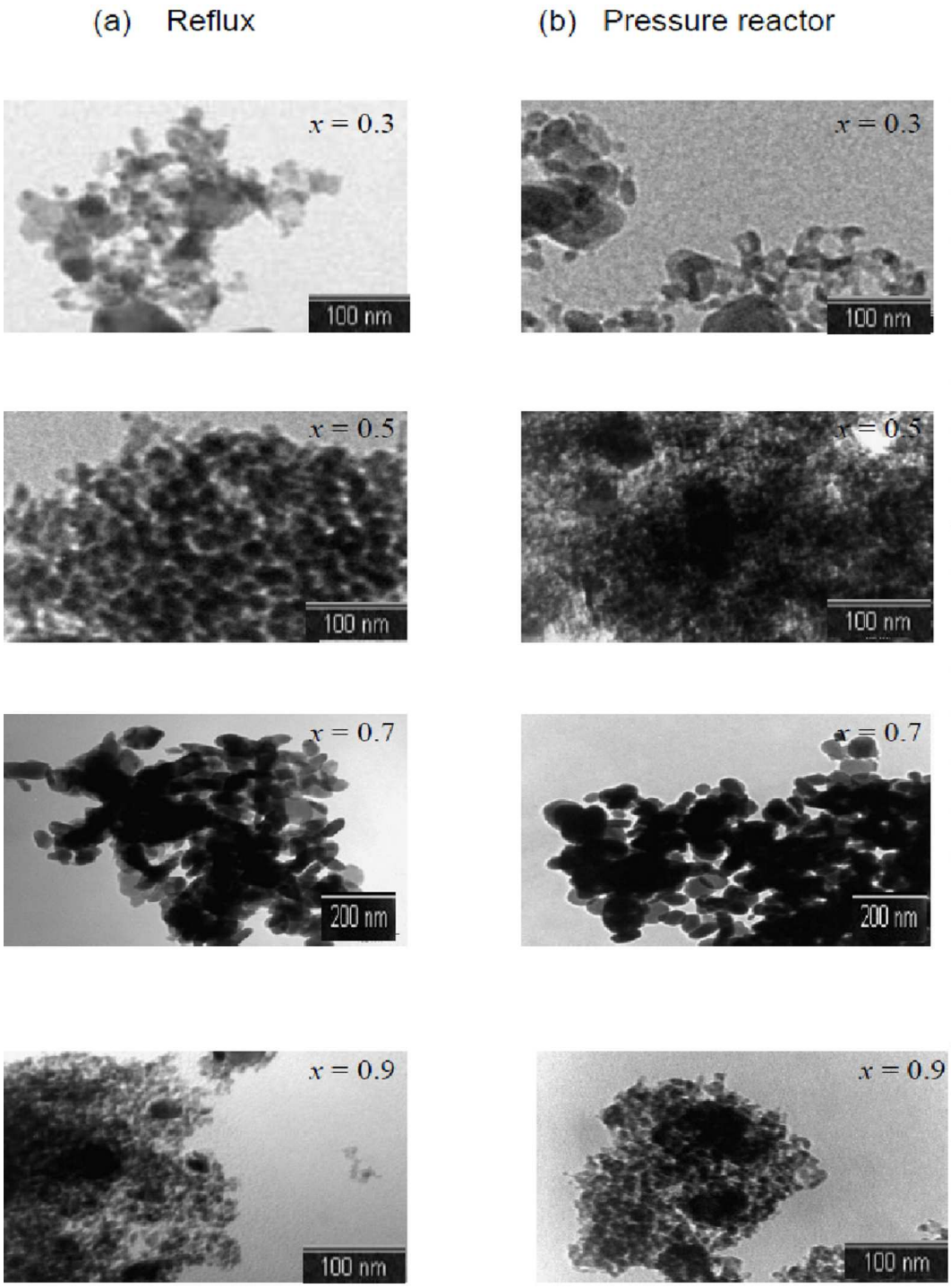

Figure 5.7: TEM micrographs for the $Sn_{0.2}Fe_xCr_{1.8-x}O_3$ samples prepared (a) in an open reflux vessel and (b) in pressure reactor.

5.3.2 Mössbauer measurements

The ^{57}Fe Mössbauer spectra recorded from $Sn_{0.2}Fe_xCr_{1.8-x}O_3$ samples at 300 K are shown in Figures 5.8 (reflux) and 5.9 (pressure reactor). It can been seen that the spectra of the samples with $x = 0.3$ and $x = 0.5$ are paramagnetic doublets. The spectra for $x = 0.7$ and $x = 0.9$ show paramagnetic component with a non-zero electric field gradient around ^{57}Fe isotopes. For $x \geq 1.1$ sextets are observed. Each Mössbauer spectrum has been fitted with two magnetic components in the form of two sextets, one sextet and one doublet or two doublets. The sextet with the higher hyperfine field is attributed to Fe^{3+} ions without Cr^{3+} or Sn^{4+} in their neigborhood lattice sites. The second sextet with lower hyperfine field is due to Fe^{3+} ions with Cr^{3+} and Sn^{4+} neighbors. This interpretation of hyperfine fields is similar to the work of Berry *et al.* [133] in Sn and Ti doped α-Fe_2O_3 samples. The doublets are observed in samples that have higher Cr content. This reflects the collapse of magnetic interaction with increase Cr content associated with more negative exchange interactions leading to doublets. All the components in the spectra recorded at 300 K were characterised by nearly constant chemical isomer shifts of about 0.35(5) mm/s confirming that the accomodation of tin into the corrundum-related structure did not induce a change in the Fe^{+3} oxidation state of iron [20]. Insignificant change in isomer shifts indicates that the s-electron density is not much affected by substitution of Cr by Fe atoms. The values of the isomer shifts and the hyperfine fields recorded in Table 5.3 are comparable to those reported for similar compounds [106]. The variation of the component with maximum hyperfine magnetic field with increasing iron content x in spectra recorded at 300 K is shown in Figure 5.10. It appears that the hyperfine field increases as the iron content x increases. The samples produced by reflux show higher magnetic hyperfine fields than the samples made in a pressure reactor. This is due to the fact that the samples made by reflux have particle sizes that are slightly higher at the

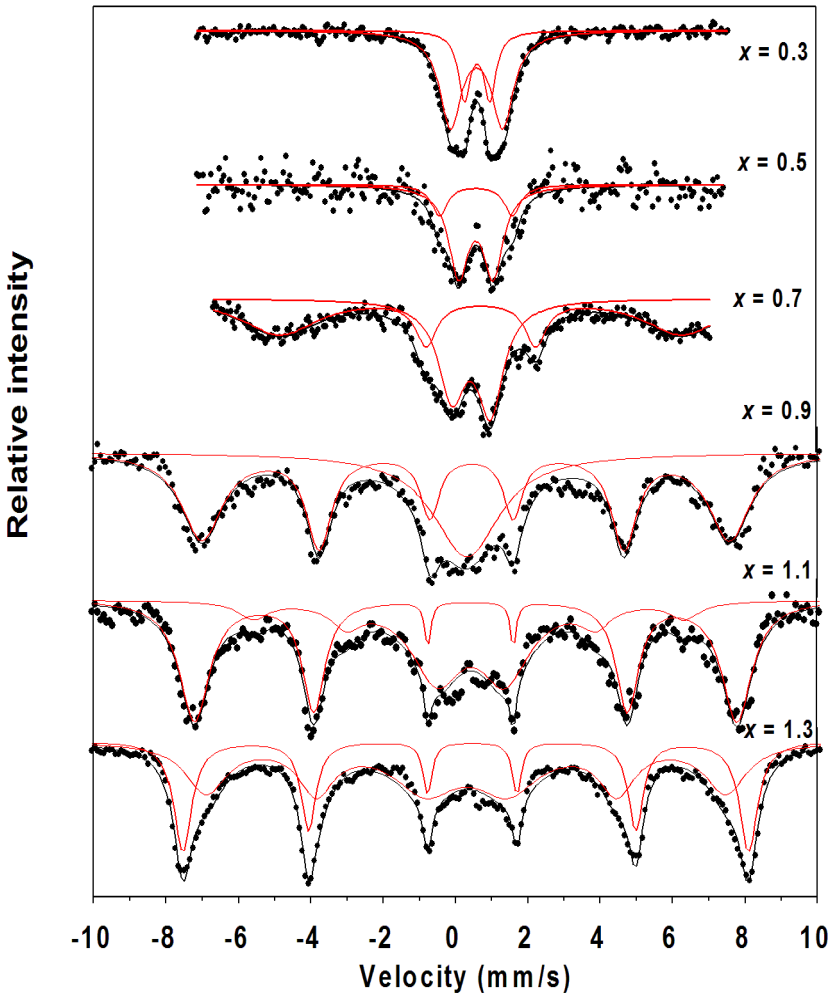

Figure 5.8: Room temperature ^{57}Fe Mössbauer spectra recorded for $Sn_{0.2}Fe_xCr_{1.8-x}O_3$ samples produced via reflux. The solid lines are the LSQ fits.

same composition than those of samples made in a pressure reactor. This decreasing tendency of the magnetic hyperfine fields at small particle sizes may be due to both the surface effect and the size effect. As the particle size decreases to nanoscale, the volume of the surface atoms is an appreciable fraction of that in the total volume, and both the small-size effect and the surface effect perturb the structure and the properties of the nanoparticles. In ferromagnetic and ferrimagnetic oxides, magnetic coupling is very sensitive to the atomic environment. The smaller the particle size the higher the fraction of surface atoms and the lower the contribution to the total magnetic moment [137].

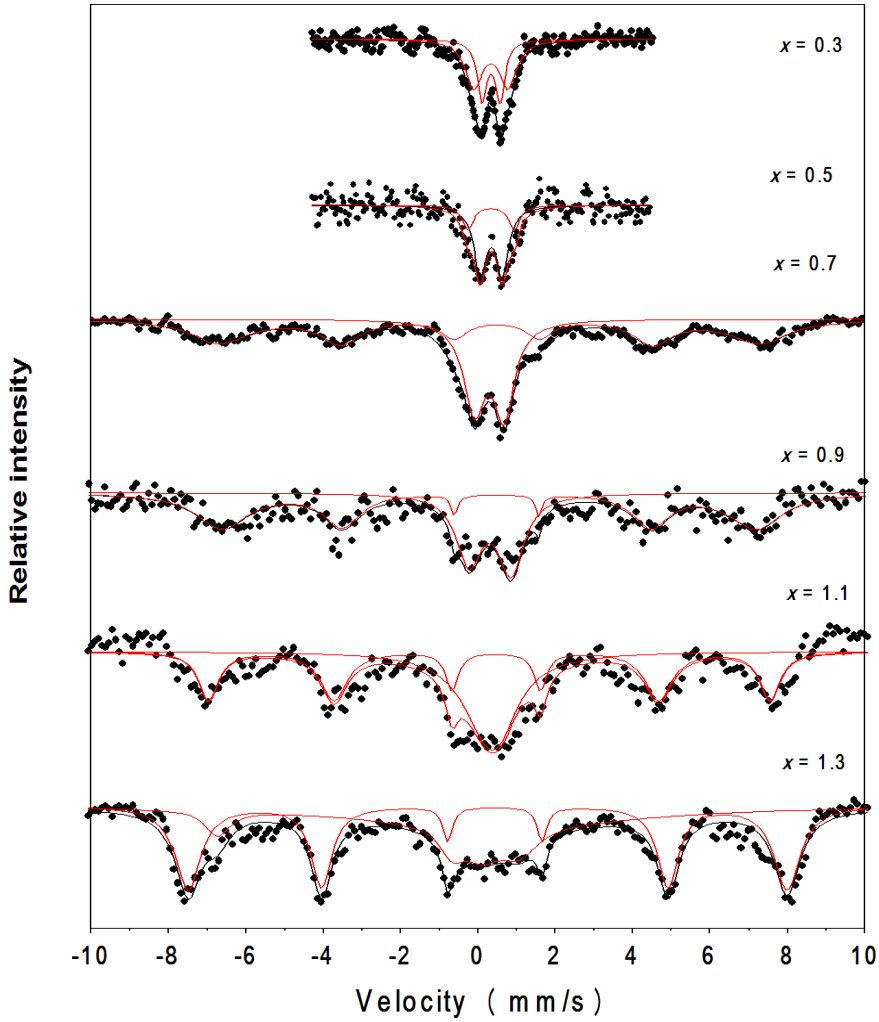

Figure 5.9: Room temperature ^{57}Fe Mössbauer spectra recorded for $Sn_{0.2}Fe_xCr_{1.8-x}O_3$ samples produced via the pressure reactor. The solid lines are the LSQ fits.

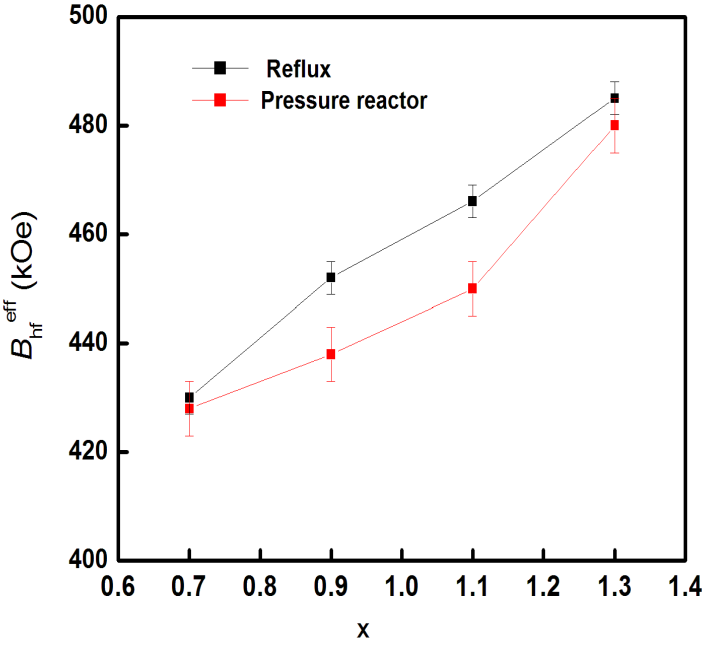

Figure 5.10: The variation of the component with maximum hyperfine magnetic field with increasing iron content x for $Sn_{0.2}Fe_xCr_{1.8-x}O_3$.

Table 5.3: Hyperfine parameters from Mössbauer spectra recorded at room temperature for the as-prepared samples of $Sn_{0.2}Fe_xCr_{1.8-x}O_3$.

T = 300 K	doublet 1			doublet 2			sextet 1				sextet 2			
	δ	Δ	f	δ	Δ	f	δ	2ε	H	f	δ	2ε	H	f
Sample	mm/s	mm/s	%	mm/s	mm/s	%	mm/s	mm/s	kOe	%	mm/s	mm/s	kOe	%
x	± 0.01	± 0.02		± 0.01	± 0.02		± 0.01	± 0.02	± 3		± 0.01	± 0.02	± 3	
Reflux														
0.3	0.37	0.42	28	0.36	0.87	72								
0.5	0.34	1.21	22	0.34	0.57	78								
0.7	0.34	0.9	32				0.38	-0.10	404	68				
0.9	0.32	0.01	33				0.37	-0.08	452	67				
1.1							0.36	-0.11	465	56	0.35	-0.031	390	44
1.3							0.37	-0.09	485	64	0.29	-0.09	445	36
Pressure reactor														
0.3	0.33	0.34	68	0.37	0.54	32								
0.5	0.35	0.34	50	0.36	0.34	50								
0.7	0.29	0.76	41				0.39	-0.09	428	59				
0.9	0.31	1.09	37				0.38	-0.10	438	63				
1.1	0.38	0.38	47				0.37	-0.08	450	53				
1.3							0.35	-0.08	421	50	0.35	-0.12	480	50

5.3.3 Magnetization measurements

The isothermal magnetization measurements presented here were performed at room temperature using a Lakeshore vibrating sample magnetometer [124]. Hysteresis loops of the samples in powder forms were obtained in an external applied field up to 14 kOe. The magnetization measurements at room temperature obtained from $Sn_{0.2}Fe_xCr_{1.8-x}O_3$ samples made in a reflux and in a pressure reactor are presented in Figures 5.11 and 5.12 respectively. The results show that the hysteresis loops obtained from the two synthesis methods are similar. The hysteresis loops are symmetric and not shifted with respect to the origin. It worth noting that the hysteresis loops for samples with $x \leqslant 0.7$ appear to consist of a paramagnetic phase where the $M - H$ plots are linear and have a magnetically ordered phase at low fields associated with hysteresis whilst for $x > 0.7$, the magnetization increases significantly. The samples exhibit nearly zero remanence and zero coercivity suggesting a superparamagnetic behavior for nanocrystalline iron oxides [20]. The magnetization does not appear to saturate even at the maximum applied field. The slow approach to saturation can be explained on the basis of the disordered spin configuration at the surface of the magnetic nanooxides [20]. The samples with lower iron concentration have similar magnetic properties as α-Cr_2O_3 [71] whilst those with higher iron concentration display properties of α-Fe_2O_3 [22]. The magnetic properties such as coercivity H_C, saturation magnetization M_S and remanance M_R were estimated from the magnetic hysteresis loops. The coercive field is calculated as

$$H_C = |\frac{H_1 + H_2}{2}| \tag{5.3.2}$$

where H_1 and H_2 are fields at the left and right side of the shifted magnetization curves respectively. The remanent magnetization is also obtained from the vertical magnetization shifts. The uncertainties have been found by standard deviation using Origin software. The coercive fields are significantly reduced with increase in Fe content

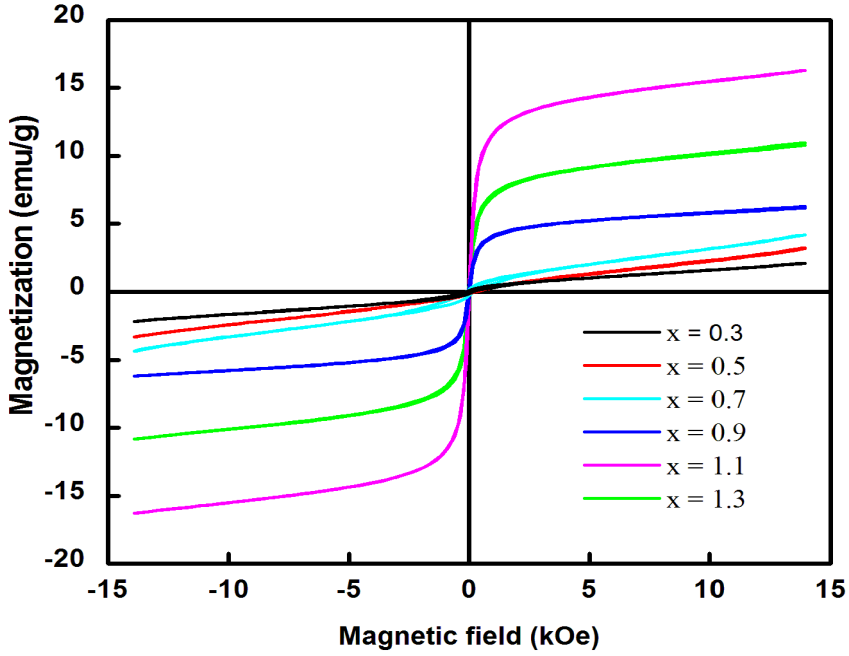

Figure 5.11: Hysteresis loops measured at room temperature for $Sn_{0.2}Fe_xCr_{1.8-x}O_3$ prepared in a reflux.

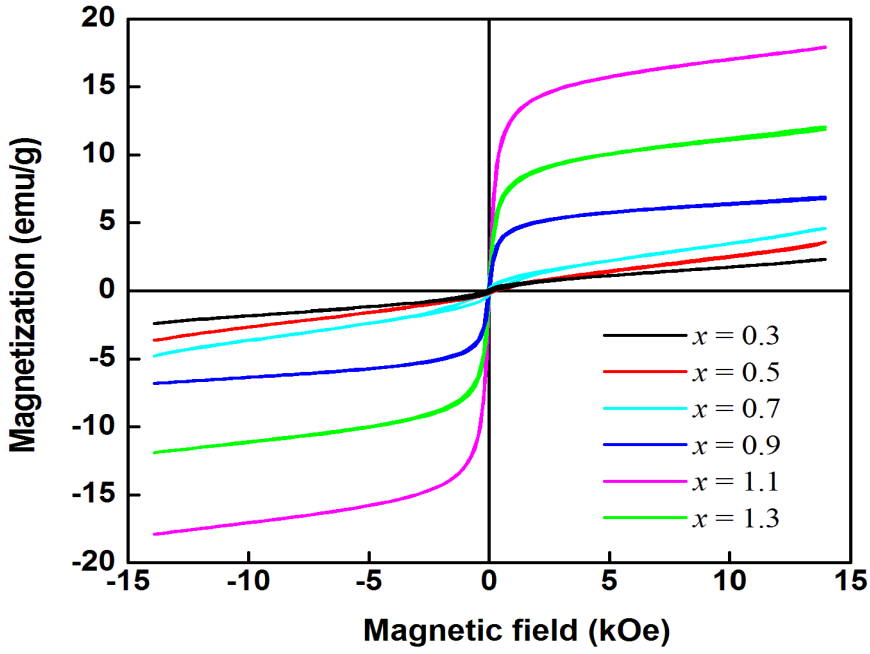

Figure 5.12: Hysteresis loops measured at room temperature for $Sn_{0.2}Fe_xCr_{1.8-x}O_3$ prepared in a pressure reactor.

while the saturation magnetization increases. The saturation magnetization was taken as the magnetization at the highest applied field. This is a reasonable estimate if we are interested in elucidating the trends in the properties with increasing iron concentration. The coercive field is a measure of the magnetization reversal processes under the action of an applied field. It depends on the domain structure, particle sizes and crystalline anisotropy. The coercive field of $Sn_{0.2}Fe_xCr_{1.8-x}O_3$ nanoparticles have been studied as a function of iron content. The substitution by Fe atoms leads to a reduction in H_C. In Figures 5.13-5.15 we have plotted the coercive fields, remanent magnetizations and saturation magnetizations as a function of iron content. The data obtained for magnetization measurements are presented in Table 5.3. The results show that the hysteresis disappears as the iron content increases. The magnetization data for $x > 0.7$ display a nearly zero coercive field which could be related to small particles in superparamagnetic state while Mössbauer data show no superparamagnetic state for most of Fe atoms in the prepared materials. This discrepancy may be due to the different time window of these experimental techniques. The saturation magnetization M_S values measured for the samples gradually increases with Fe^{3+} substitution. This may be due to the fact that Cr^{3+} ions (magnetic moment 3 μB) are replaced by stronger magnetic Fe^{3+} ions (magnetic moment 5 μB). The ratio $M_R/M_S = S$ is referred to as the squareness of a hysteresis loop [127] where M_R is the remanent magnetization. It is derived to determine whether the intergrain exchange exists or not [138]. Stoner and Wohlfarth have reported $S = 0.5$ for randomly oriented non-interacting particles, while $S < 0.5$, particles interact by magnetostatic interaction [138]. In this series of alloys, all samples S values are less than 0.5 indicating that particles interact by magnetostatic interactions. We have further investigated the effect of the reduction of particle sizes on magnetization by mechanical milling on a $Sn_{0.2}Fe_{1.3}Cr_{0.5}O_3$ sample. The hysteresis curves are shown in Figure 5.16 and the magnified view in Figure 5.17. The various parameters deduced from the hysteresis loops are given in Table 5.4. A significant drop

in magnetization and an increase in coercive field are observed on reducing grain sizes from about 28 nm to 24 nm (after 2 hours of milling). The reduction in magnetization is attributed to weakening of magnetic coupling between moments. The reduction in magnetization can also be explained by structural distortions in the surface of the powders compared to that of bulk compounds [139], [140]. This compares well with the evolution of the superparamagnetic phase in the Mössbauer spectra with decreasing grain size. A slight reduction in coercive field is also observed when the particle size is further reduced to 17 nm (after 3 hours of milling). The coercive field appears to achieve a maximum value of about 207 Oe at a critical sample particle size of about 22.8 nm as shown in Figure 5.18. This trend is expected to be closely related to the change in magnetic hardness of the samples [135]. Similar behavior has been

Table 5.4: Coercive fields (H_C), saturation magnetizations (M_S), remanent magnetizations (M_R)and ratio M_R/M_S for $Sn_{0.2}Fe_xCr_{1.8-x}O_3$ samples.

Sample x	H_C Oe $\pm$ 4	M_R emu/g $\pm$0.1	M_S emu/g $\pm$0.1	M_R/M_S
Reflux				
0.3	278	0.1	2.0	0.02
0.5	220	0.1	2.1	0.03
0.7	210	0.2	4.2	0.03
0.9	33	0.5	10.3	0.05
1.1	22	0.8	13.2	0.06
1.3	18	1.1	16.2	0.07
Pressure reactor				
0.3	287	0.1	2.3	0.04
0.5	238	0.1	3.4	0.03
0.7	228	0.2	4.6	0.04
0.9	43	0.4	6.9	0.05
1.1	31	0.9	11.9	0.07
1.3	28	1.1	13.8	0.08

observed elsewhere [19]. This decrease at larger sizes can be explained on the basis of a crossover effect from single-domain to mutli-domain behavior at a critical particle size [141]. After about 3 hours of milling no significant change in the particle size occurs

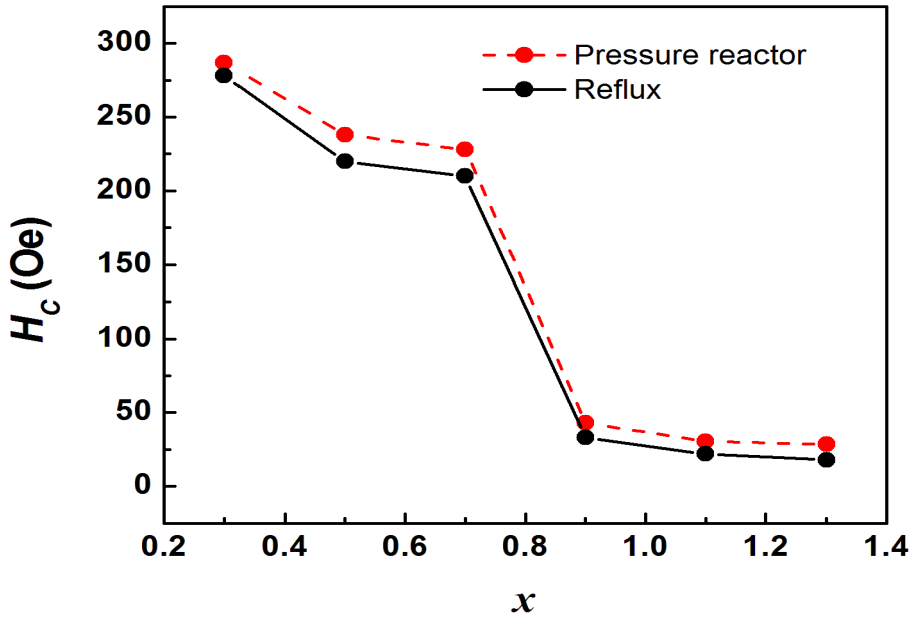

Figure 5.13: Coercive field H_C versus iron concentration for $Sn_{0.2}Fe_xCr_{1.8-x}O_3$ samples.

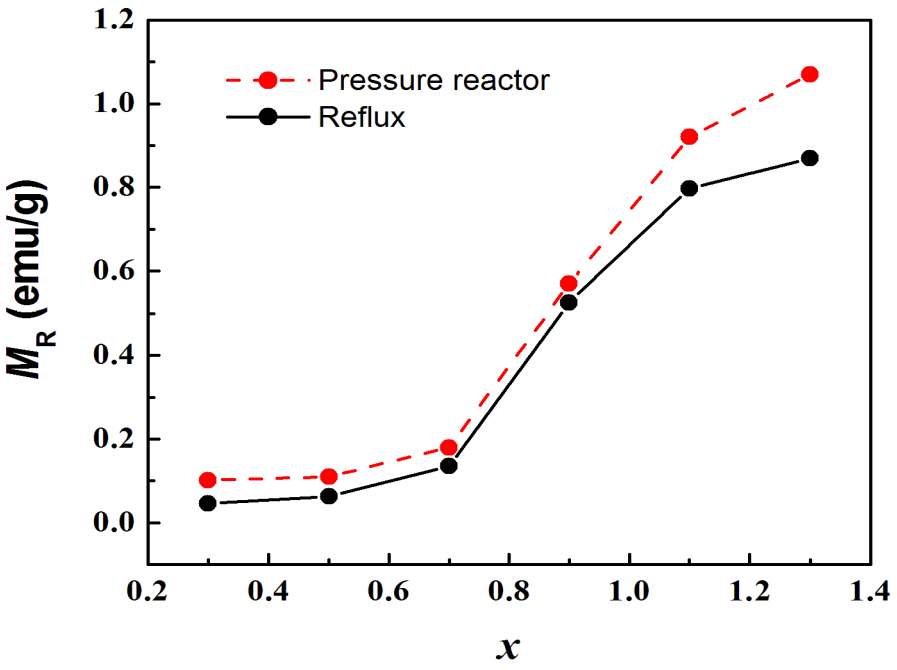

Figure 5.14: Remanent magnetization M_R versus iron concentration (x) for the as-prepared $Sn_{0.2}Fe_xCr_{1.8-x}O_3$ samples.

with further grinding. For single-domain particles the coercive field can be expected

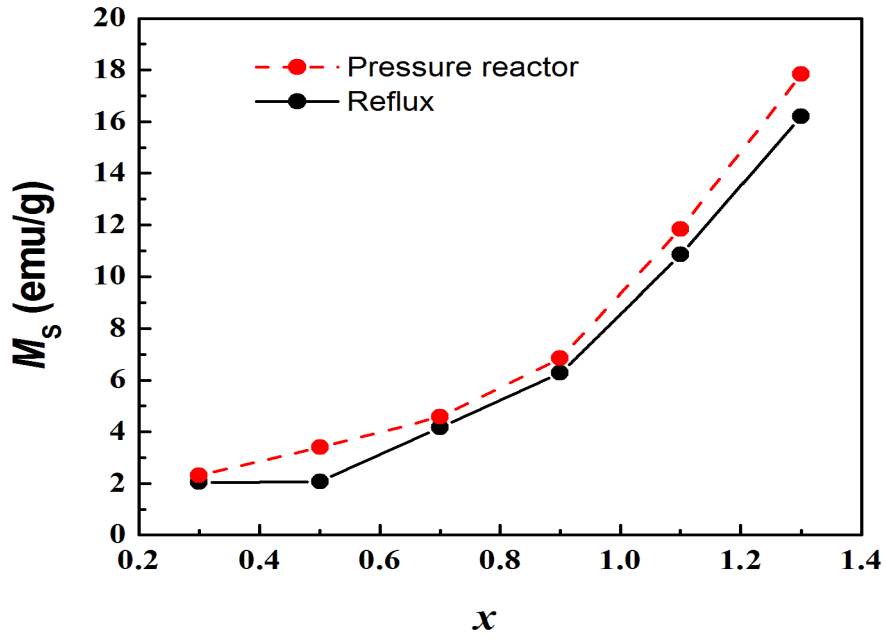

Figure 5.15: Saturation magnetization M_S versus iron concentration (x) for the as-prepared $Sn_{0.2}Fe_xCr_{1.8-x}O_3$ samples.

to increase with increase in particle size D according to the relation [141]

$$H_C = a_m + b_m/D \tag{5.3.3}$$

where a_m and b_m are constants. We have plotted H_C versus $1/D$ in Figure 5.19 to test the validity of Eq. (5.3.3) and determined the constants a_m and b_m. A good fit to the data (correlation coefficient of 0.9396) has been observed. We obtained the values of a_m and b_m for the $Sn_{0.2}Fe_{1.3}Cr_{0.5}O_3$ oxide to be -1.1 ± 0.45 kOe and 32.5 ± 11.85 nm kOe, respectively. The value of b_m might be related to the magnetic coupling between the moments [19]. For multi-domain particles, H_C is expected to decrease with further increase in particle size as [141]

$$H_C = a_s - b_s/D^2. \tag{5.3.4}$$

A graph of H_C versus $1/D^2$ for the $Sn_{0.2}Fe_{1.3}Cr_{0.5}O_3$ oxide is shown in Figure 5.20. This gives the constant a_s and b_s to be 0.48 kOe and - 109.29 $(nm)^2$ kOe (with a correlation coefficient of 0.98057). The coercive field is closely related to processes that limit the

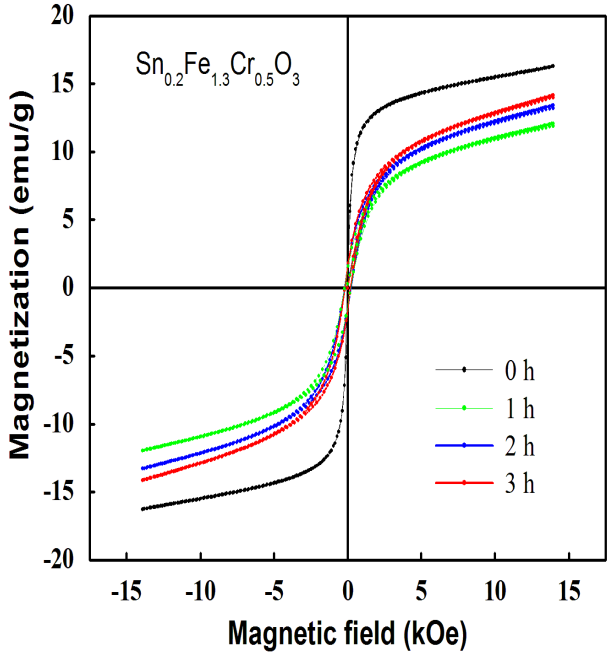

Figure 5.16: Room temperature hysteresis loops for the milled $Sn_{0.2}Fe_{1.3}Cr_{0.5}O_3$.

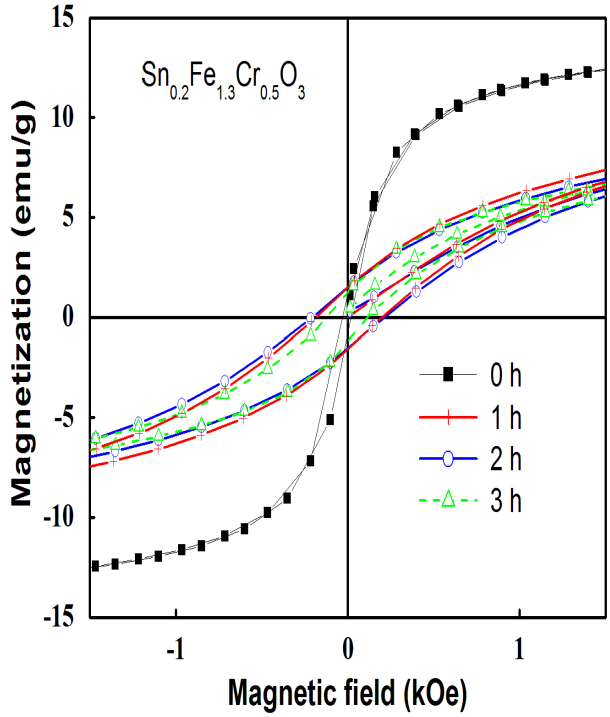

Figure 5.17: Magnified view of hysteresis loops measured at low fields for milled $Sn_{0.2}Fe_{1.3}Cr_{0.5}O_3$.

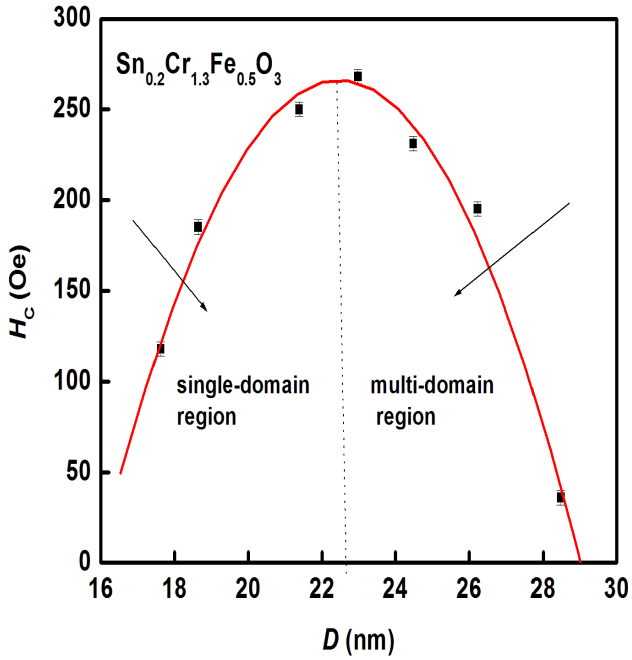

Figure 5.18: Coercive field H_C versus particle size D for $Sn_{0.2}Fe_{1.3}Cr_{0.5}O_3$. The solid line is the LSQ fit.

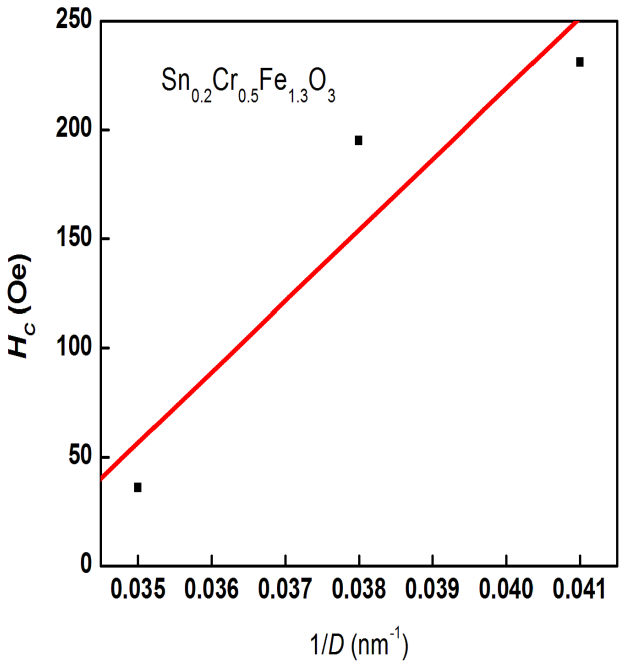

Figure 5.19: Variation of coercive fields for $Sn_{0.2}Fe_{1.3}Cr_{0.5}O_3$ with $1/D$ for $D<$ 23 nm below transition point for ball milled samples. The solid line is the LSQ fit.

motion of domain walls in a material. In the present system of compounds we assume that this arises due to an increased number of grain boundaries with milling [130]. The milling process increases the number of multidomain particles. A nonlinear variation in coercivity and anisotropy constant can be explained on the basis of particle size as with the reduction of particle size, the surface to volume ratio increases and surface effects may induce a spin disorder in surface layer which results in enhanced anisotropy [142, 143].

Table 5.5: Effect of the milling time on the nanoparticles properties.

	$Sn_{0.2}Fe_{1.3}Cr_{0.5}O_3$	
Milling time (min)	H_C Oe $\pm$ 4	D (nm) $\pm$0.02
0	36	28.48
60	195	26.23
120	231	24.48
130	268	22.98
150	250	21.38
170	185	18.64
180	118	17.62

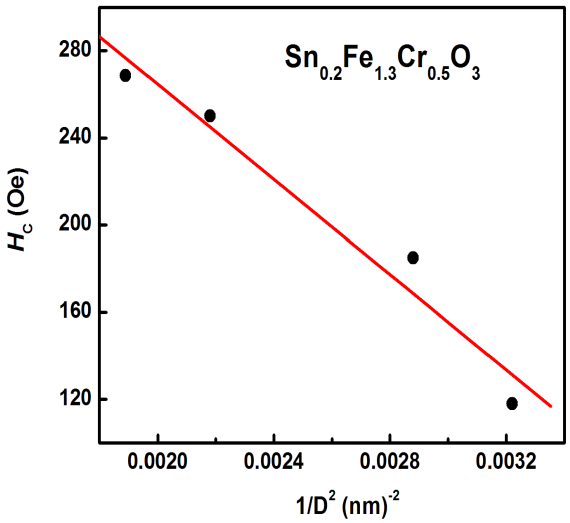

Figure 5.20: Variation of coercive fields for $Sn_{0.2}Fe_{1.3}Cr_{0.5}O_3$ with $1/D^2$ for $D>$ 23 nm. The solid line is the LSQ fit.

5.3.4 Conclusion

Nanoparticles of $Sn_{0.2}Fe_xCr_{1.8-x}O_3$ oxides with single phase corundum structure were synthesized directly by the hydrothermal method. There were no significant difference in the particle sizes of the samples made in reflux and in a pressure reactor as determined by XRD and TEM analysis. However, the samples prepared using a pressure reactor appear to be have particle sizes that are slightly smaller. The composition variations also appear to follow similar trends. Evidence of successful Sn incorporation into the corundum structure is obtained [20]. The milled sample of $Sn_{0.2}Fe_{1.3}Cr_{0.5}O_3$ shows reduced magnetization with reduction in grain size and an associated increase in coercive field after milling for 2 hours. The coercive fields have been found to vary with particle size according to Equations 5.3.3 and 5.3.4 corresponding to single-domain and muti-domain behavior respectively.

Chapter 6

Structure and magnetic properties of $Mg_{0.2}Fe_xCr_{1.8-x}O_3$ nano oxides

6.1 Introduction

In this chapter we present the structure and magnetic properties of $Mg_{0.2}Fe_xCr_{1.8-x}O_3$ nanosized alloys with $0.3 \leq x \leq 0.9$. The samples were synthesized at low reaction temperature of about 100 °C by using the hydrothermal method in a pressure reactor. We managed to produce samples with particle sizes in the range between 32.8 and 55.6 nm. The structures and magnetic properties of the synthesized samples were investigated on the as-prepared samples annealed at 600 °C and on samples annealed at 700 °C. The evolutions of the properties as a function of composition were investigated by XRD, TEM, Mössbauer spectroscopy, magnetization and susceptibility measurements.

6.2 Experimental details

High-purity metal chlorides were used as starting materials to make 0.1 molar (M) solutions for the hydrothermal process. The synthesis procedures is similar to what we have presented before [20, 21]. Excess aqueous ammonia was slowly added to the chloride mixture until full precipitation. The precipitate was boiled in deionised water in a pressure reactor for 3 hours. The products were then filtered and washed

with deionized water several times until no chloride ions were detected by addition of drops of silver nitrate standard solution. The clean products were finally washed with ethanol and then dried under an infrared 250 W lamp. The resulting homogeneous powders were heated in air at 600 °C for 12 hours. The X-ray diffraction (XRD) patterns of the samples were obtained by using CoKα radiation (λ = 1.7903 Å) on a Philips diffractometer (type: PW 1710). The Mössbauer spectra were recorded at about 300 K using a conventional constant acceleration spectrometer with a ^{57}Co source sealed in Rh matrix. Magnetization measurements were obtained by using a Quantum Design vibrating sample magnetometer operated between 10 K and 400 K [21]. These measurements included hysteresis loops, zero field cooling (ZFC) and field cooling (FC) magnetizations.

6.3 Results and discussion

6.3.1 X-ray diffraction

Figure 6.1 shows the XRD patterns for the $Mg_{0.2}Fe_xCr_{1.8-x}O_3$ alloys. The patterns confirm the formation of the basic corundum structure in all samples. These XRD results are similar to those of Sn doped α-Fe_2O_3 [66, 133]. No impurity phases were observed in the patterns. The refinement of XRD data was performed by Rietveld analysis (FullProfSuite for Windows) using a model involving a combination of both interstitial and substitutional Mg^{2+} ions in octahedral coordination [134]. The structure of α-Fe_2O_3 has Fe^{3+} ions distributed in an ordered fashion in 2/3 of the octahedral sites within a framework of hexagonally close-packed O^{2-} ions. Chains of face sharing octahedra are directed along the c axis, and the Fe^{3+} ions within each chain form pairs as shown in Figure 6.2. All refinements in which the oxygen occupancy was allowed to vary implied no vacancies on the oxygen sublattice and provided strong evidence of the validity of the model illustrated in Figure 6.3 [77]. The lower charge on magnesium ion

allows the formation of a linear defect cluster of three Mg^{2+} species. In the final stage of the refinements, the cation site occupancies were constrained in accordance with the model described above as shown in Table 6.1.The average grain sizes were obtained using the Debye-Scherrer equation (4.4.2) [114]. Direct measurement of the crystal lite sizes and powder morphology of the as-prepared samples were also performed by transmission electron microscopy (TEM). The TEM pictures are shown in Figures 6.4 and 6.5.

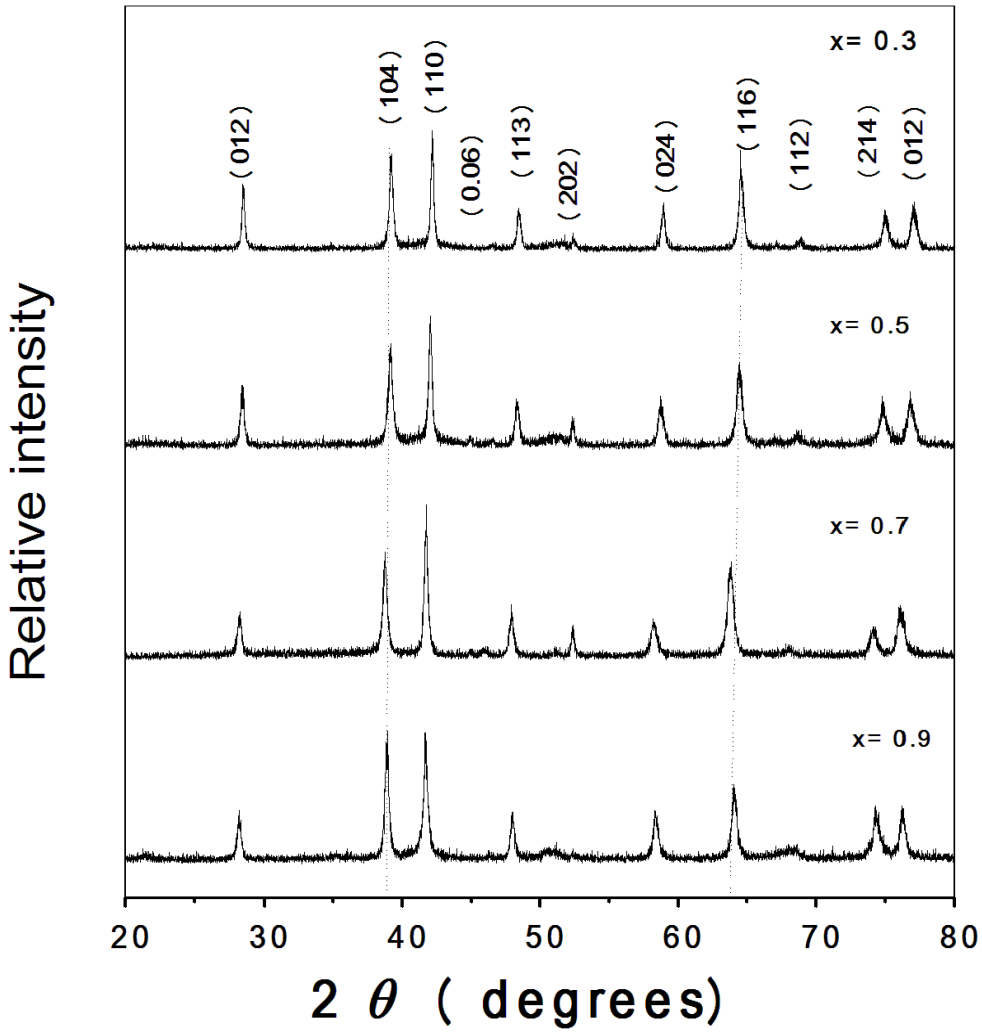

Figure 6.1: XRD patterns recorded for $Mg_{0.2}Fe_xCr_{1.8-x}O_3$ samples.

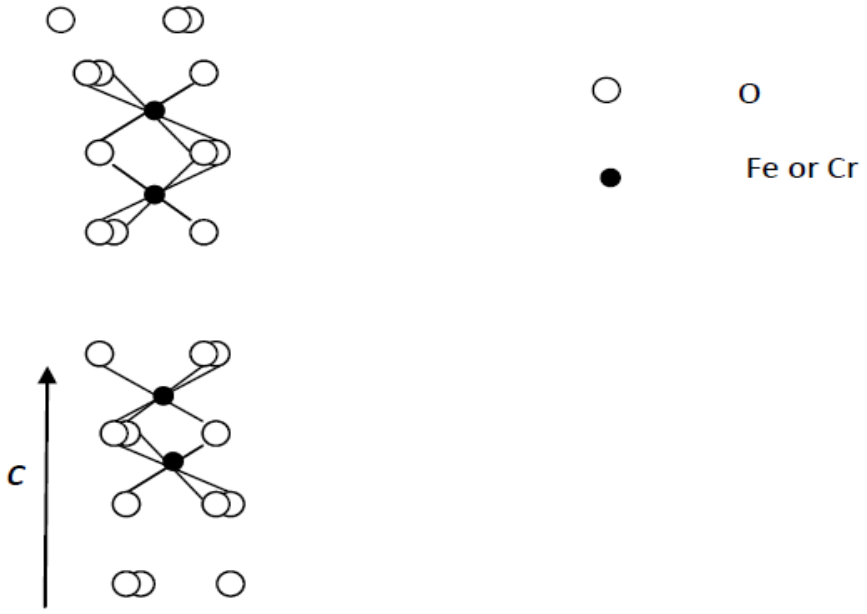

Figure 6.2: Linking of FeO_6 or CrO_6 octahedra along c in α-Fe_2O_3 or α-Cr_2O_3.

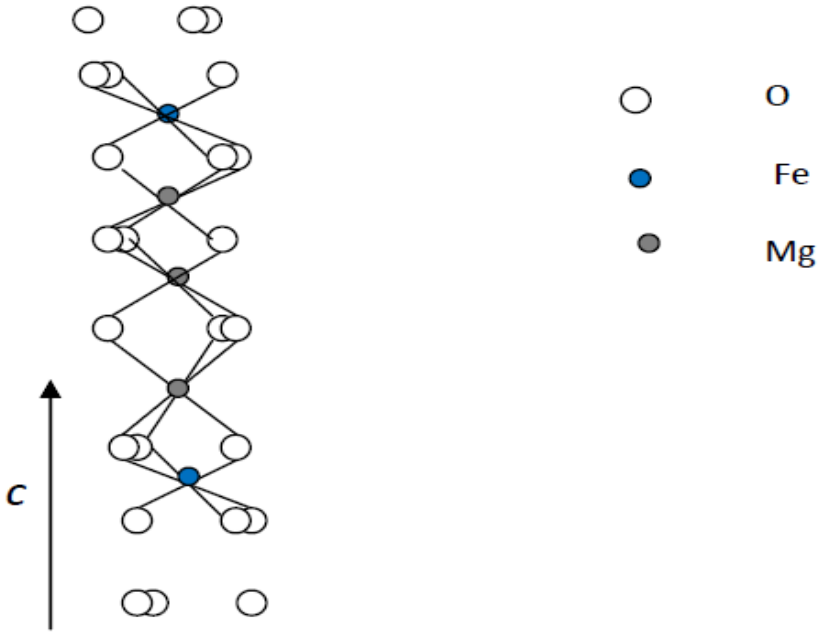

Figure 6.3: Structural model involving the substitution of $2Fe^{3+}$ or $2Cr^{3+}$ ions by $3Mg^{2+}$ ions.

Table 6.1: Refined Structural Parameters for $Mg_{0.2}Fe_xCr_{1.8-x}O_3$ samples.

Atom	x/a	y/b	z/c	$U_{iso}\times 100/\mathring{A}^2$	Occupancy
			$Mg_{0.2}Fe_{0.3}Cr_{1.5}O_3$		
Cr1	0.00000	0.00000	0.3463(2)	0.500(0)	9.026(2)
Fe	0.00000	0.00000	0.3463(2)	0.500(0)	1.696(2)
Mg1	0.00000	0.00000	0.3463(2)	0.500(0)	0.447(3)
Mg2	0.00000	0.00000	0.00000	0.000(0)	0.500(0)
O1	0.3215(1)	0.00000	0.2600(0)	0.500(0)	18.000(0)
R_{wp} (%)	13.4		R_{exp} (%)	10.5	
			$Mg_{0.2}Fe_{0.5}Cr_{1.3}O_3$		
Cr1	0.00000	0.00000	0.35173(2)	0.500(0)	8.694(2)
Fe	0.00000	0.00000	0.35173(2)	0.500(0)	2.318(2)
Mg1	0.00000	0.00000	0.35173(2)	0.500(0)	1.290(3)
Mg2	0.00000	0.00000	0.00000	0.000(0)	0.500(0)
O1	0.3317(1)	0.00000	0.2500(0)	0.500(0)	18.000(0)
R_{wp} (%)	14.4		R_{exp} (%)	12.5	
			$Mg_{0.2}Fe_{0.7}Cr_{1.1}O_3$		
Cr1	0.00000	0.00000	0.34690(0)	0.500(0)	9.055(0)
Fe	0.00000	0	0.34690(0)	0.500(0)	2.415(0)
Mg1	0.00000	0.00000	0.34690(0)	0.500(0)	0.270(0)
Mg2	0.00000	0.00000	0.00000	0.000(0)	0.500(0)
O1	0.3217(1)	0.00000	0.250(0)	0.500(0)	18.000(2)
R_{wp} (%)	12.4		R_{exp} (%)	11.5	
			$Mg_{0.2}Fe_{0.9}Cr_{0.9}O_3$		
Cr1	0.00000	0.00000	0.34690(0)	0.500(0)	10.260(0)
Fe	0.00000	0.00000	0.34690(0)	0.500(0)	1.207(0)
Mg1	0.00000	0.00000	0.34690(0)	0.500(0)	0.270(0)
Mg2	0.00000	0.00000	0	0.000(0)	0.500(0)
O1	0.30800(0)	0.00000	0.2500(0)	0.500(0)	18.000(0)
R_{wp} (%)	13.4		R_{exp} (%)	10.5	

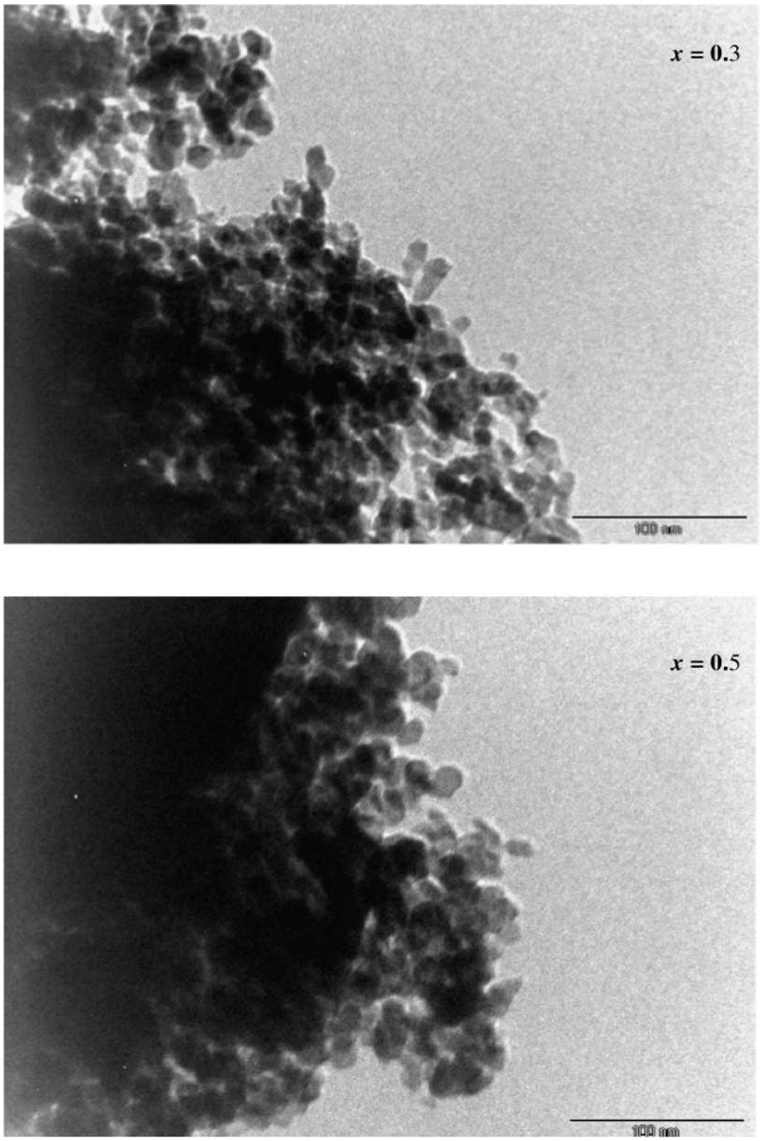

Figure 6.4: TEM micrographs for $Mg_{0.2}Fe_{0.3}Cr_{1.5}O_3$ and $Mg_{0.2}Fe_{0.5}Cr_{1.3}O_3$ samples.

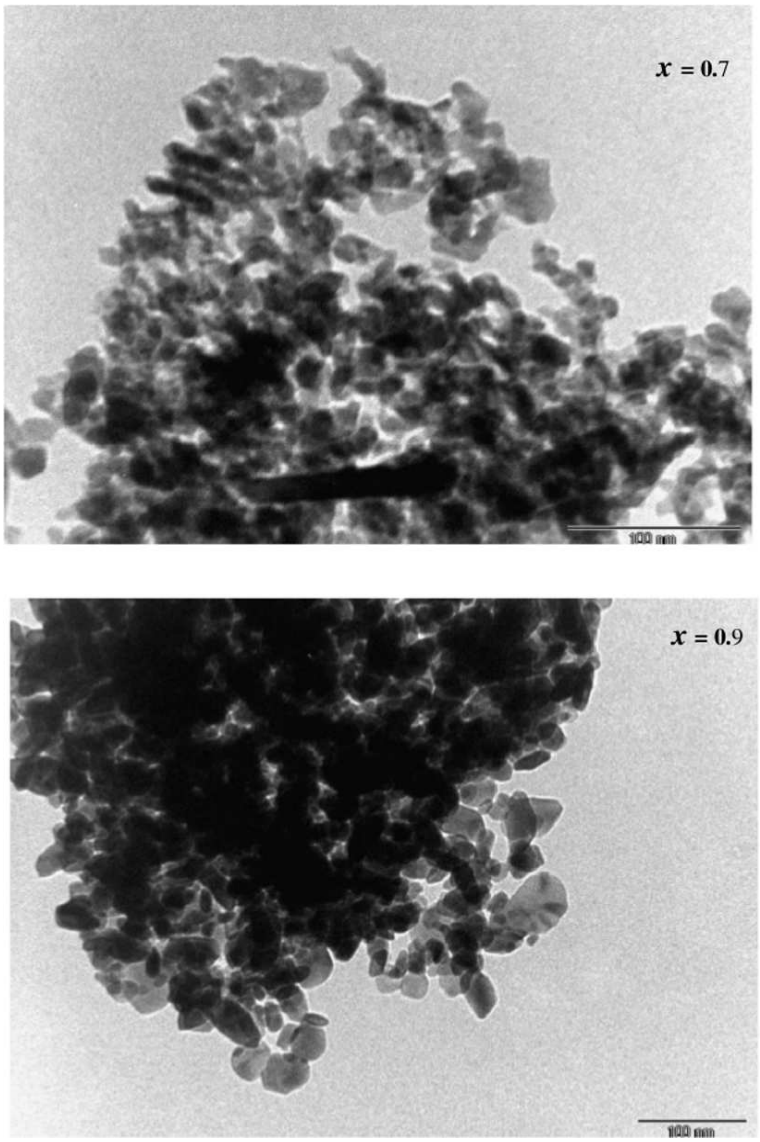

Figure 6.5: TEM micrographs for $Mg_{0.2}Fe_{0.7}Cr_{1.1}O_3$ and $Mg_{0.2}Fe_{0.9}Cr_{0.9}O_3$ samples.

The shapes of the particles appear to be nearly spherical with a significant spread in the particle sizes for all the alloys studied. Hence, the mean square estimation of the diameters has been used to calculate the average grain size D_{TEM} from at least 30 particles on each micrograph. The lattice parameters, the average particle diameters as calculated from XRD data (D_{XRD}) and observed by TEM measurements (D_{TEM}) are shown in Table 6.2. The calculated D_{XRD} and measured D_{TEM} values of the particle sizes are in good agreement. The particle sizes appear to be sensitive to Cr concentration for $x = 0.3$, 0.5 and 0.9 where a reduction in particle sizes is observed with increase in Fe content except for the $x = 0.7$ alloy which has an unusually high particle size. This alloy appears more relaxed with slightly higher unit cell volume which we assume to be more likely due to longer synthesis or sintering time.

Table 6.2: Particle sizes (D_{XRD}), (D_{TEM}) and lattice parameters for as-prepared $Mg_{0.2}Fe_xCr_{1.8-x}O_3$ samples.

x	$a = b$ (Å) $\pm 10^{-3}$	c (Å) $\pm 10^{-3}$	V (Å^3) $\pm 10^{-3}$	D_{XRD} (nm) ± 0.8	D_{TEM} (nm) ± 2
0.3	4.986	13.621	295.43	55.6	53
0.5	4.985	13.643	294.34	42.5	41
0.7	5.001	13.622	296.23	65.9	64
0.9	4.962	13.586	291.4	32.8	37

6.3.2 Mössbauer measurements

The variation of Mössbauer spectra as a function of x for the $Mg_{0.2}Fe_xCr_{1.8-x}O_3$ recorded at room temperature is shown in Figure 6.6. It can been seen that the spectra of the samples with $x = 0.3$ and $x = 0.5$ are paramagnetic doublets. The spectra for $x = 0.7$ and 0.9 show paramagnetic component with a non-zero electric field gradient around ^{57}Fe isotopes. The spectra for alloys with low Fe concentration ($x \leq 0.5$) were best fitted to two doublets. The doublets are associated with Fe ions in paramagnetic spin states. For $x = 0.7$and 0.9, the spectra show the superposition of a sextet pattern and a broad doublet. In this case the spectra could be fitted to a single sextet and a doublet patterns.

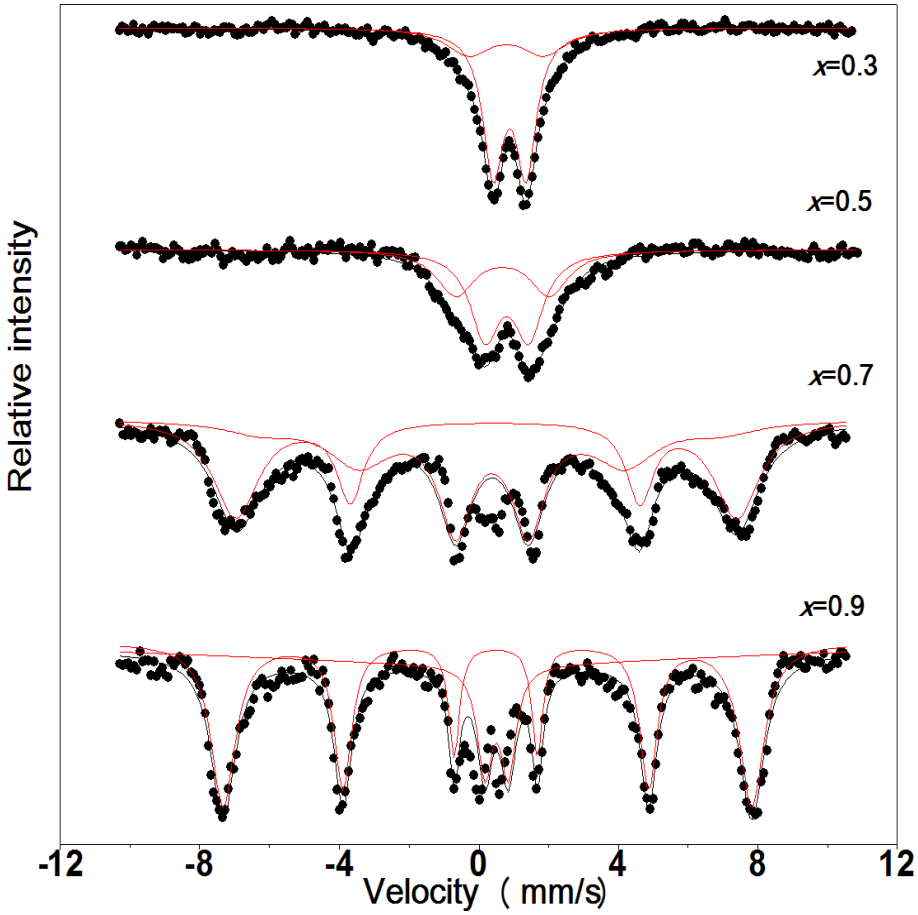

Figure 6.6: Room temperature ^{57}Fe Mössbauer spectra recorded for $Mg_{0.2}Fe_xCr_{1.8-x}O_3$ samples. The solid lines are the LSQ fits.

The solid lines are the result of fittings to the experimental data and correspond to individual components (sextets or doublets). There was no significant change in isomer shifts and quadrupole splitting with increasing x. A slight increase in hyperfine fields from 442 kOe to 469 kOe has been observed for the fitting sextet. This is due to an increase in Fe content, a behavior that can increase T_N. The ^{57}Fe Mössbauer spectra showed no evidence for the oxidation of Fe^{3+} to Fe^{2+} as result of the incorporation of Mg^{2+}. This is therefore consistent with charge balance not involving a change in the oxidation state of iron. The Mössbauer fit parameters are presented in Table 6.3.

Table 6.3: Hyperfine parameters from Mössbauer spectra recorded at room temperature for the as-prepared samples of $Mg_{0.2}Fe_xCr_{1.8-x}O_3$. The solid line is the LSQ fits.

T = 300 K	doublet 1			doublet 2			sextet 1			
	δ	Δ	f	δ	Δ	f	δ	2ε	H	f
Sample	mm/s	mm/s	%	mm/s	mm/s	%	mm/s	mm/s	kOe	
x	± 0.01	± 0.02		± 0.01	± 0.02		± 0.01	± 0.02	± 3	
Reflux										
0.3	0.35	0.9	29	0.36	0.39	71				
0.5	0.33	0.52	59	0.29	1.11	41				
0.7	0.37	1.07	25				0.36	-0.11	442	75
0.9	0.32	0.67	17				0.37	-0.11	469	83

6.3.3 Magnetization measurements

The magnetic properties of the $Mg_{0.2}Fe_xCr_{1.8-x}O_3$ nanooxides were also determined. The temperature variation of the magnetization for the as-prepared samples measured after zero field cooling (ZFC) and field cooling (FC) regimes are shown in Figures 6.7-6.10. The lower curve for each sample in all Figures correspond to ZFC and the upper curve to FC. During FC, the samples were cooled from 400 K to 10 K in the presence of an external magnetic field of 50 Oe. For ZFC measurements, the samples were cooled to 10 K in zero field. The magnetizations were recorded during warming up to 400 K in the presence of the same external field. The magnetization for the FC curve decreases

continuously with increasing temperature. With decreasing temperature both ZFC and FC magnetizations rise and separate at a temperature (T_G) where it is assumed that the ferromagnetic (FM) clusters begin to form [144] due to short range coupling of magnetic moments. At a lower temperature T_B called the blocking or freezing temperature the ZFC magnetizations reach a maximum where the moments of the FM clusters begin to freeze. The blocking temperature depends on the average particle size [128]. As expected T_B increases with increased particle size for all samples except for the $x = 0.7$ sample. The width of the peak in ZFC curve is associated with particle size distribution. A narrow peak observed in ZFC curve for $x = 0.9$ indicates narrow distribution of particle sizes. A bifurcation between the FC and ZFC curves usually implies the existence of a cluster-glass [144, 145] and is possibly due to the magnetic frustration induced by the surface-driven spin frustration and disorder in the nanoparticles [146], [147, 148]. These results indicate cluster-glass-like behavior. According to equation (2.4.36) and as shown in Figure 2.3, the linear fits for the temperature dependence of the inverse magnetization show that the samples exhibit Curie-Weiss type behavior above 286 K and 290 K for $x = 0.7$ and $x = 0.9$ respectively. The corresponding extrapolated paramagnetic Weiss temperatures θ_p are -354 K and -722 K. The corresponding effective magnetic moments are 3.83 μ_{eff} and 4.23 μ_{eff}. The theoretical value can be obtained as follows: $\mu_{eff} = (0.2\times5.92 + 0.9\times3.87)\mu_B = 4.67$ μ_B. The experimental values are slightly smaller than the theoretical value. Figure 6.11 shows typical results for $x = 0.9$. The large negative values of θ_p indicate that the antiferromagnetic (AFM) interactions in $Mg_{0.2}Fe_xCr_{1.8-x}O_3$ are strong. Figures 6.12 to 6.15 show the field dependencies of the magnetization for different compositions in the alloys series $Mg_{0.2}Fe_xCr_{1.8-x}O_3$ recorded at 400 K. The inset of these figures show the amplified hysteresis loop.

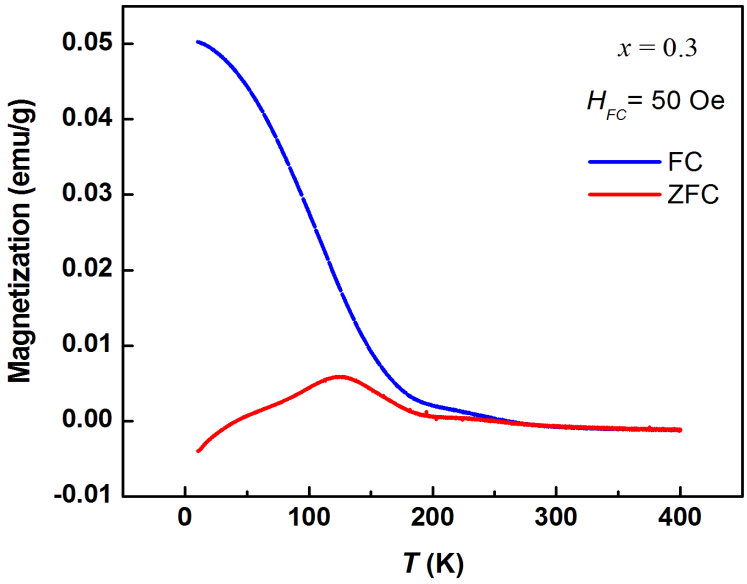

Figure 6.7: Temperature dependence of ZFC and FC magnetizations of the as-prepared $Mg_{0.2}Fe_{0.3}Cr_{1.5}O_3$ sample.

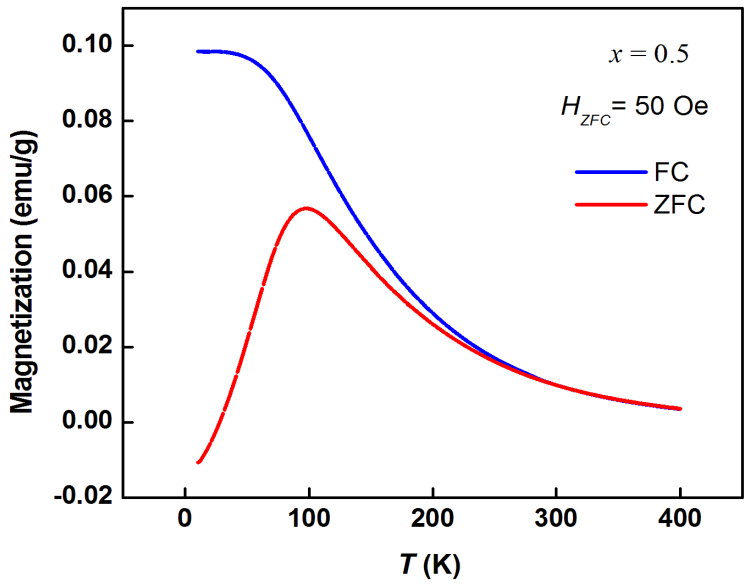

Figure 6.8: Temperature dependence of ZFC and FC magnetizations of the as-prepared $Mg_{0.2}Fe_{0.5}Cr_{1.3}O_3$ sample.

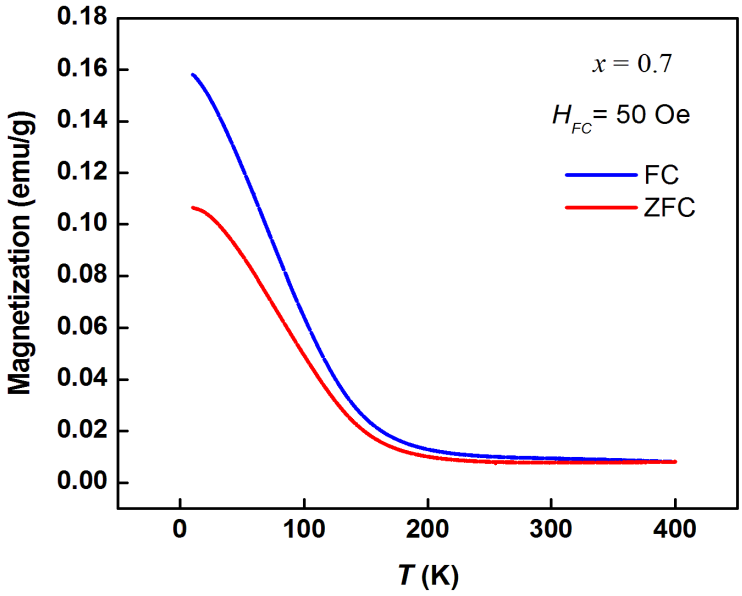

Figure 6.9: Temperature dependence of ZFC and FC magnetizations of the as-prepared $Mg_{0.2}Fe_{0.7}Cr_{1.1}O_3$ sample.

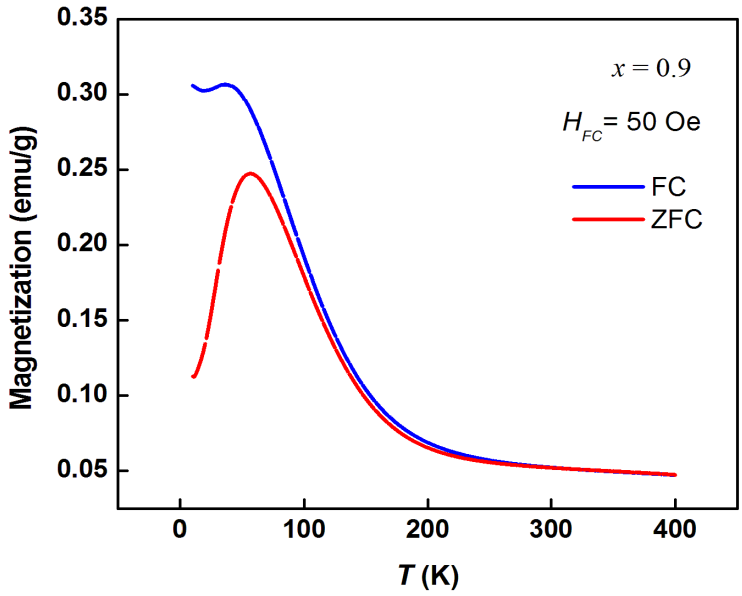

Figure 6.10: Temperature dependence of ZFC and FC magnetizations of the as-prepared $Mg_{0.2}Fe_{0.9}Cr_{0.9}O_3$ sample.

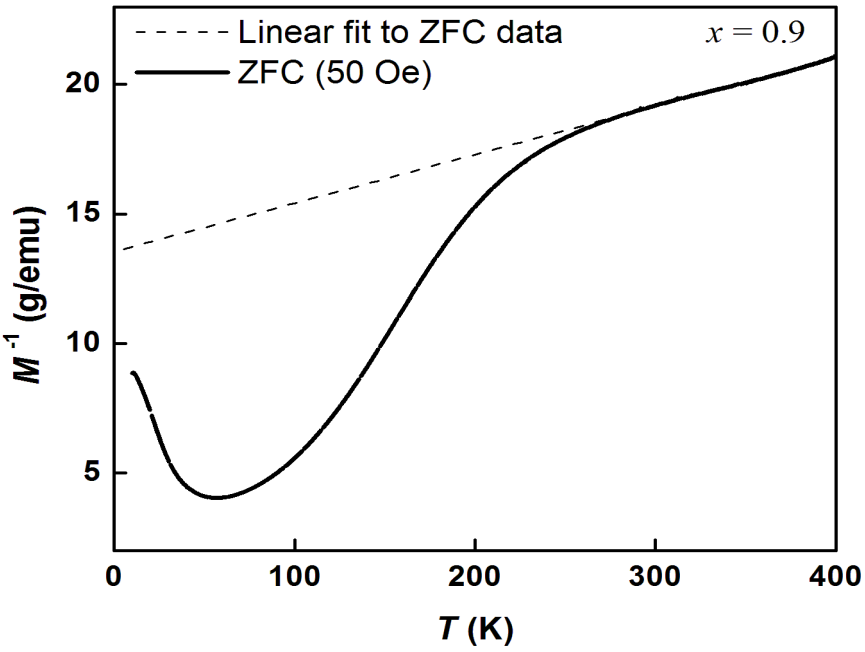

Figure 6.11: Linear fit for the temperature dependence of the inverse magnetization for the $Mg_{0.2}Fe_xCr_{1.8-x}O_3$ for x=0.9 sample.

An anomalous variation of magnetization with low magnetic field is observed. This behavior might have application in magnetic switching devices. For purely paramagnetic phases, the magnetization curves at 400 K should be straight lines across the first and third quadrants in the hysteresis loops. However, the plots show that in addition to a paramagnetic phase there is a small magnetic phase in all samples at 400 K. The paramagnetic phase is consistent with doublets in the Mössbauer spectra obtained at 300 K. The magnetic phase appears to grow with an increase in the Fe content of the alloys as indicated by increased hysteresis. We assume that at low temperature, the small magnetic phase evolves into FM clusters which eventually freeze at the blocking temperature while the dominant paramagnetic phase evolves into AFM phase below its corresponding Néel temperature (T_N). An increase in coercivity was observed from 400 K to 10 K. The measurements of hysteresis loops at 10 K shown in Figure 6.16-6.19 were performed after field cooling (FC) and zero field cooling (ZFC) measurements. The hysteresis loops are not symmetrical about the origin but are slightly shifted to

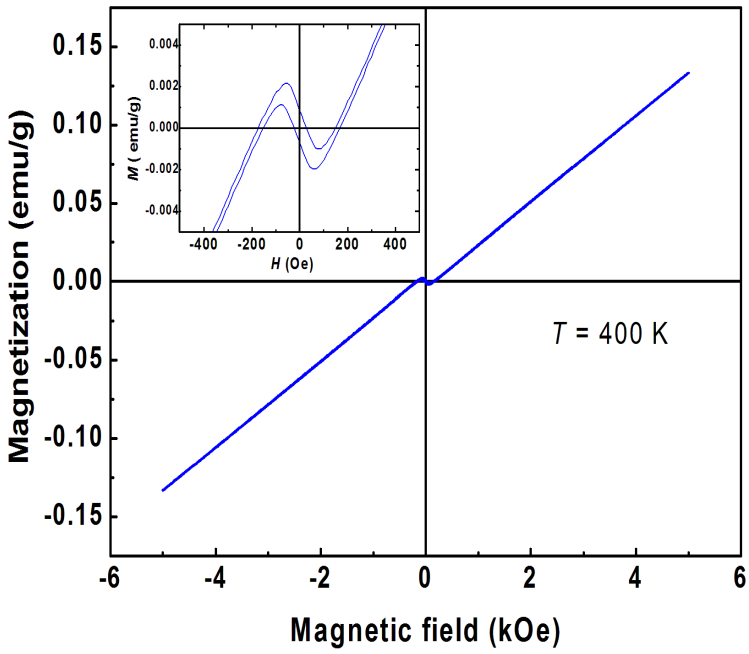

Figure 6.12: Magnetization curves of the $Mg_{0.2}Fe_{0.3}Cr_{1.5}O_3$ sample measured at 400 K. The inset shows the amplified hysteresis loop.

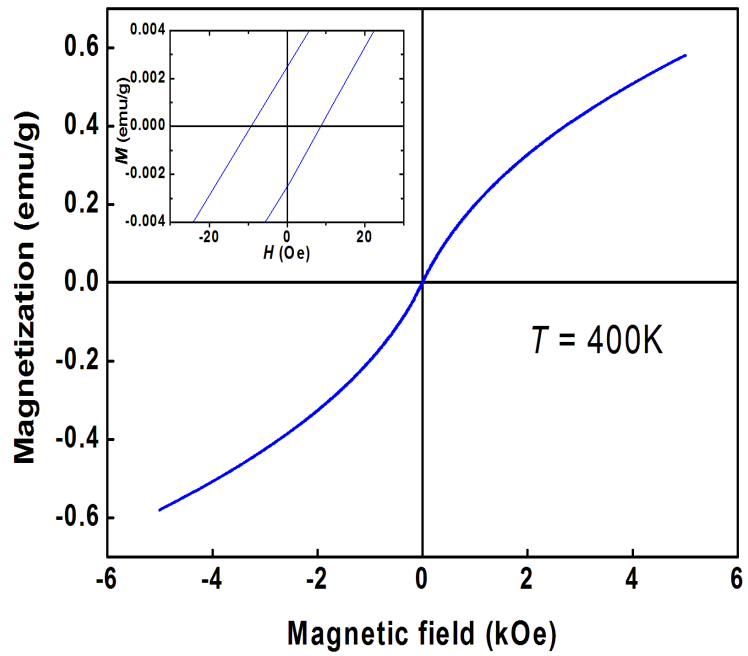

Figure 6.13: Magnetization curves of the $Mg_{0.2}Fe_{0.5}Cr_{1.3}O_3$ sample measured at 400 K. The inset shows the amplified hysteresis loop.

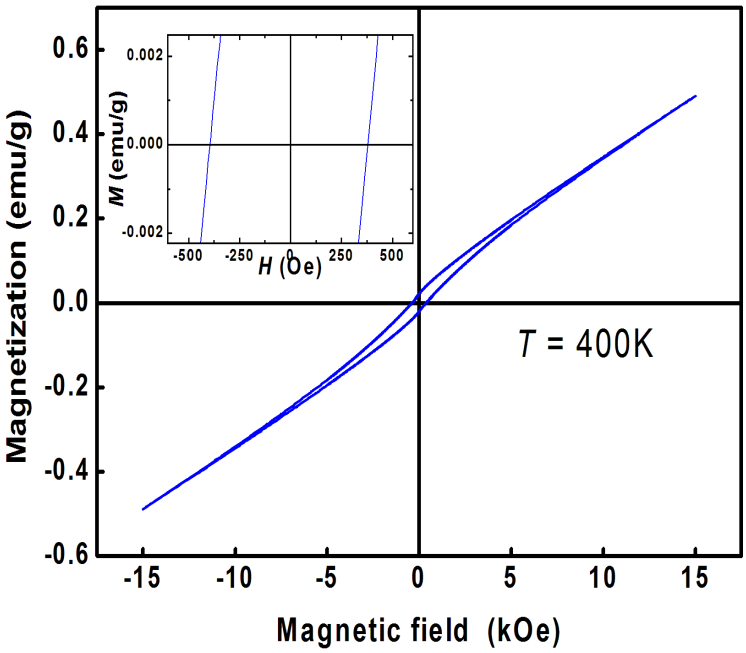

Figure 6.14: Magnetization curves of the $Mg_{0.2}Fe_{0.7}Cr_{1.1}O_3$ sample measured at 400 K. The inset shows the amplified hysteresis loop.

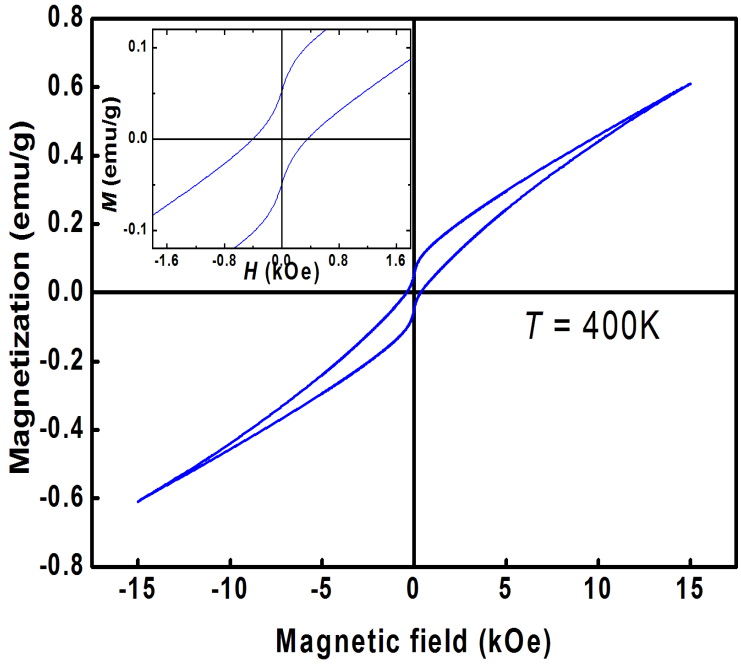

Figure 6.15: Magnetization curves of the $Mg_{0.2}Fe_{0.9}Cr_{0.9}O_3$ sample measured at 400 K. The inset shows the amplified hysteresis loop.

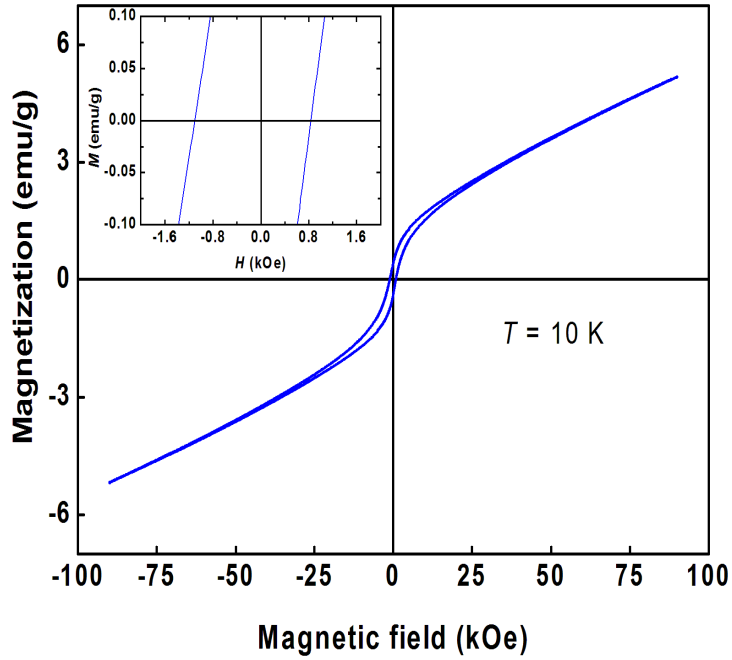

Figure 6.16: Magnetization curves of the $Mg_{0.2}Fe_{0.3}Cr_{1.5}O_3$ sample measured at 10 K. The inset shows the amplified hysteresis loop.

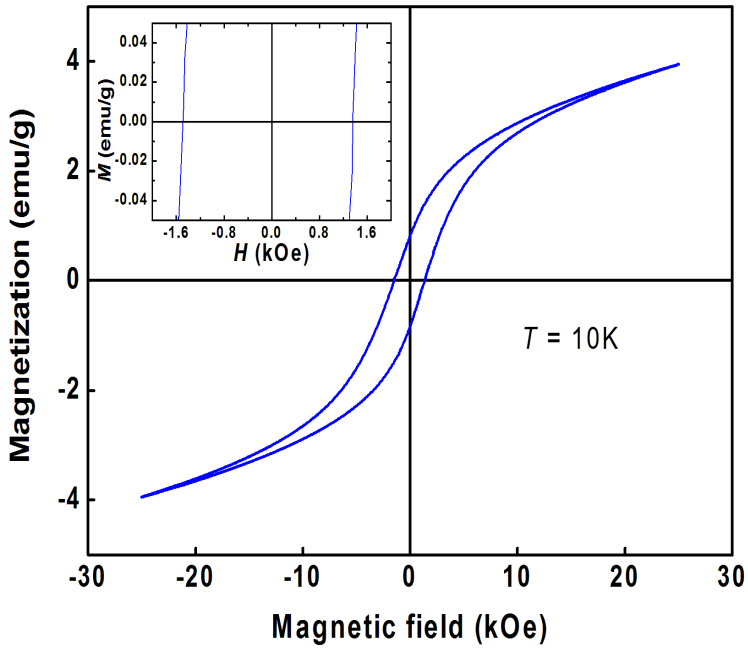

Figure 6.17: Magnetization curves of the $Mg_{0.2}Fe_{0.5}Cr_{1.3}O_3$ sample measured at 10 K. The inset shows the amplified hysteresis loop.

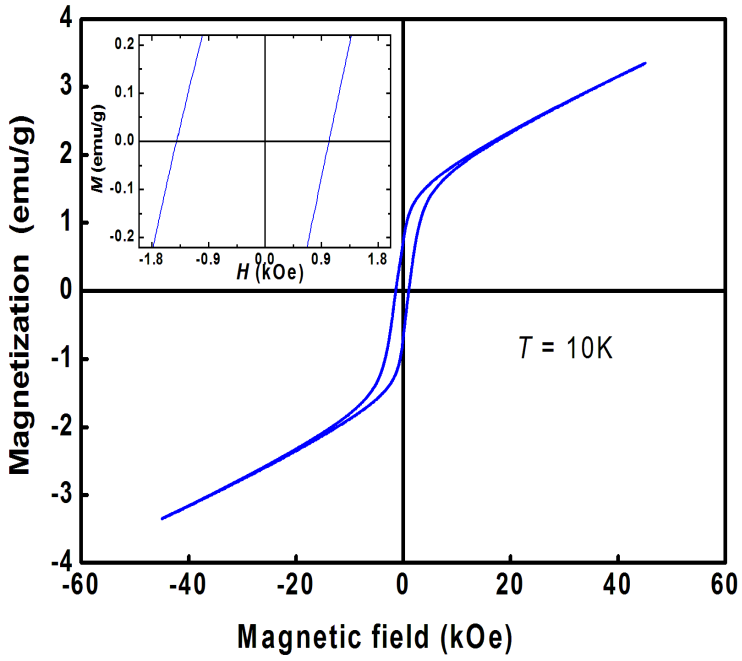

Figure 6.18: Magnetization curves of the $Mg_{0.2}Fe_{0.7}Cr_{1.1}O_3$ sample measured at 10 K. The inset shows the amplified hysteresis loop.

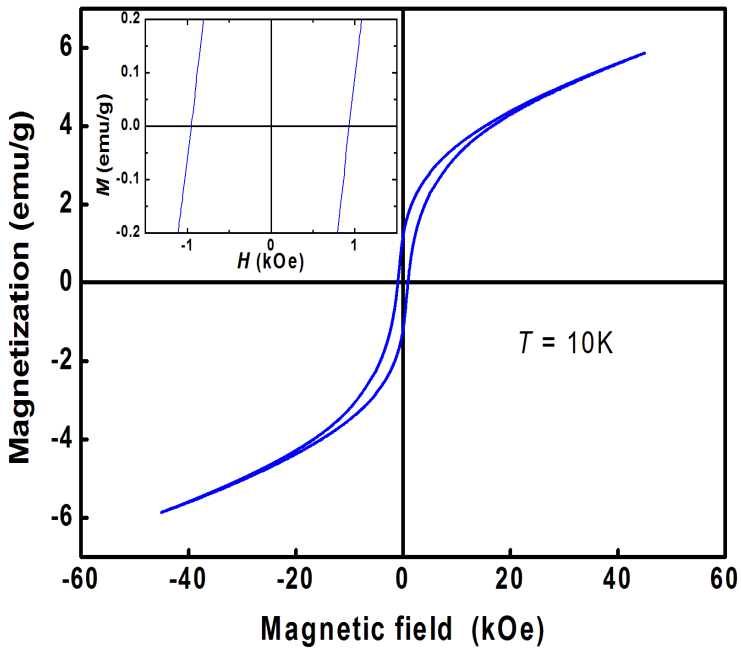

Figure 6.19: Magnetization curves of the $Mg_{0.2}Fe_{0.9}Cr_{0.9}O_3$ sample measured at 10 K. The inset shows the amplified hysteresis loop.

the left side. The shift of the hysteresis loop along the field axis is associated with exchange bias effects [149]. The direct exchange interaction between ferromagnetic and anti-ferromagnetic spins in a common interface results in unidirectional magnetic anisotropy seen as exchange bias effect. The theory of exchange bias effect was discussed in Chapter 2. In the present case for $Mg_{0.2}Cr_{1.8-x}Fe_xO_3$ nanoparticle alloys, the exchange bias is due to the exchange interaction between the antiferromagnetic (AFM) and ferromagnetic (FM) spin clusters dominated by Cr and Fe atoms respectively. The exchange bias phenomenon has applications in magneto-electronic switching devices, random access magnetic storage units, magnetic sensors and spintronics devices [150]. The exchange bias field is defined as

$$H_{EB} = |\frac{H_{C1} - H_{C2}}{2}| \tag{6.3.1}$$

where H_{C1} and H_{C2} are coercive fields at the left and right side of the shifted magnetization curves respectively [150]. The values of the exchange bias field H_{EB} deduced from hysteresis loops measured at 10 K are shown in Table 6.3, which we can correlate with iron content x and particle sizes presented in Table 6.1. In Figure 6.20 we observe that there is no correlation between H_{EB} and iron content x. Figure 6.21 shows the particle size dependence of H_{EB} for all our samples. The exchange bias field H_{EB} seems to correlate very well with the particle sizes D. This is consistent with previous studies which show larger bias at larger particle sizes [150, 151]. The presence of AFM domains in this case is expected to account for the particle size dependence of H_{EB} by an argument similar to AFM layer thickness dependence of FM-AFM films [151]. The correlation in Figure 6.21 is also interesting because it suggests a critical particle size of about 31 nm when H_{EB} is zero for this series of alloys.

Table 6.4: Values of exchange bias fields for as-prepared $Mg_{0.2}Fe_xCr_{1.8-x}O_3$ samples annealed at 600 °C.

x	H_{EB} (Oe) $\pm$ 0.5	D_{XRD} (nm) $\pm$ 0.04
0.3	135.0	55.61
0.5	64.1	42.32
0.7	192.3	65.91
0.9	10.2	32.83

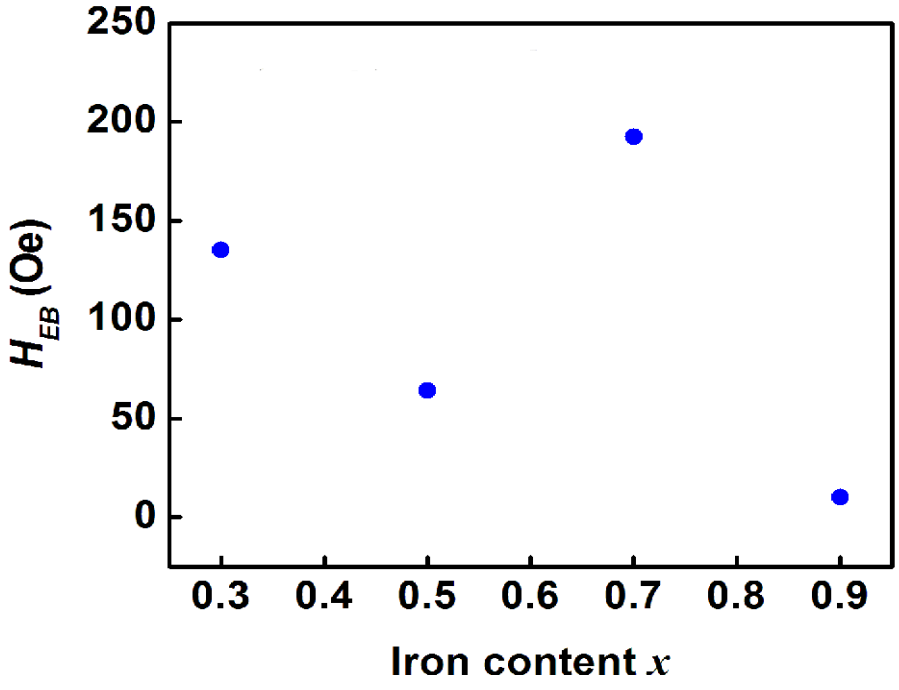

Figure 6.20: Iron content dependence of exchange bias field H_{EB} for the $Mg_{0.2}Fe_xCr_{1.8-x}O_3$ samples measured at 10 K.

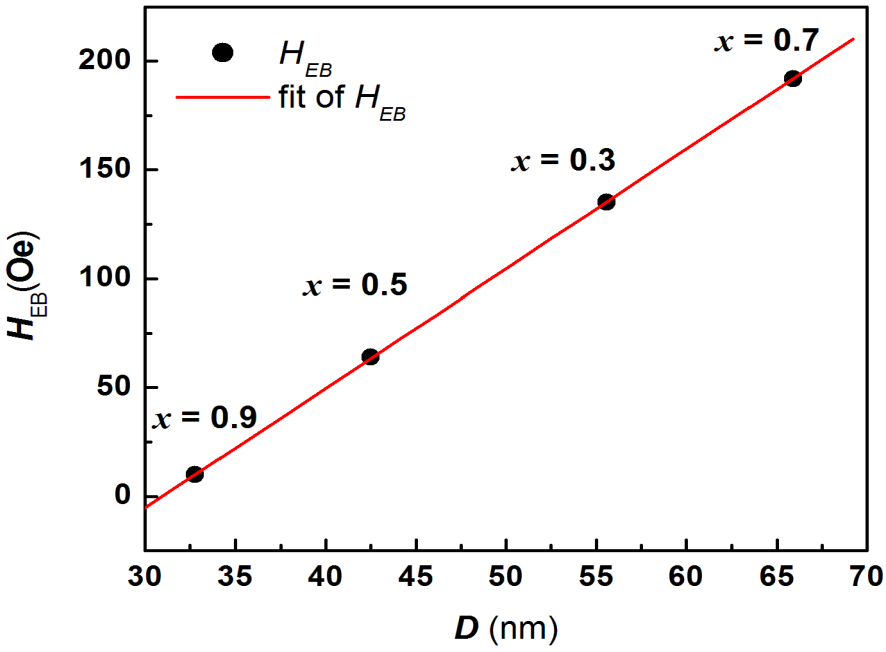

Figure 6.21: Particle size dependence of exchange bias field H_{EB} for the $Mg_{0.2}Fe_xCr_{1.8-x}O_3$ samples measured at 10 K. The solid line is the linear fit to the data with a correlation coefficient of 0.999.

6.3.4 Conclusion

We have successfully prepared $Mg_{0.2}Fe_xCr_{1.8-x}O_3$ nanoparticle alloys by hydrothermal process. An anomalous variation of magnetization in low fields has been observed. Our results from 400 K to 10 K show evidence of strong antiferromagnetic (AFM) interactions in the alloys. The results also show the presence of weak ferromagnetic (FM) clusters. The nanoparticle oxides have been found to exhibit exchange bias effects which appear to be sensitive to particle sizes. Samples with larger grains show more enhanced exchange bias effect. A strong linear relationship between the exchange bias field (H_{EB}) and particles sizes (D) has been observed for particle sizes between 32 and 66 nm.

Chapter 7

Effect of annealing on exchange bias in $Mg_{0.2}Fe_xCr_{1.8-x}O_3$ nano oxides

7.1 Introduction

Exchange bias is a phenomenon associated with induced exchange anisotropy at the interface between ferromagnetic (FM) and antiferromagnetic (AFM) phases in a heterogeneous system [98]. The exchange bias considerably increases the total anisotropy of the system, which has technological applications for magnetic storage, spin-electron devices and the development of permanent magnets [149]. The exchange bias is observed as the unidirectional shift of a hysteresis loop when a system is cooled down to low temperatures in an external applied magnetic field below the Néel temperature of the AFM phase. In addition to the exchange bias at the FM/AFM interface, exchange bias has also been reported for different systems which involve glassy magnetic behaviour such as FM/spin-glass (SG) bilayer films, core-shell structure and intrinsically phase separated cluster-glass (CG) alloys [152–155]. In most cases, the exchange bias has been investigated on artificially fabricated heterogeneous systems consisting of FM/AFM or FM/SG bilayers or core-shell structures. A fundamental understanding of the nature of intrinsic phase separation of the alloys is therefore important for technological applications. Nieebieskikwiat *et al.* [156] and Qian *et al.* [157] have

reported strong effect of exchange bias in the case of charge ordered manganites such as $Pr_{1/3}Ca_{2/3}MnO_3$ and $Y_{0.2}Ca_{0.8}MnO_3$. The exchange bias is also reported for cluster-glass cobaltites La(Ba, Sr)CoO_3, where the exchange bias is due to the cluster-glass consisting of FM and SG phases [154], [155]. Recently we observed the exchange bias phenomenon in $Mg_{0.2}Fe_xCr_{1.8-x}O_3$ annealed at 600 °C for 12 hours [158]. In this chapter we extend the results presented in chapter 6 and we investigate the effect of further annealing the $Mg_{0.2}Fe_xCr_{1.8-x}O_3$ nanoparticles on the exchange bias effect.

7.2 Experimental details

High-purity metal chlorides were used as starting materials to make 0.1 molar (M) solutions for synthesis of $Mg_{0.2}Fe_xCr_{1.8-x}O_3$ nano oxides by hydrothermal reaction. The synthesis procedure is similar to what we have presented before [20, 21]. The resulting homogeneous powders were heated in air at 700 °C for 12 hours. The X-ray diffraction (XRD) patterns of the samples were obtained by using CoKα radiation (λ = 1.7903 Å) on a Philips diffractometer (type: PW 1710). The magnetization measurements were performed using two different systems, namely a Lakeshore model 735 vibrating sample magnetometer (VSM) for room temperature measurements and a Mini cryogen free system for magnetization measurements in applied magnetic fields of up to 50 kOe in the temperature range of 2 - 300 K.

7.3 Results and discussion

7.3.1 X-ray diffraction

Figure 7.1 shows the XRD patterns for the $Mg_{0.2}Cr_{1.8-x}Fe_xO_3$ alloys annealed at 700 °C. The patterns confirm the persistence of the basic corundum structure in all the samples. These XRD results are similar to those of Sn doped α-Fe_2O_3 presented in Chapter

5 [66, 133] and which were interpreted in terms of tin occupying both octahedral, interstitial and substitutional sites. The average particle sizes were obtained using the Debye-Scherrer equation (4.4.2) [114] and are recorded in Table 7.1.

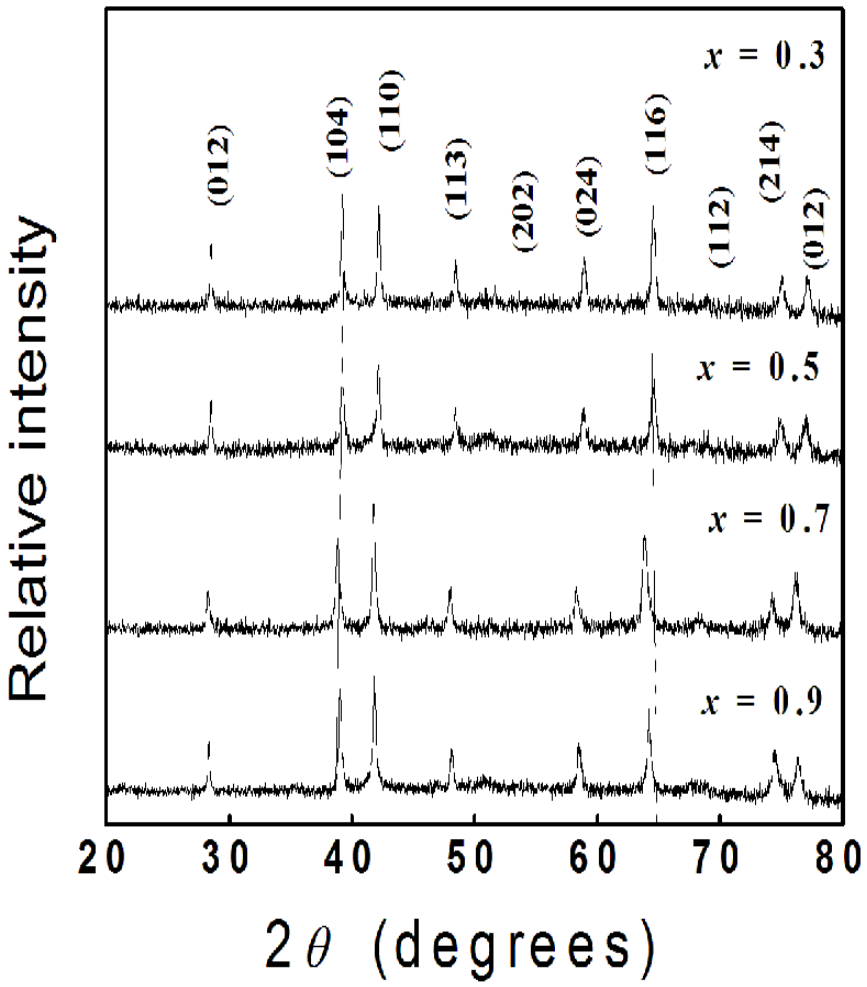

Figure 7.1: XRD patterns for $Mg_{0.2}Fe_xCr_{1.8-x}O_3$ samples annealed at 700 °C.

Table 7.1: Particle size (D_{XRD}) for $Mg_{0.2}Fe_xCr_{1.8-x}O_3$ samples.

x	D_{XRD} (nm) $\pm$ 0.8
0.3	56.45
0.5	44.01
0.7	66.55
0.9	34.01

7.3.2 Magnetization measurements

The magnetic properties of the $Mg_{0.2}Fe_xCr_{1.8-x}O_3$ nano oxides annealed at 700 °C were also determined. Figures 7.2 to 7.5 show the field dependencies of the magnetization for different compositions in the alloys series $Mg_{0.2}Fe_xCr_{1.8-x}O_3$ recorded at 300 K. The results show that the hysteresis loops for samples with $x \leqslant 0.5$ appear to consist of a paramagnetic phase where the $M-H$ plots are almost linear. For samples with $x > 0.5$ there is an additional small magnetically ordered phase in low fields associated with hysteresis. The samples exhibit nearly zero remanence and zero coercivity suggesting a superparamagnetic behavior of the nanocrystalline iron oxides [20]. The magnetic phase appears to grow with increase in the Fe content of the alloys as indicated by increased hysteresis. We observe that at low temperature, the small magnetic phase evolves into FM clusters which eventually freeze at a blocking temperature while the dominant paramagnetic phase evolves into AFM phase below its corresponding Néel temperature (T_N). The hysteresis loops recorded at different temperatures are shown in Figures 7.6 - 7.9. It is worth noting that in the $M-H$ curves, the magnetization

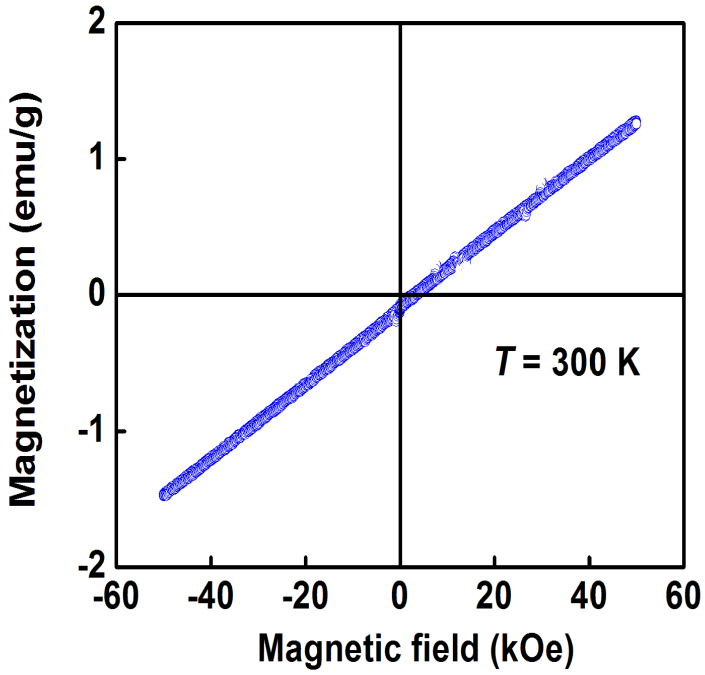

Figure 7.2: Hysteresis loop measured for $Mg_{0.2}Fe_{0.3}Cr_{1.5}O_3$ sample.

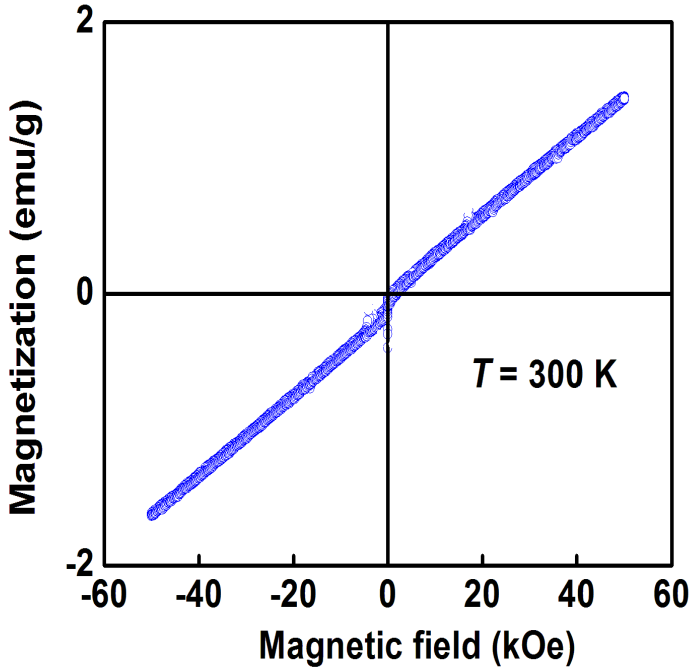

Figure 7.3: Hysteresis loop measured for $Mg_{0.2}Fe_{0.5}Cr_{1.3}O_3$ sample.

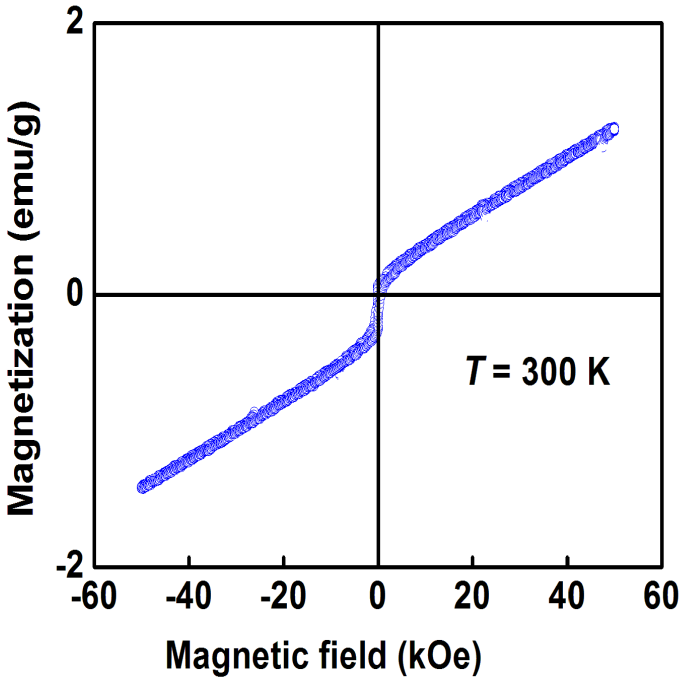

Figure 7.4: Hysteresis loop measured for $Mg_{0.2}Fe_{0.7}Cr_{1.1}O_3$ sample.

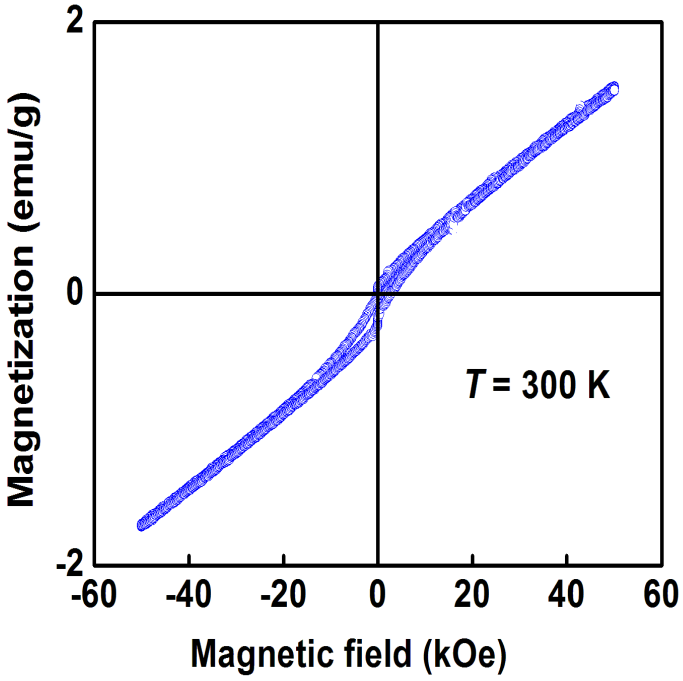

Figure 7.5: Hysteresis loop measured for $Mg_{0.2}Fe_{0.9}Cr_{0.9}O_3$ sample.

value increases and does not reach saturation even at the highest magnetic field. This can indicate the dominant role of the AFM components. Thus the $Mg_{0.2}Fe_xCr_{1.8-x}O_3$ may be considered to be composed of AFM cores and FM cluster-glass-like shells. As the temperature is lowered, the finite-range ferromagnetic ordering is constructed in the shell, and the FM clusters form and begin to freeze around the freezing temperature (T_f). At low temperature, the samples become magnetically harder due to spin-freezing. The coercive fields increase with decreasing temperature. The coercive field is defined as

$$H_C = \frac{|H_{C1}| + |H_{C2}|}{2}, \tag{7.3.1}$$

where $|H_{C1}|$ and $|H_{C2}|$ relate to the left and right shifts of the hysteresis loops respectively [159]. The raw data for the coercive fields are recorded in Table 7.2 and the temperature dependence of the coercive field H_C obtained from hysteresis loops in the temperature range 2 to 100 K for the $Mg_{0.2}Fe_xCr_{1.8-x}O_3$ samples studied are shown in Figures 7.10 - 7.13. The temperature dependence of H_C follows well the formula

$$H_C = H_C(0)\exp(-T/T_1), \tag{7.3.2}$$

where $H_C(0)$ is the extrapolated coercive field at absolute zero temperature and T_1 is a constant [159]. The coercive field data is fitted over the entire temperature range with $T_1 = 59.2 \pm 0.1$ K, 143.4 ± 0.2 K, 30.1 ± 0.1 K and 18.1 ± 0.3 K for $x = 0.3$, 0.5, 0.7 and 0.9 respectively.

Table 7.2: Values of coercive fields for $Mg_{0.2}Fe_xCr_{1.8-x}O_3$ samples annealed at 700 °C.

x	0.3	0.5	0.7	0.9
T (K)	H_C (Oe) $\pm$ 0.5	H_C (Oe) $\pm$ 0.5	H_C (Oe) $\pm$ 0.5	H_C (Oe) $\pm$ 0.5
2	150.2	167.3	219.1	263.1
10	142.2	161.2	112.3	156.1
30	110.3	114.1	114.3	114.2
60	87.2	87.3	33.1	79.1
100	67.2	37.2	17.1	37.2

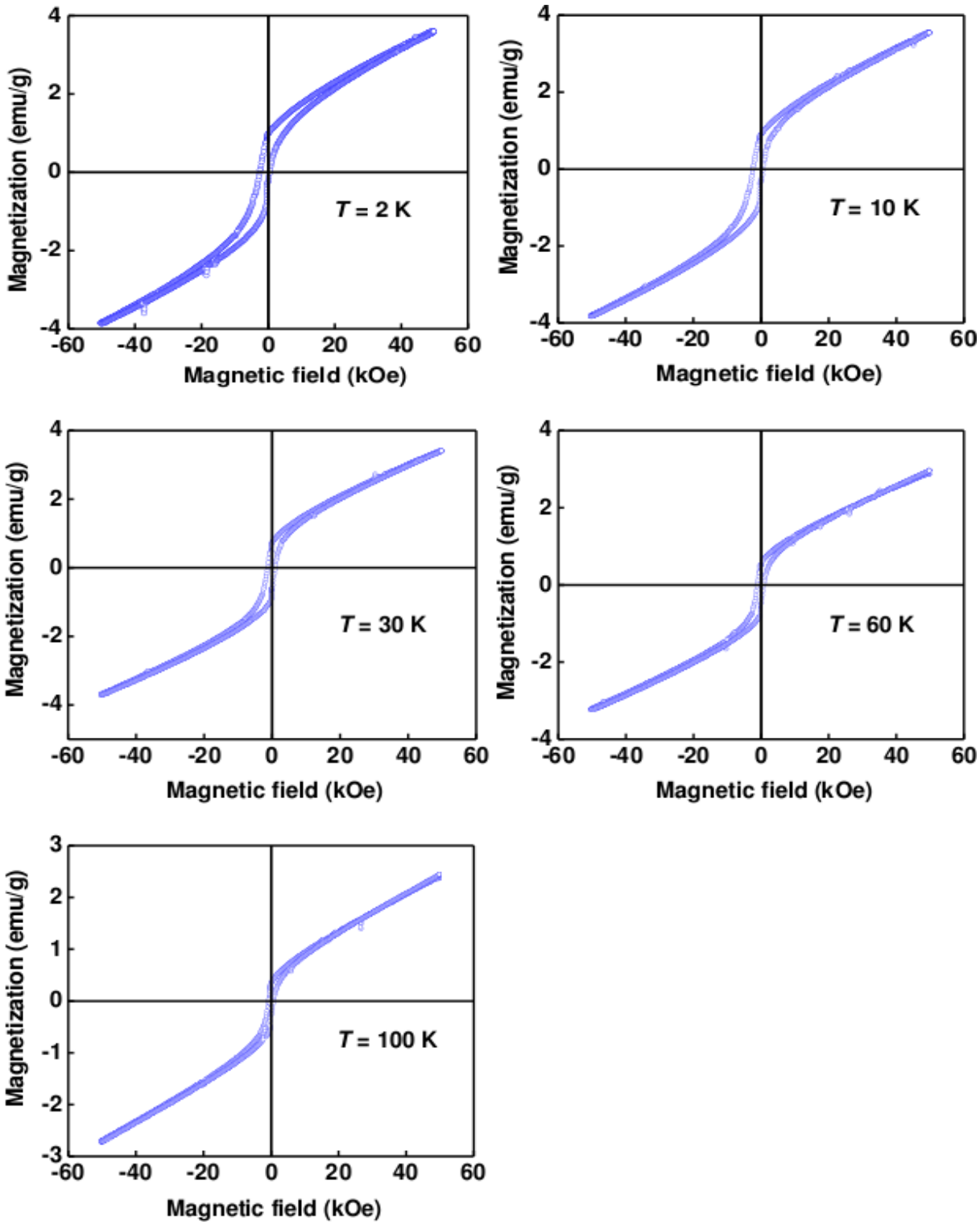

Figure 7.6: Hysteresis loops measured at different temperatures for $Mg_{0.2}Fe_{0.3}Cr_{1.5}O_3$ sample.

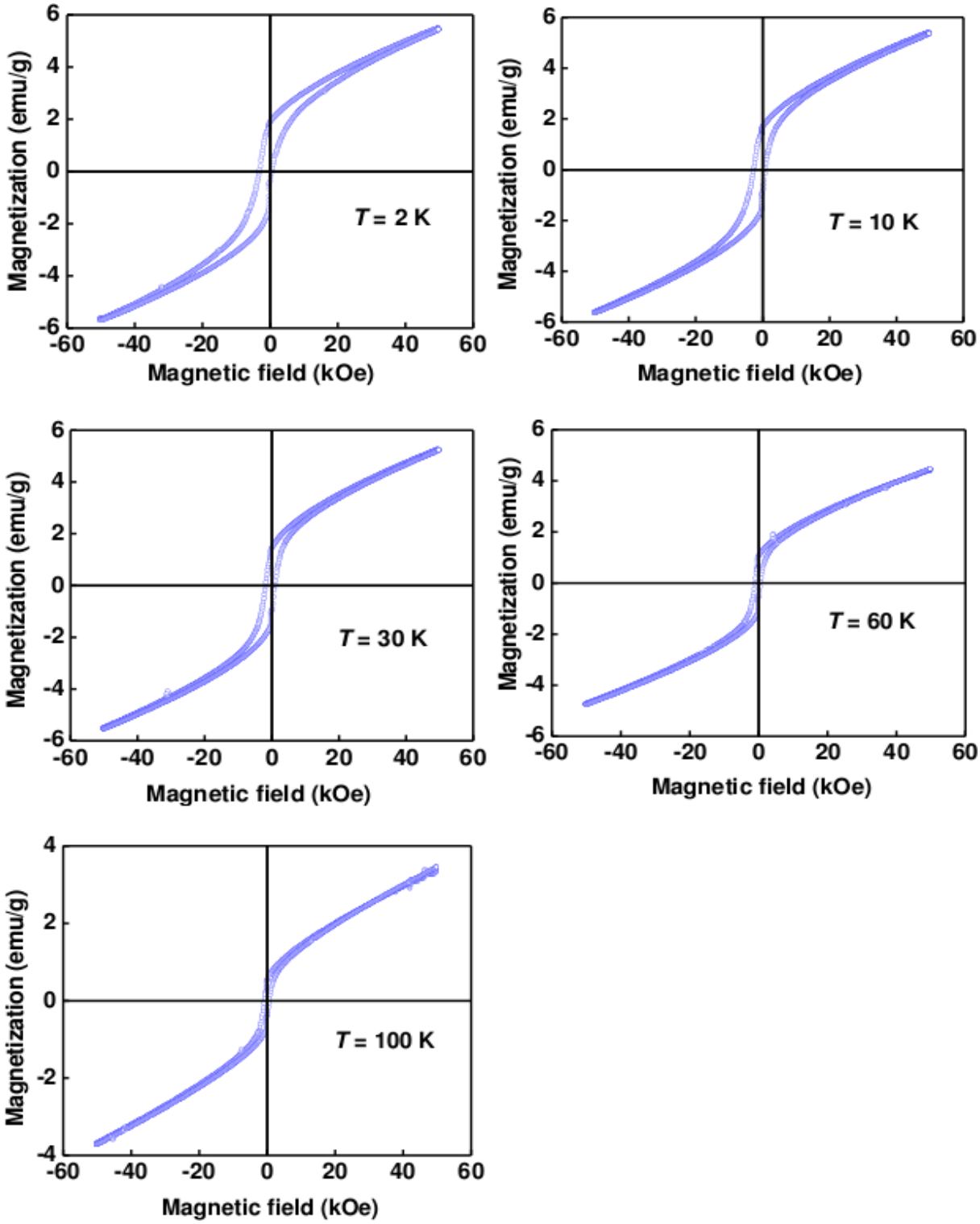

Figure 7.7: Hysteresis loops measured at different temperatures for $Mg_{0.2}Fe_{0.5}Cr_{1.3}O_3$ sample.

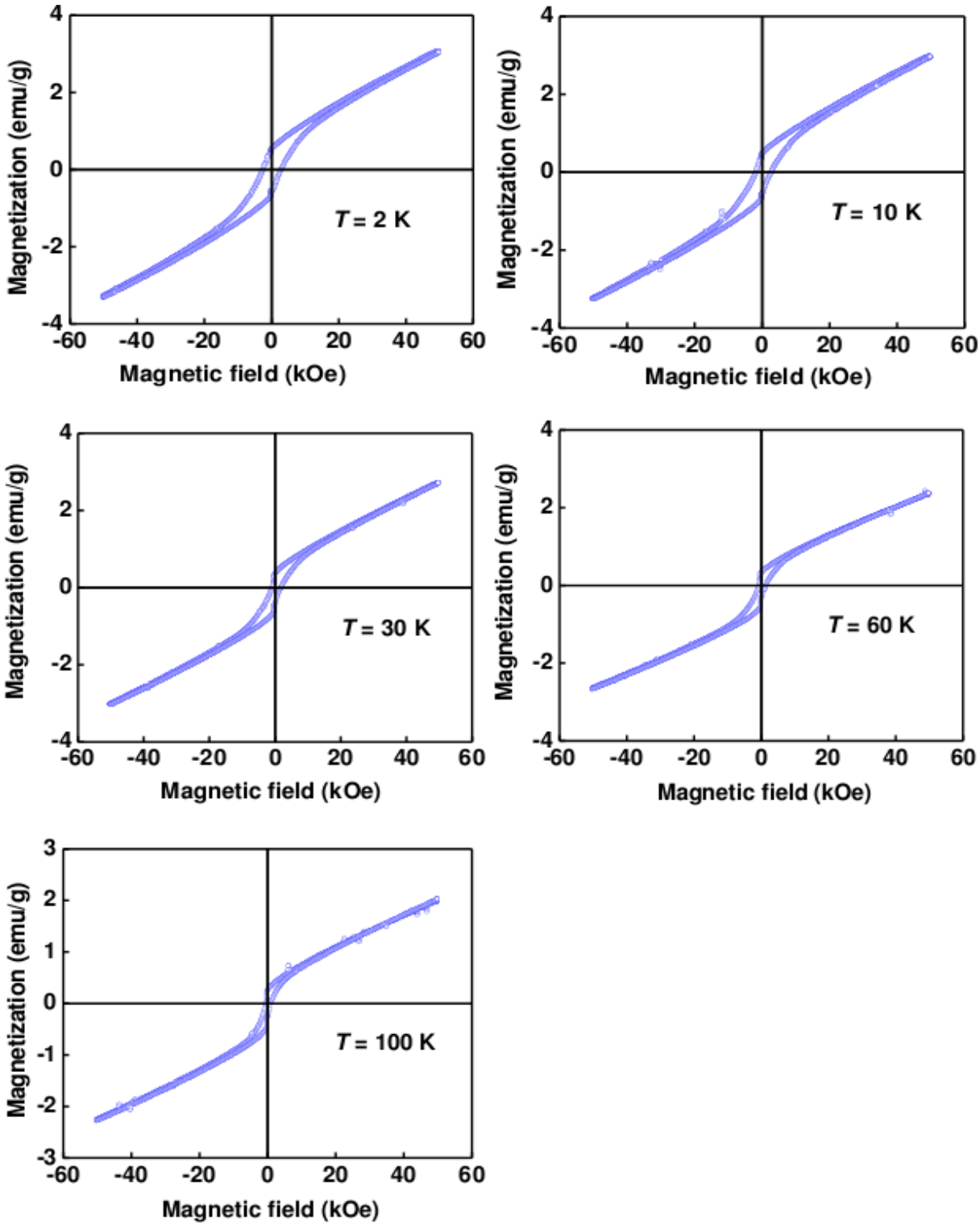

Figure 7.8: Hysteresis loops measured at different temperatures for $Mg_{0.2}Fe_{0.7}Cr_{1.1}O_3$ sample.

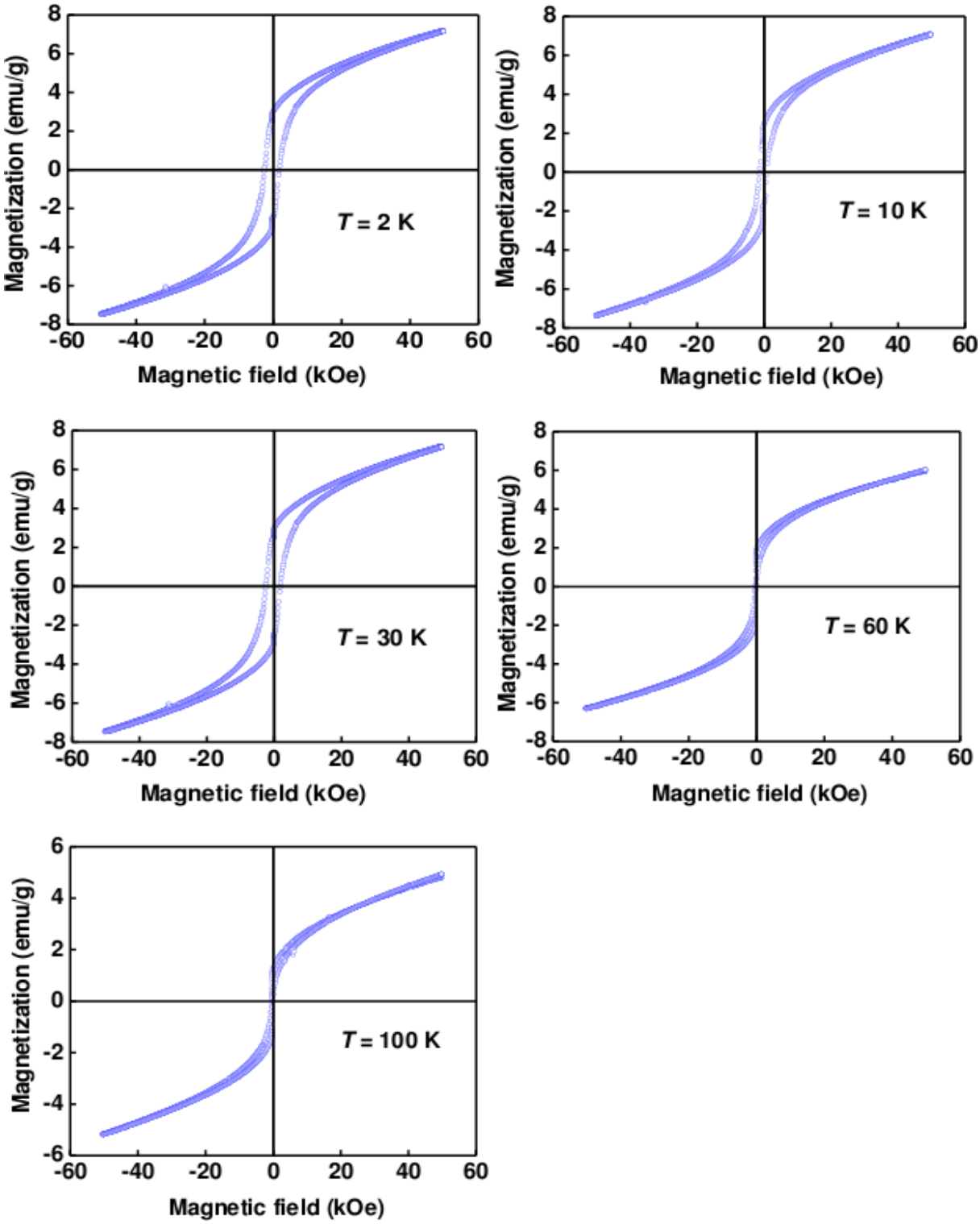

Figure 7.9: Hysteresis loops measured at different temperatures for $Mg_{0.2}Fe_{0.9}Cr_{0.9}O_3$ sample.

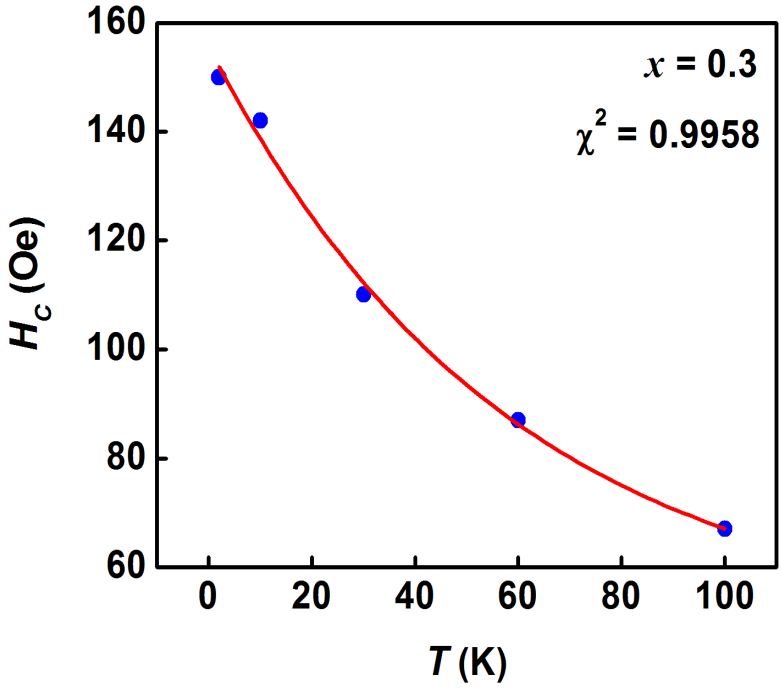

Figure 7.10: Temperature dependence of the coercive field for the as-annealed sample of $Mg_{0.2}Fe_{0.3}Cr_{1.5}O_3$, fitted by exponential functions.

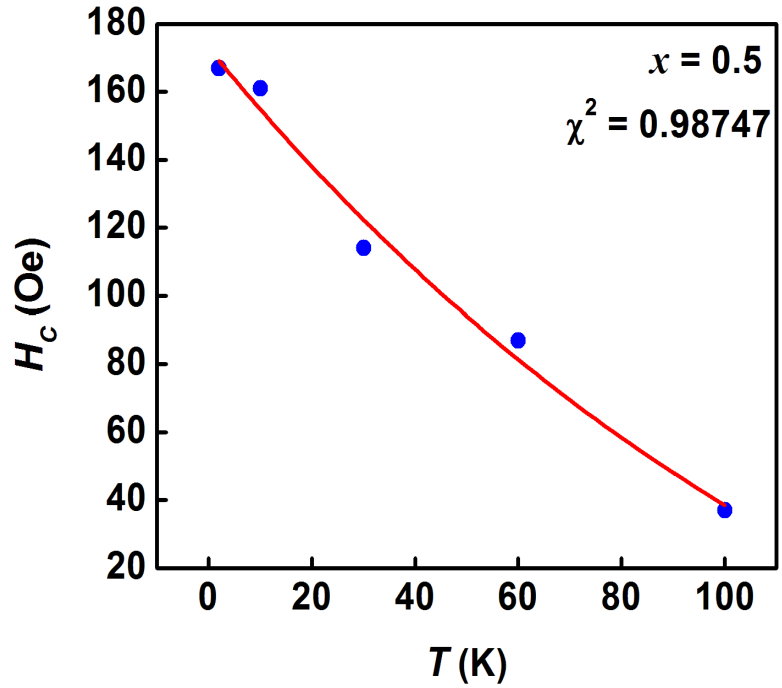

Figure 7.11: Temperature dependence of the coercive field for the as-annealed sample of $Mg_{0.2}Fe_{0.5}Cr_{1.3}O_3$, fitted by exponential functions.

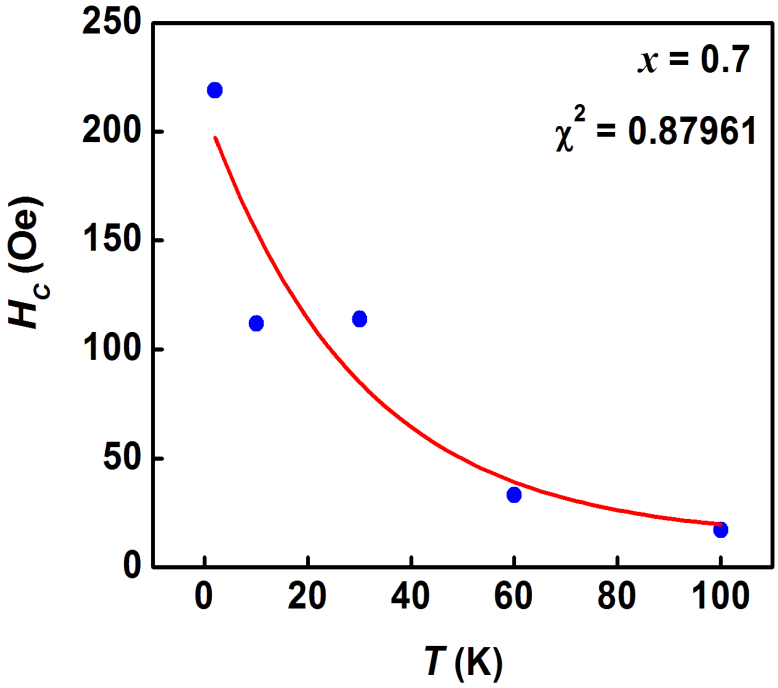

Figure 7.12: Temperature dependence of the coercive field for the as-annealed sample of $Mg_{0.2}Fe_{0.7}Cr_{1.1}O_3$, fitted by exponential functions.

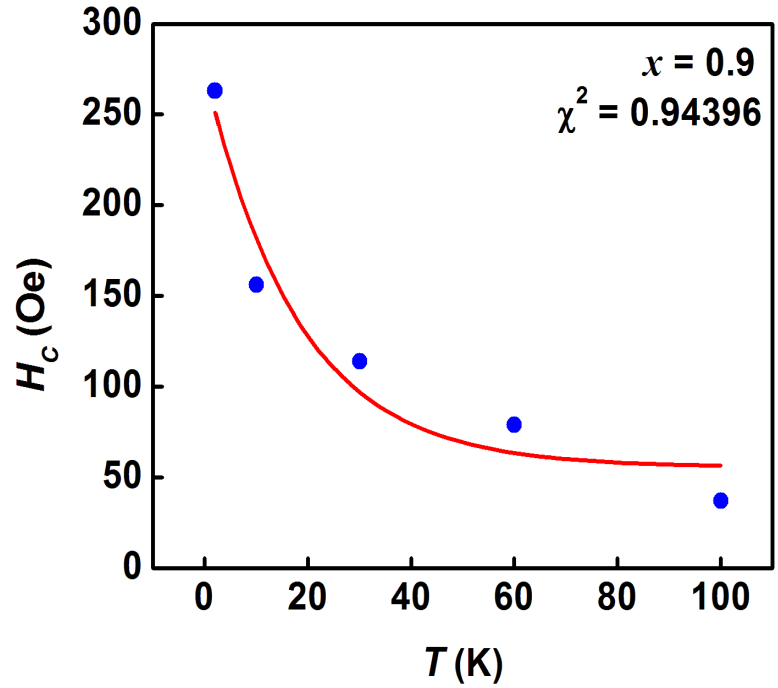

Figure 7.13: Temperature dependence of the coercive field for the as-annealed sample of $Mg_{0.2}Fe_{0.9}Cr_{0.9}O_3$, fitted by exponential functions.

Here again, we find that the hysteresis loops are shifted along the magnetic field axis, indicating the presence of exchange bias effects in the samples [149] in the temperature range between 2 and 20 K. The presence of the microscopic unidirectional exchange anisotropy interaction at the FM/AFM interface appears to be responsible for the exchange bias phenomena [151]. In order to verify whether the observed exchange bias like properties are associated with magnetic ordering, we studied the temperature dependence of the exchange bias. In these measurements, the samples were field-cooled to the measuring temperature in an applied field of 50 Oe. Once the measuring temperature was reached, the magnetization loops were measured between ± 50 kOe. The exchange bias fields deduced from the hysteresis loops at different temperatures are given in Table 7.3 and plotted as a function of temperature in Figure 7.14.

Significant exchange bias is observed at low temperatures for the samples annealed

Table 7.3: Values of exchange bias fields for $Mg_{0.2}Fe_xCr_{1.8-x}O_3$ samples annealed at 700 °C.

T (K)		2	4	10	20
x	D_{XRD} (nm) ± 0.04	H_{EB} (Oe) ± 0.5	H_{EB} (Oe) ± 0.5	H_{EB} (Oe) ± 0.5	H_{EB} (Oe) ± 0.5
0.3	56.45	67.0	94.21	6.4	4.2
0.5	44.01	105.2	120.0	74.0	5.1
0.7	66.55	35.2	74.1	55.2	3.2
0.9	34.01	10.2	8.2	3.2	2.1

at 700 °C. In the core/shell nanoparticle model, the core spin particles are expected to align while the shell spin particles are in randomized states due to the broken exchange bonds at the surfaces of the nanoparticles [98]. This allows the shell to freeze into random directions at the lowest temperatures. The exchange bias decreases with increase in temperature. The AFM order also diminishes due to thermal fluctuations which result in the weakening of interfacial interactions that causes reduction of loop shifts along the field direction. When the temperature approaches T_N, H_{EB} vanishes due to the disapperance of AFM order. It should be noted that though exchange bias

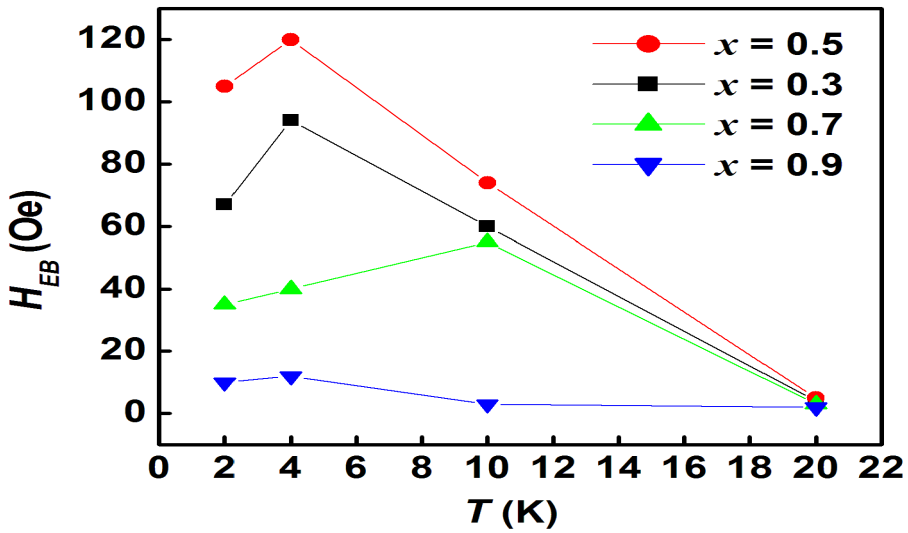

Figure 7.14: Exchange bias fields obtained at different temperatures for $Mg_{0.2}Fe_xCr_{1.8-x}O_3$ samples.

has been observed in some bulk materials, including several Heusler alloys, the effect is in most cases limited to low temperatures [151, 157]. In order to further investigate the correlation between the exchange bias and the particle sizes observed in chapter 6, we have measured hysteresis loops at 2 K, 4 K, 10 K and 20 K. Figure 7.15 shows the particle size dependence of H_{EB} for all our samples at the first three temperatures. Contrary to what was observed in Chapter 6, the exchange bias field H_{EB} increases with decreasing particle size D, reaches the maximum around 44 nm for $x = 0.5$ and then decreases until it reaches a critical value of about 33 nm when H_{EB} is zero. For the $Mg_{0.2}Fe_xCr_{1.8-x}O_3$ nano oxides, as the particle size decreases, more and more surface spins deviate from the AFM arrangement which implies the increasing proportion of the uncompensated spin shell and the reduction in the AFM core in the nano oxide [157]. At the same time the uncompensated surface spins favor the FM coupling, leading to the increase in FM clusters with reducing particle size. Thus, H_{EB} increases first and reaches its maximum, then decreases with decreasing particle size. Huang *et al.* [151] have reported similar results of H_{EB} measured at 5 K for $La_{0.25}Co_{0.75}MnO_3$ nanoparticles with D<100 nm.

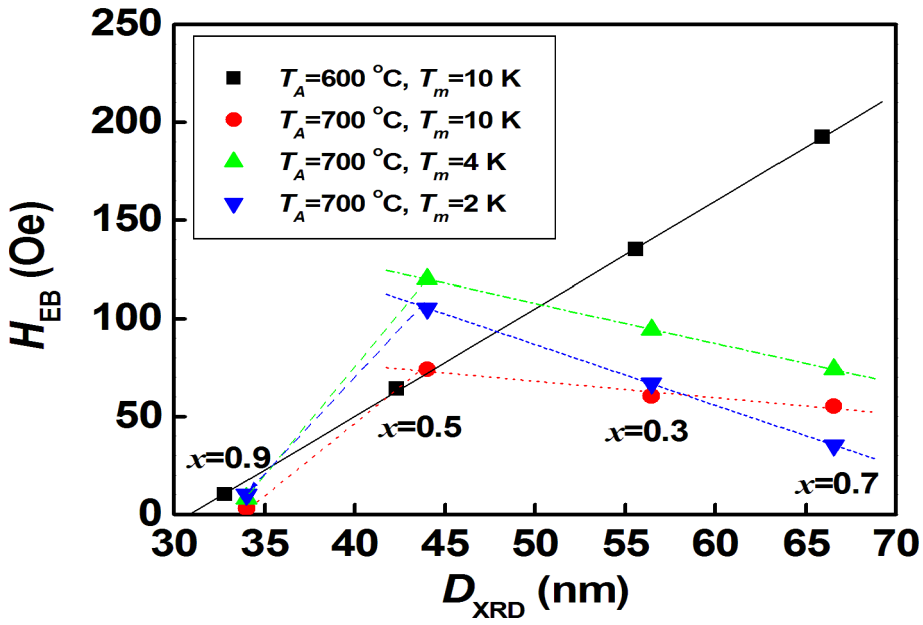

Figure 7.15: Particle size dependence of exchange bias field H_{EB} measured at T_m for $Mg_{0.2}Fe_xCr_{1.8-x}O_3$ samples annealed at T_A.

7.3.3 Conclusion

Nanoparticles of $Mg_{0.2}Fe_xCr_{1.8-x}O_3$ oxides with single phase corundum structure were synthesized directly by the hydrothermal method. A summary of the effects of annealing temperature T_A on the exchange bias effect are shown in Figure 7.15. As expected thermal annealing increases the particle sizes. The sample at $x = 0.5$ shows enhancement of H_{EB} after annealing while reduction of H_{EB} are observed for other samples. As observed in Figure 6.21 a strong correlation was observed between H_{EB} and D_{XRD}. After annealing only the sample at $x = 0.5$ introduces an extra data point that correlates with previous results measured at the same temperature $T_m = 10$ K. Our results show exponential temperature dependence of coercive field. Similar temperature dependences have been observed in other alloys such as $La_{1-x}CaMnO_3$ [151, 159] and Fe-rich Fe_xZr_{1-x} amorphous alloys [160]. However, there is still no conclusive evidence of the origin of such a temperature dependence. Coercive fields are related to the ease of inducing magnetization reversals due to the effects of pinning of magnetic domain

walls. One possible explanation of the exponential temperature dependence of H_C can involve a decrease in the volume fraction of AFM components with increase in temperature [151].

Chapter 8

Structure and magnetic properties of $Mn_{0.2}Fe_xCr_{1.8-x}O_3$ nano oxides

8.1 Introduction

In this chapter we present the structure and magnetic properties of $Mn_{0.2}Fe_xCr_{1.8-x}O_3$ nanosized alloys with x ranging from 0.3 to 1.3. The samples were synthesized at low reaction temperature of about 100 °C by using the hydrothermal method using a model 4843 stirred pressure reactor. We have managed to produce samples with particle sizes in the range between 14.2 and 32.8 nm. The structures and magnetic properties of the synthesized samples were investigated on the as-prepared samples annealed at 600 °C. The evolution of the properties as a function of composition was investigated by XRD, TEM, Mössbauer spectroscopy, magnetization and susceptibility measurements.

8.2 Experimental details

High-purity metal chlorides were used as starting materials to make 0.1 molar (M) solutions for hydrothermal reaction. The synthesis procedure is similar to what we have presented before [20, 21]. Excess aqueous ammonia was slowly added to the stochiometric chloride metal mixture until full precipitation. The precipitate was boiled under pressure in a reactor for 3 hours. The products were then filtered and washed

with deionized water over a Whatman micro-fibre filter (GF/F) several times until no chloride ions were detected by addition of drops of silver nitrate standard solution. The clean products were finally washed with ethanol and then dried under an infrared lamp. The resulting homogeneous powders were heated in air at 600 °C for 12 hours. The X-ray diffraction (XRD) patterns of the samples were obtained by using CoKα radiation (λ = 1.7903 Å) on a Philips diffractometer (type: PW 1710). The Mössbauer spectra were recorded at about 300 K using a conventional constant acceleration spectrometer with a ^{57}Co source sealed in Rh matrix. The magnetization measurements were performed using two different systems, namely a Lakeshore model 735 vibrating sample magnetometer (VSM) for room temperature measurements and a Quantum Design MPMS SQUID magnetometer for magnetization measurements in applied magnetic fields of up 50 kOe in the temperature range of 2 K to 400 K. These measurements included hysteresis loops, zero field cooling (ZFC) and field cooling (FC) magnetizations.

8.3 Results and discussion

8.3.1 X-ray diffraction

Figure 8.1 shows the XRD patterns for the $Mn_{0.2}Fe_xCr_{1.8-x}O_3$ alloys. The patterns confirm the formation of the basic corundum structure in all samples. Small impurities were observed in the patterns around 45°. These XRD results are similar to those of Sn doped α-Fe_2O_3 presented in Chapter 5 [66], [133] and which were interpreted in terms of tin occupying both octahedral interstitial and substitutional sites. It appears that in solid solutions of the type α-$(FeCr)_2O_3$ the manganese ion also occupies similar sites as does tin and magnesium. The refinement of XRD data was performed by Rietveld analysis (FullProfSuite for Windows) using a model involving a combination of both interstitial and substitutional Mn^{2+} ions in octahedral coordination [134]. The

complete set of final refined parameters are shown in Table 8.1. The average particle sizes were obtained using the Debye-Scherrer equation (4.2) [114]. Direct measurements of the particle sizes and powder morphology for the as-prepared samples were also performed by transmission electron microscope (TEM). The TEM pictures in Figure 8.2 show the presence of small particles. The lattice parameters, the average particle size as calculated from XRD data (D_{XRD}) and observed by TEM measurements (D_{TEM}) are recorded in Table 8.1. The general trend of D in Figure 8.3 for the different samples shows that the calculated D_{XRD} and measured D_{TEM} values of the particle sizes are in good agreement.

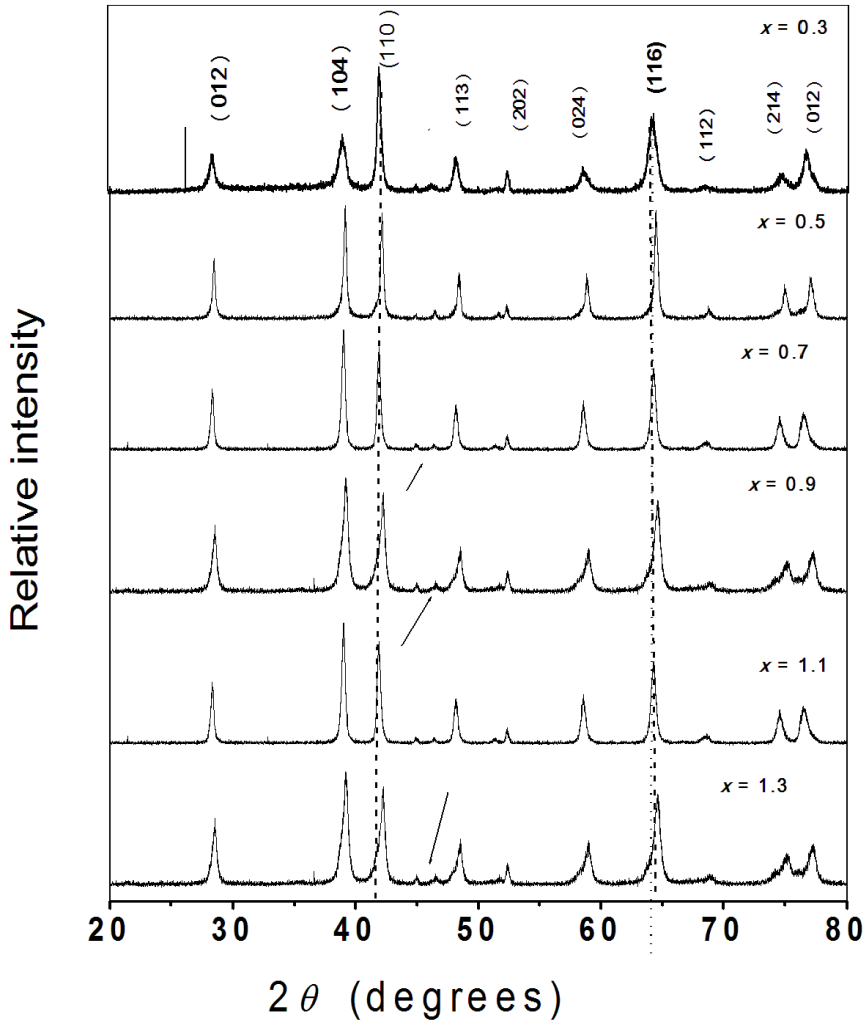

Figure 8.1: XRD patterns recorded for the as-prepared $Mn_{0.2}Fe_xCr_{1.8-x}O_3$ samples. The arrows indicate small impurities.

Table 8.1: Refined Structural Parameters for $Mn_{0.2}Fe_xCr_{1.8-x}O_3$ samples.

Atom	x/a	y/b	z/c	$U_{iso}\times 100/\AA^2$	Occupancy
			$Mn_{0.2}Fe_{0.3}Cr_{1.5}O_3$		
Cr1	0.00000	0.00000	0.34690(0)	0.500(0)	10.260(0)
Fe	0.00000	0.00000	0.34690(0)	0.500(0)	1.207(0)
Mn1	0.00000	0.00000	0.34690(0)	0.500(0)	0.270(0)
Mn2	0.00000	0.00000	0	0.000(0)	0.500(0)
O1	0.30800(0)	0.00000	0.2500(0)	0.500(0)	18.000(0)
			$Mn_{0.2}Fe_{0.5}Cr_{1.3}O_3$		
Cr1	0.00000	0.00000	0.34690(0)	0.500(0)	9.055(0)
Fe	0.00000	0	0.34690(0)	0.500(0)	2.415(0)
Mn1	0.00000	0.00000	0.34690(0)	0.500(0)	0.270(0)
Mn2	0.00000	0.00000	0.00000	0.000(0)	0.500(0)
O1	0.3217(1)	0.00000	0.250(0)	0.500(0)	18.000(2)
			$Mn_{0.2}Fe_{0.7}Cr_{1.1}O_3$		
Cr1	0.00000	0.00000	0.34690(0)	0.500(0)	10.260(0)
Fe	0.00000	0.00000	0.34690(0)	0.500(0)	1.207(0)
Mn1	0.00000	0.00000	0.34690(0)	0.500(0)	0.270(0)
Mn2	0.00000	0.00000	0	0.000(0)	0.500(0)
O1	0.30800(0)	0.00000	0.2500(0)	0.500(0)	18.000(0)
			$Mn_{0.2}Fe_{0.9}Cr_{0.9}O_3$		
Cr1	0.00000	0.00000	0.34690(0)	0.500(0)	10.260(0)
Fe	0.00000	0.00000	0.34690(0)	0.500(0)	1.207(0)
Mn1	0.00000	0.00000	0.34690(0)	0.500(0)	0.270(0)
Mn2	0.00000	0.00000	0	0.000(0)	0.500(0)
O1	0.30800(0)	0.00000	0.2500(0)	0.500(0)	18.000(0)
R_{wp} (%)	13.4		R_{exp} (%)	10.5	
			$Mn_{0.2}Fe_{1.1}Cr_{0.7}O_3$		
Cr1	0.00000	0.00000	0.34689(0)	0.500(0)	9.658(0)
Fe	0.00000	0.00000	0.34689(0)	0.500(0)	1.810(0)
Mn1	0.00000	0.00000	0.34689(0)	0.500(0)	0.269(0)
Mn2	0.00000	0.00000	0.00000	0.000(0)	0.500(0)
O1	0.3217(1)	0.00000	0.250(0)	0.500(0)	18.000(0)
R_{wp} (%)	12.4		R_{exp} (%)	7.5	
			$Mn_{0.2}Fe_{1.3}Cr_{0.5}O_3$		
Cr1	0.00000	0.00000	0.34689(0)	0.500(0)	9.658(0)
Fe	0.00000	0.00000	0.34689(0)	0.500(0)	1.810(0)
Mn1	0.00000	0.00000	0.34689(0)	0.500(0)	0.269(0)
Mn2	0.00000	0.00000	0.00000	0.000(0)	0.500(0)
O1	0.3217(1)	0.00000	0.250(0)	0.500(0)	18.000(0)
R_{wp} (%)	12.4		R_{exp} (%)	7.5	

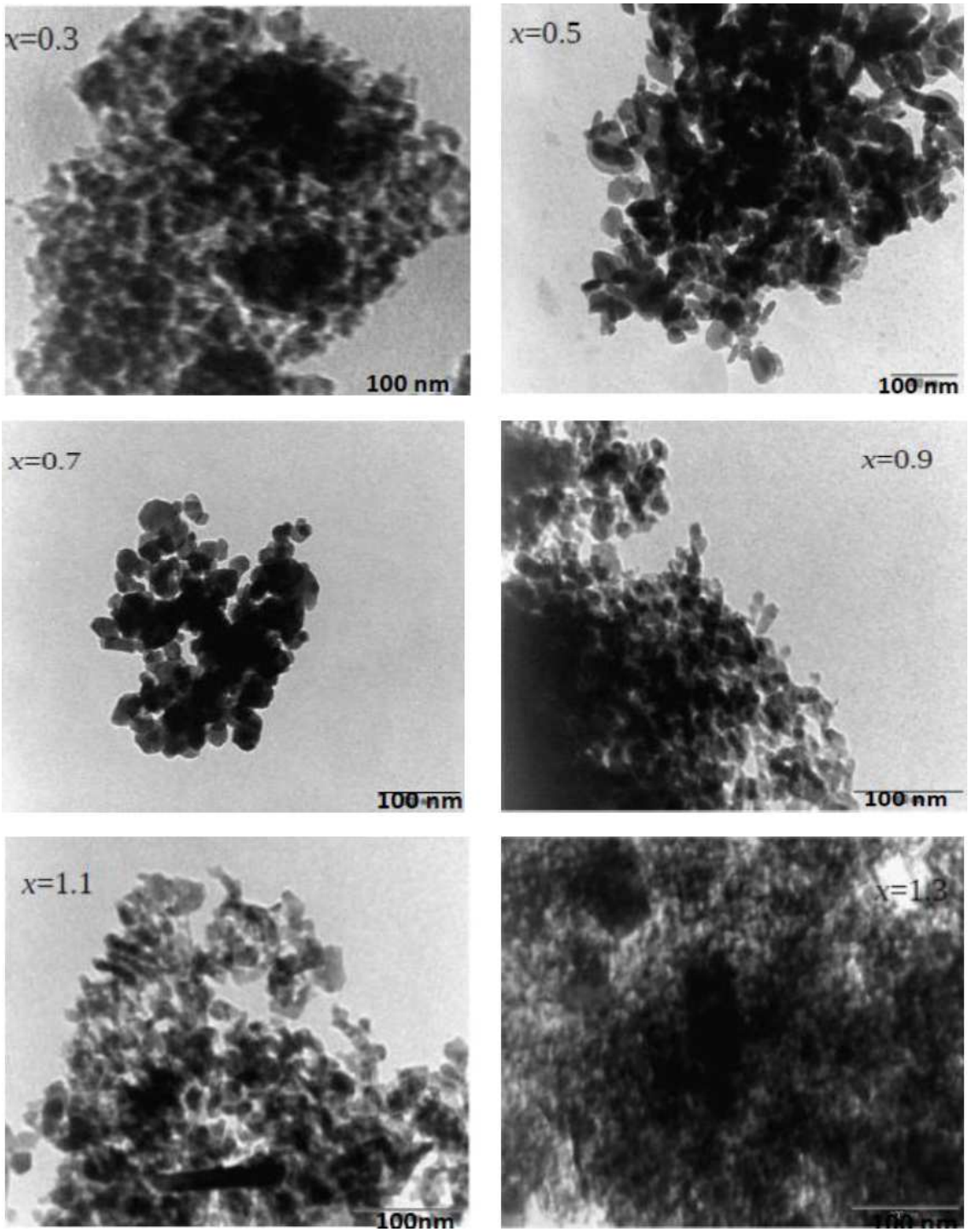

Figure 8.2: TEM micrographs for the as-prepared $Mn_{0.2}Fe_xCr_{1.8-x}O_3$ samples.

Table 8.2: Particle size (D_{XRD}) and lattice parameters for $Mn_{0.2}Fe_xCr_{1.8-x}O_3$ samples.

x	$a = b$ (Å) $\pm 10^{-3}$	c (Å) $\pm 10^{-3}$	V ($Å^3$) $\pm 10^{-3}$	D_{XRD} (nm) ± 0.6	D_{TEM} (nm) ± 2
0.3	4.989	13.699	290.40	32.8	31
0.5	4.986	13.632	288.76	28.9	27
0.7	5.004	13.646	287.34	26.8	26
0.9	4.976	13.608	286.53	17.5	18
1.1	4.989	13.778	283.32	15.3	15
1.3	5.024	13.768	283.12	14.20	14

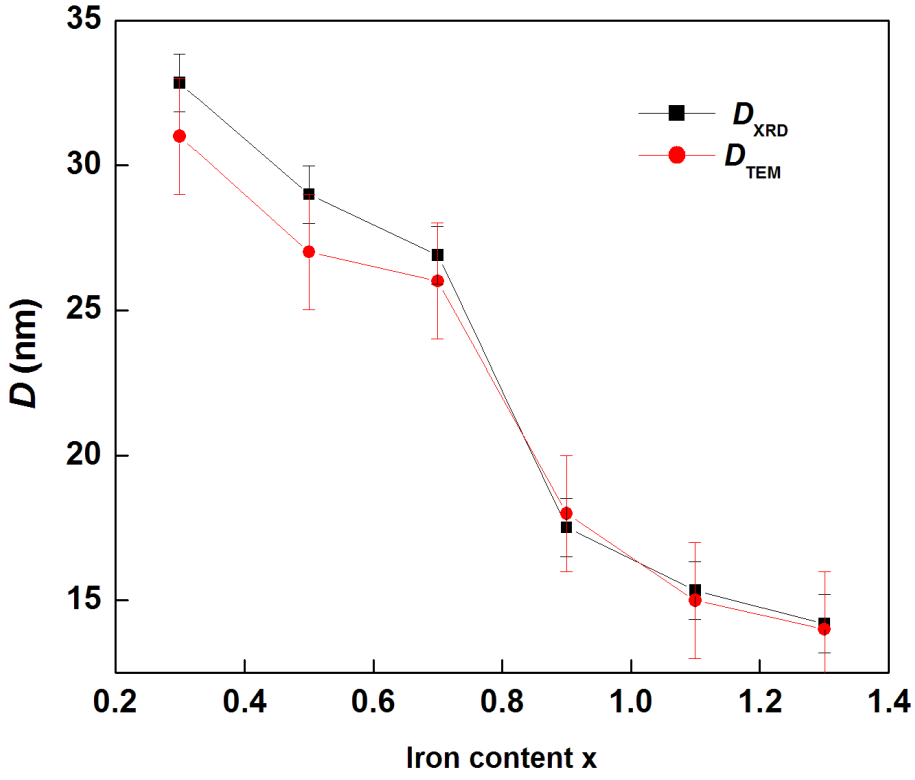

Figure 8.3: Variation of particle size with iron content for the as-prepared samples of $Mn_{0.2}Fe_xCr_{1.8-x}O_3$.

8.3.2 Mössbauer measurements

The ^{57}Fe Mössbauer spectra recorded for $Mn_{0.2}Fe_xCr_{1.8-x}O_3$ samples at 300 K are shown in Figure 8.4. It can been seen that the spectra for $x = 0.3$ and $x = 0.5$ are paramagnetic doublets and were best fitted to two doublets. The spectrum for $x = 0.7$ shows a doublet with a weak sextet pattern, and for $x \geq 0.9$ sextets are being formed. The spectra for Fe content $x = 0.7$, 0.9 and 0.11 were best fitted to one doublet and one sextet while the spectra recorded for $x = 1.3$ were best fitted by the superposition of two sextets. The component with a larger hyperfine magnetic field can be associated with the Fe^{3+} ions without Mn^{2+} ions in nearby lattice sites whereas the component with lower hyperfine magnetic field reflects the lower spin density at Fe^{3+} in the vicinity of Mn^{2+} nearest cation neighbors. The solid lines are the fits to the experimental data and correspond to individual components (sextets or doublets). The doublet was required in the fits of the samples x =03 and 0.5 which we associate with Fe ions in the paramagnetic states. The Mössbauer spectra of $x = 0.7$ and 0.9 have been fitted with two magnetic components in the form of one sextet and onde doublet while the spectra of $x = 1.1$ and 1.3 were fitted with two sextets. The sextet with the higher hyperfine field is attributed to Fe^{3+} ions without Cr^{3+} or Mn^{2+} in their neigborhood lattice sites. The second sextet with lower hyperfine field is due to Fe^{3+} ions with Cr^{3+} and Mn^{4+} neighboors. This interpretation of hyperfine fields is similar to the work of Berry *et al* [133] in Sn and Ti doped α-Fe_2O_3 samples. The doublets are observed in samples that have higher Cr content. This reflects the collapse of magnetic interaction with increase Cr content associated with more negative exchange interactions leading to doublets. All the components in the spectra recorded at 300 K were characterized by a nearly constant chemical isomer shift of 0.32(3) mm/s confirming that the accommodation of manganese into the corrundum-related structure did not induce a change in the Fe^{3+} oxidation state [110]. Insignificant change in isomer shifts indicates that the s-electron

density is not much affected by substitution of Cr by Fe atoms or by thermal relaxation of the lattice. The Mössbauer parameter fits are presented in Table 8.2. The results confirm that manganese can also be accommodated in the corundum-related structure without inducing a change in the Fe^{3+} oxidation state as demonstrated before for tin-doped samples [20].

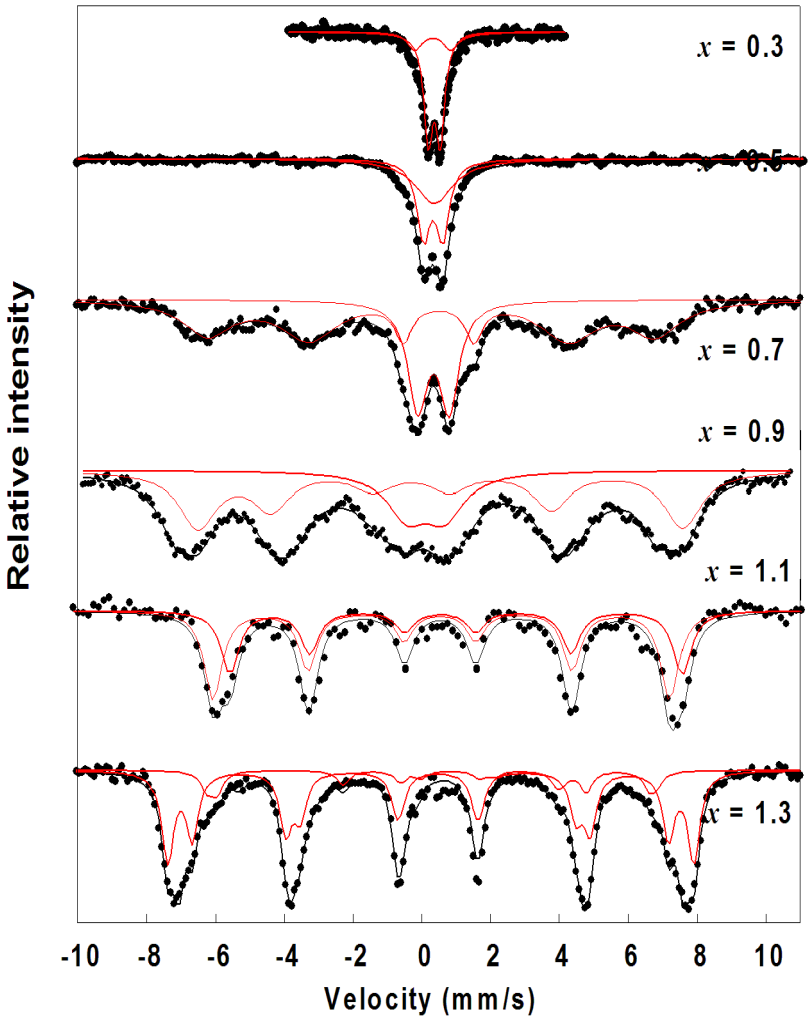

Figure 8.4: Room temperature ^{57}Fe Mössbauer spectra for the as-prepared $Mn_{0.2}Fe_xCr_{1.8-x}O_3$ samples. The solids lines are LSQ fits.

Table 8.3: Hyperfine parameters from Mössbauer spectra recorded at room temperature for the as-prepared samples of $Mn_{0.2}Fe_xCr_{1.8-x}O_3$. The solid line is the LSQ fits.

T = 300 K	doublet 1			doublet 2			sextet 1				sextet 2			
	δ	Δ	f	δ	Δ	f	δ	2ε	H	f	δ	2ε	H	f
Sample	mm/s	mm/s	%	mm/s	mm/s	%	mm/s	mm/s	kOe	%	mm/s	mm/s	kOe	%
x	± 0.01	± 0.02		± 0.01	± 0.02		± 0.01	± 0.02	± 3		± 0.01	± 0.02	± 3	
Reflux														
0.3	0.36	0.38	70	0.33	1.07	30								
0.5	0.31	1.08	39	0.37	0.49	61								
0.7	0.34	0.9	32				0.36	-0.09	404	68				
0.9	0.32	0.37					0.34	-0.08	423	58				
1.1							0.32	-0.12	432	47	0.34	-0.09	473	53
1.3							0.35	-0.14	491	20	0.37	-0.12	494	80

8.3.3 Magnetization measurements

Field cooling (FC) and zero field cooling (ZFC) magnetizations as a function of temperature for samples with x = 0.7, 0.9, 1.1, 1.3 are shown in Figures 8.5 - 8.8. The lower curve for each sample corresponds to ZFC and the upper curve to FC. In ZFC, a sample is cooled in zero field from room temperature to the lowest temperature at about 10 K where a measuring field is applied. The sample is cooled and the magnetization recorded in the same measuring field for FC. The magnetization measurements were performed with increasing temperature from 10 K to about 400 K in an external magnetic field of 50 Oe. The magnetization for the FC curves decrease continuously with increasing temperature. ZFC and FC magnetizations coincide at a spin freezing temperature which depends on the applied field. ZFC magnetization curves increase gradually with increasing temperature and reach maximum values at blocking temperatures. The width of the peak in the ZFC curve is associated with particle size distribution [161]. The slow decrease of the magnetization with further increase in temperature is associated with disordering of particle spins. One of the characteristic features of the plots in Figures 8.5 - 8.8 are reduced magnetizations at lower temperature for ZFC samples. Similar behaviour of FC and ZFC magnetizations have been

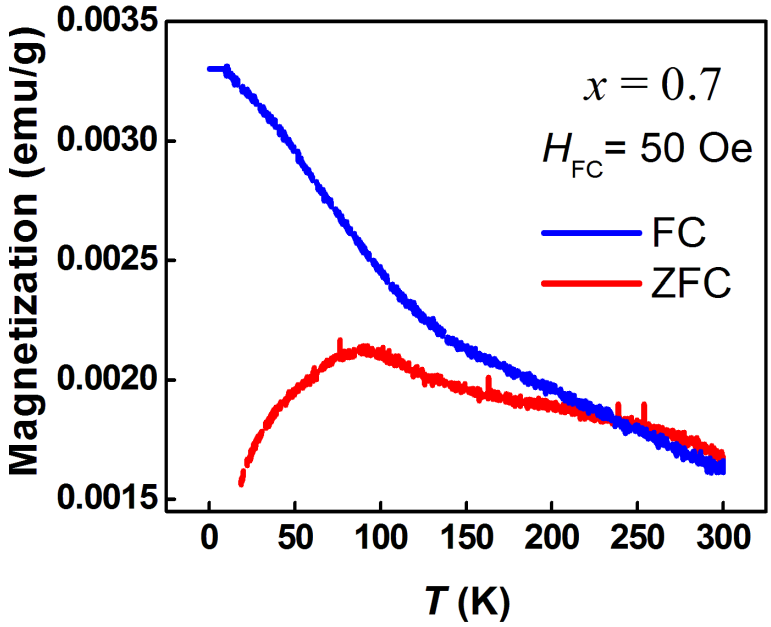

Figure 8.5: Temperature dependence of ZFC and FC magnetizations for the as-prepared $Mn_{0.2}Fe_{0.7}Cr_{1.1}O_3$.

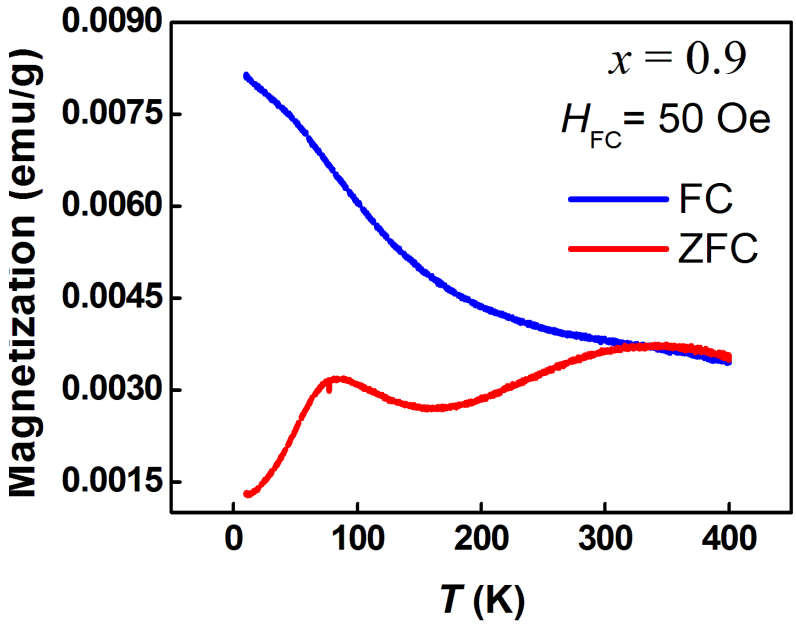

Figure 8.6: Temperature dependence of ZFC and FC magnetizations for the as-prepared $Mn_{0.2}Fe_{0.9}Cr_{0.9}O_3$.

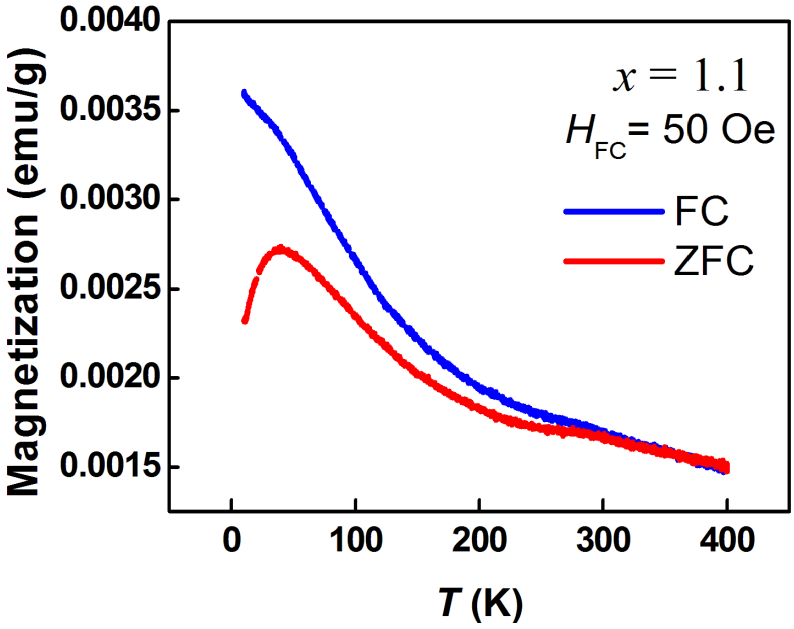

Figure 8.7: Temperature dependence of ZFC and FC magnetizations for the as-prepared $Mn_{0.2}Fe_{1.1}Cr_{0.7}O_3$.

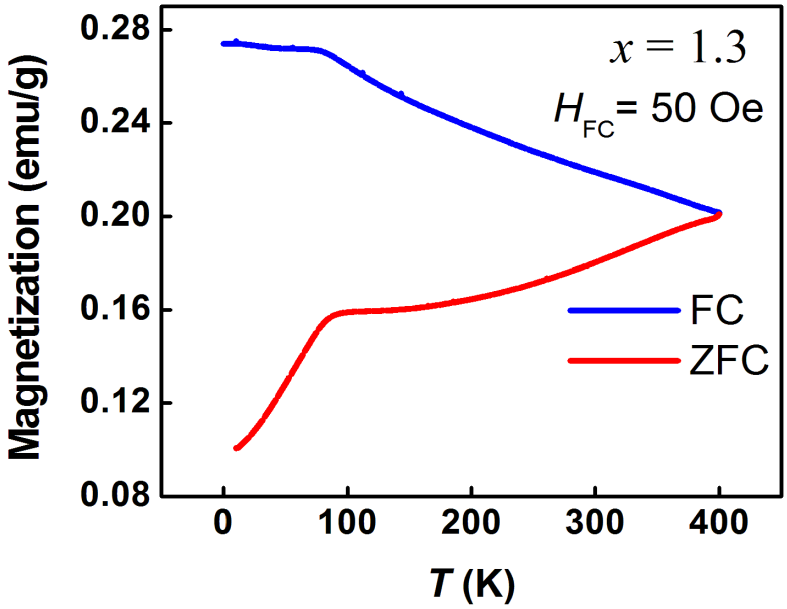

Figure 8.8: Temperature dependence of ZFC and FC magnetizations for the as-prepared $Mn_{0.2}Fe_{1.3}Cr_{0.5}O_3$.

considered to be spin-glass like behavior [162]. The ZFC curve for $x = 0.9$ shows a maximum in the magnetization at 82 K. Beyond this the magnetization reduces up to about 180 K before it further increases, touching the FC magnetization curve at about 330 K. This type of a double peak structure has been observed elsewhere [163] and was attributed to the bimodal distribution in particle size. At a lower temperature T_B called the blocking temperature, the ZFC magnetization reaches a maximum where the moments of the FM clusters begin to freeze. The blocking temperature depends on the average particle size [128, 144]. Figure 8.9 shows the linear fit to the temperature dependence of the inverse magnetization for $x = 0.9$. This sample clearly exhibits a Curie-Weiss type behavior above 200 K as indicated by the linear fit. The slope of the graph is 0.2 that gives a Curie constant $C = 5$. The value of the effective magnetization is found using the formula: $\mu_{eff} = 2.84\ C^{1/2} = 6.35\ \mu_B$. The value obtained is lower compared to the theoretical value which is 9.95 μ_B. This can be explained by the fact that in fitting the curve, we only considered the part that is linear. The corresponding

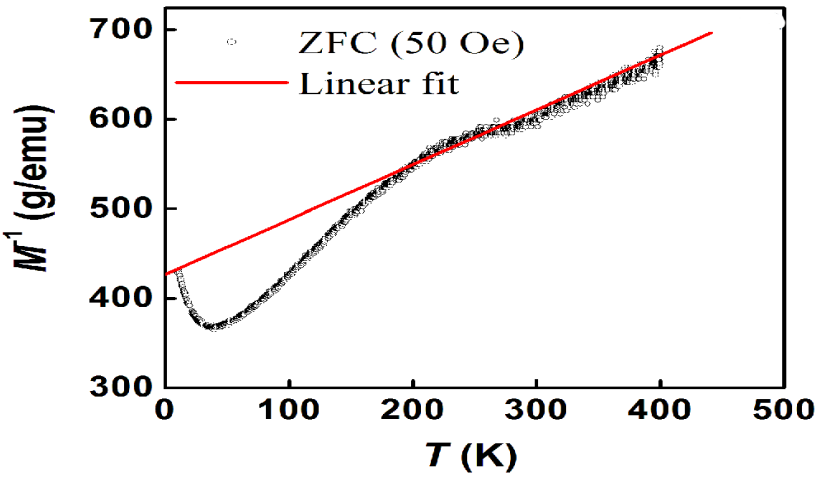

Figure 8.9: Linear fit for the temperature dependence of the inverse magnetization for the $Mn_{0.2}Fe_{0.9}Cr_{0.9}O_3$ samples. The red line is the linear fit.

extrapolated paramagnetic Weiss temperature θ_p is -175 K.

The value of θ_p shows that the antiferromagnetic interactions (AFM) are weaker in $Mn_{0.2}Fe_{0.9}Cr_{0.9}O_3$ compared to $Mg_{0.2}Fe_{0.9}Cr_{0.9}O_3$ where θ_p was -722 K [20].

The isothermal magnetization measurements presented here were performed at room temperature on a Lakeshore vibrating sample magnetometer [124]. Hysteresis loops of the samples in powder forms were obtained in an external applied field of up to ± 14 kOe. The magnetization measurements at room temperature obtained from $Mn_{0.2}Fe_xCr_{1.8-x}O_3$ samples are presented in Figure 8.10. We find lower magnetizations compared to what was observed in Chapter 5 for $Sn_{0.2}Fe_xCr_{1.8-x}O_3$ samples. The hysteresis loops for all samples appear to consist of a paramagnetic phase where the *M-H* plots are linear and a magnetically ordered phase at low fields associated with hysteresis. The magnetization increases rapidly in fields up to about 3 kOe and then vary almost linearly without reaching any saturation to a field of 14 kOe. This typical weak magnetic response confirms the antiferromagnetic interactions in the samples. This is similar to the main antiferromagnetic interactions in hematite particles responsible of a large magnetic susceptibility in high fields which is superimposed on a spontaneous ferromagnetic moment, coming either from weak ferromagnetism for temperatures above the Morin transition, or from uncompensated moments mainly at the surface of the particles [146]. Evidence of displacement of hysteresis loops are also observed in Figure 8.10. Assymmetric magnetic hysteresis loops exhibiting shifts both in the field and magnetization axis as well as an enhanced coercive field are observed which indicate the existence of exchange bias phenomenon. The vertical and horizontal loop shifts features are due to minor loop effect which means effects that appear when the FC loops are recorded without reaching saturation magnetization regime. The exchange bias effect can be explained on the basis of a phenomenological core-shell model where the core shows AFM behavior and the surrounding shell possesses a net magnetic moment due to a large number of uncompensated surface spins [98, 164]. The variation of the exchange bias H_{EB} with particle size D and iron content x are displayed in Figure 8.11 and Figure 8.12. The values of the exchange bias fields are recorded in Table 8.3.

Table 8.4: Values of exchange bias fields for as-prepared $Mn_{0.2}Fe_xCr_{1.8-x}O_3$ samples measured at room temperature.

x	D (nm) ± 0.1	H_{EB} (Oe) ± 0.5
0.3	31.3	57.1
0.5	27.8	86.2
0.7	26.2	157.3
0.9	18.1	257.1
1.1	15.3	324.2
1.3	13.8	362.6

The exchange bias field increases as the particle size decreases with increased Fe content x. The loops shifts are different with different particle sizes suggesting that the materials at room temperature may be superparamagnetic. Strong correlations are also observed between the exchange bias H_{EB} with particle size D (Figure 8.11) and with Fe content x (Figure 8.12). The linear correlation between H_{EB} and D is particularly interesting. It suggests a collapse of H_{EB} to zero at a particle size of about 33 nm. This is a similar value as for the H_{EB} versus D curve for Mg-doped samples [21] for hysteresis loops at 10 K. The main difference in this case is that H_{EB} decreases with increase in D. In order to investigate the phenomenon of exchange bias further, we measured isothermal magnetization loops at different temperatures. In Figure 8.13 we present the hysteresis loops for the as-prepared $Mn_{0.2}Fe_{1.3}Cr_{0.5}O_3$ sample measured at 2, 10, 30, 50, 100, 150 and 200 K in applied magnetic fields of up to 50 kOe using a Mini cryogen free magnetization measurement system (Figure 4.9). We observe that the exchange bias decreases at lower temperatures. This is in contrast to what was observed in Chapter 6 for $Mg_{0.2}Fe_xCr_{1.8-x}O_3$ nanoparticles and in other literature reports relating to Ni/NiO particles with an average particle size below 30 nm which demonstrated an asymmetrical magnetic hysteresis loop only at low temperatures [165].

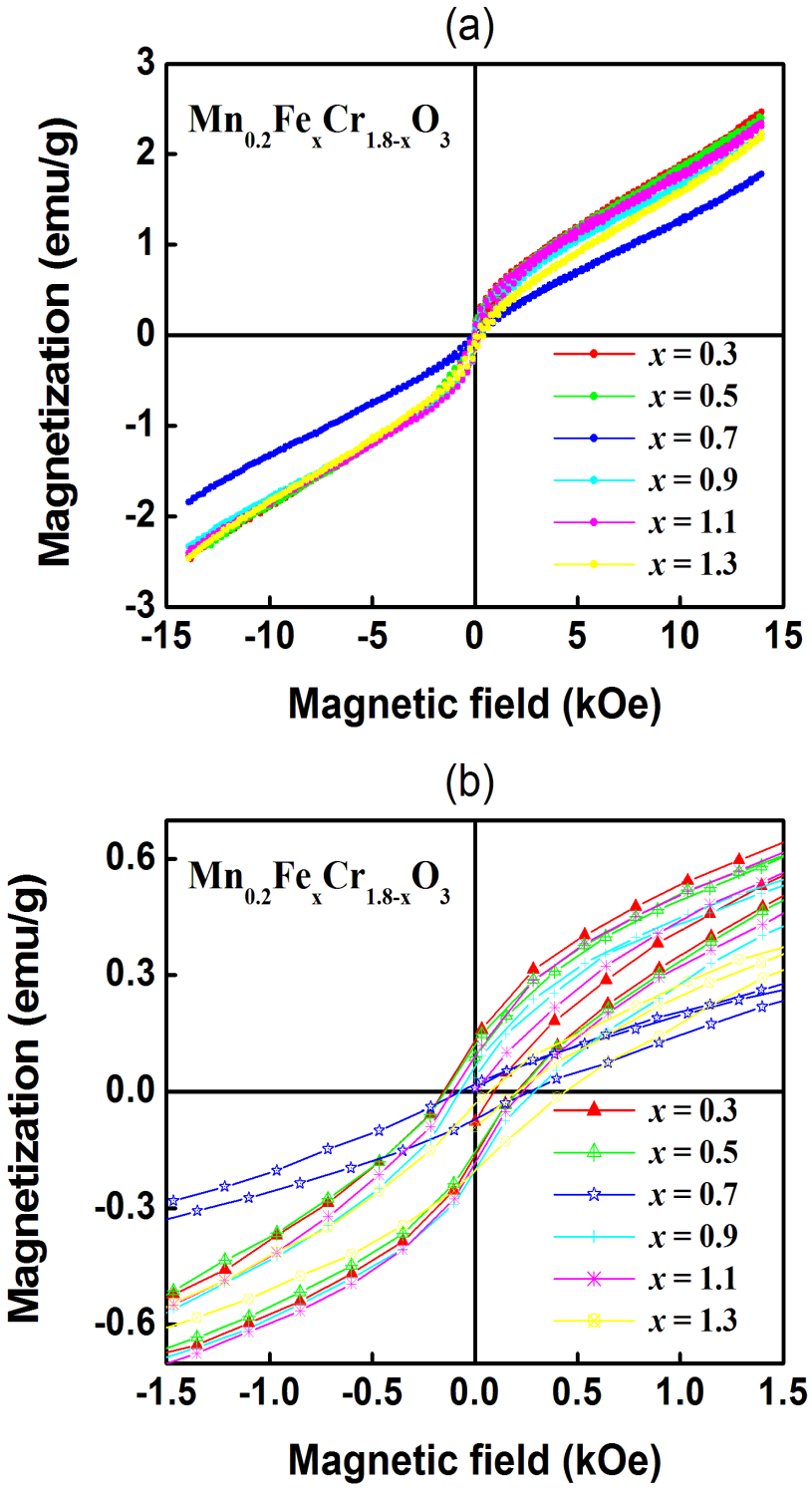

Figure 8.10: (a) Hysteresis loops measured at room temperature for $Mn_{0.2}Fe_xCr_{1.8-x}O_3$ in a reflux. (b) Magnified view of hysteresis loops at low fields.

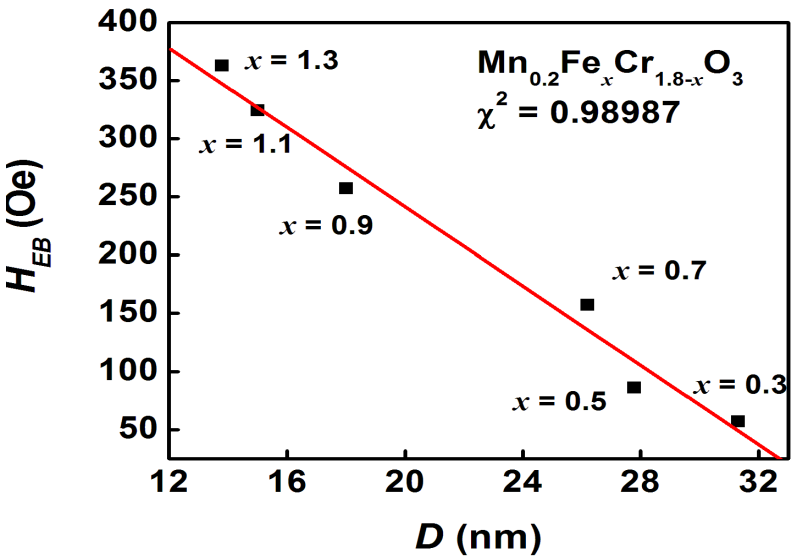

Figure 8.11: Particle size dependence of exchange bias field H_{EB} for the as-prepared $Mn_{0.2}Cr_{1.8-x}Fe_xO_3$ samples measured at room temperature. The red line is the linear fit.

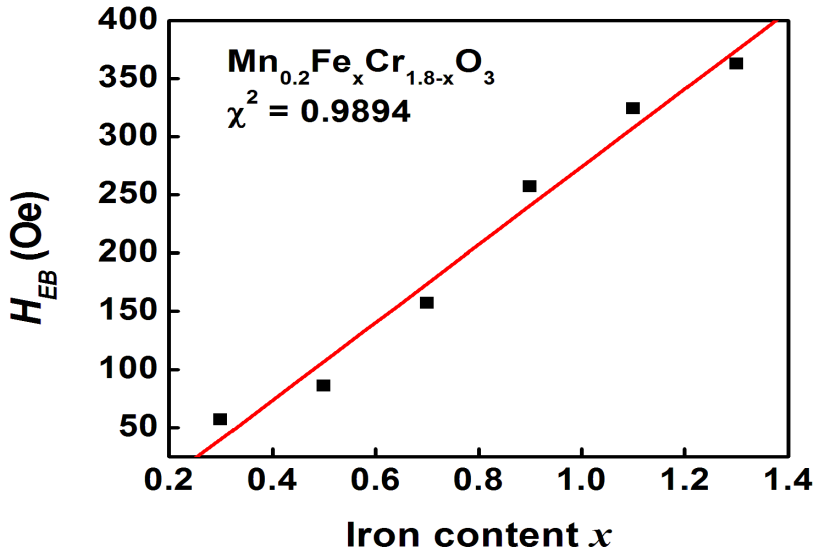

Figure 8.12: Iron content dependence of exchange bias field H_{EB} for the as-prepared $Mn_{0.2}Fe_xCr_{1.8-x}O_3$ samples measured at room temperature. The red line is the linear fit.

The shift observed may suggest the existence of spin-glass configurations. In magnetic oxide nanoparticles [146, 166], such configurations possess different structure and magnetic order between the surface and the interior of the nanoparticles. In this case the disfigurement and small cavities of nanoparticles which cause surface spin disorder or canting may be expected to be responsible for the loop shift of the superparamagnetic nanomaterials. The temperature dependence of the exchange bias for the $Mn_{0.2}Fe_{1.3}Cr_{0.5}O_3$ sample is shown in Figure 8.14. Hysteresis loops of the as-prepared samples of $Mn_{0.2}Fe_xCr_{1.8-x}O_3$ with $x = 0.7$, 0.9, 1.1 and 1.3 recorded at 2 K are shown in Figures 8.15 - 8.20.

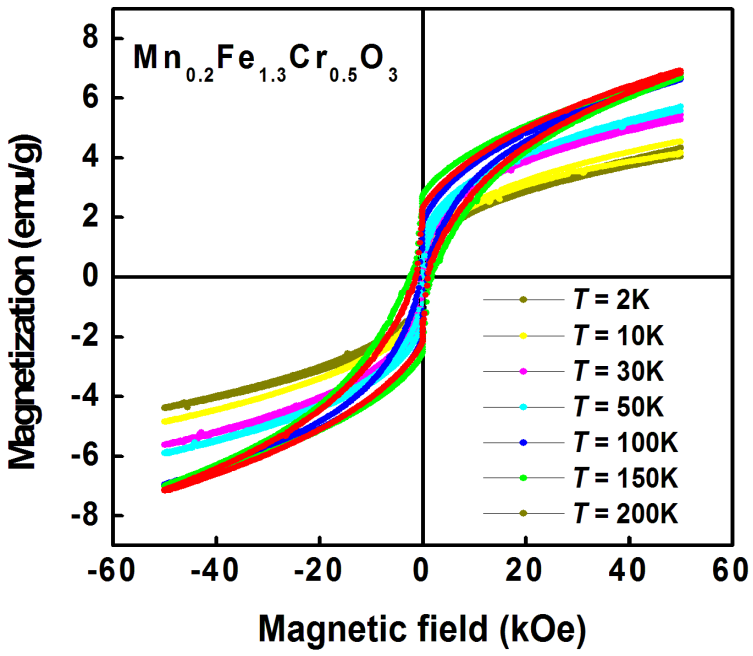

Figure 8.13: Hysteresis loops for the as-prepared sample of $Mn_{0.2}Fe_{1.3}Cr_{0.5}O_3$ recorded at different isothermal temperatures.

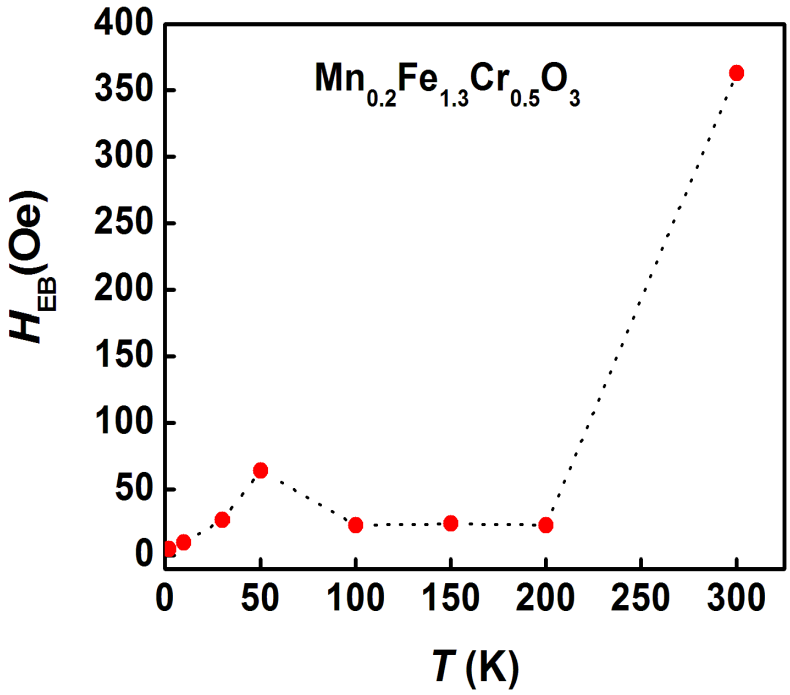

Figure 8.14: Temperature dependence of the exchange bias field for the as-prepared sample of $Mn_{0.2}Fe_{1.3}Cr_{0.5}O_3$.

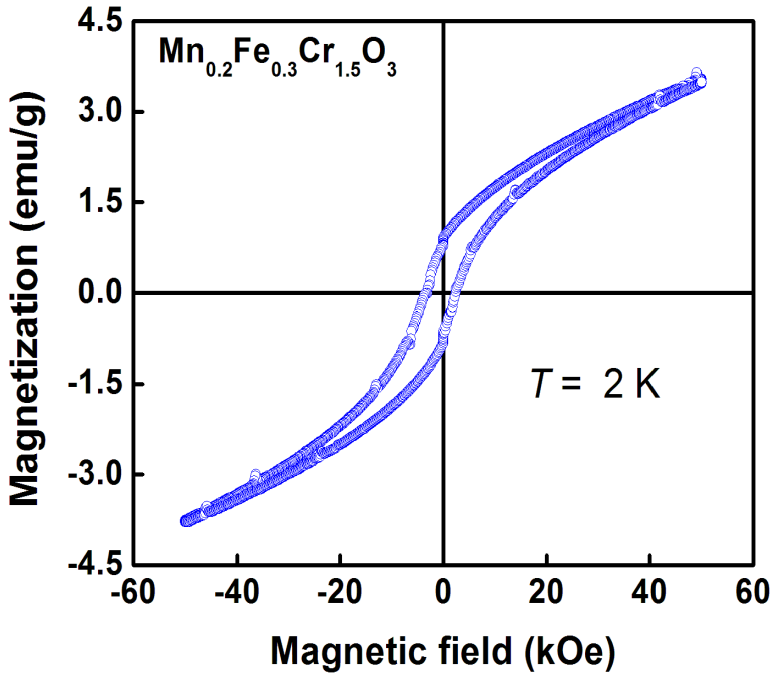

Figure 8.15: Hysteresis loops of $Mn_{0.2}Fe_{0.3}Cr_{1.5}O_3$ measured at 2 K.

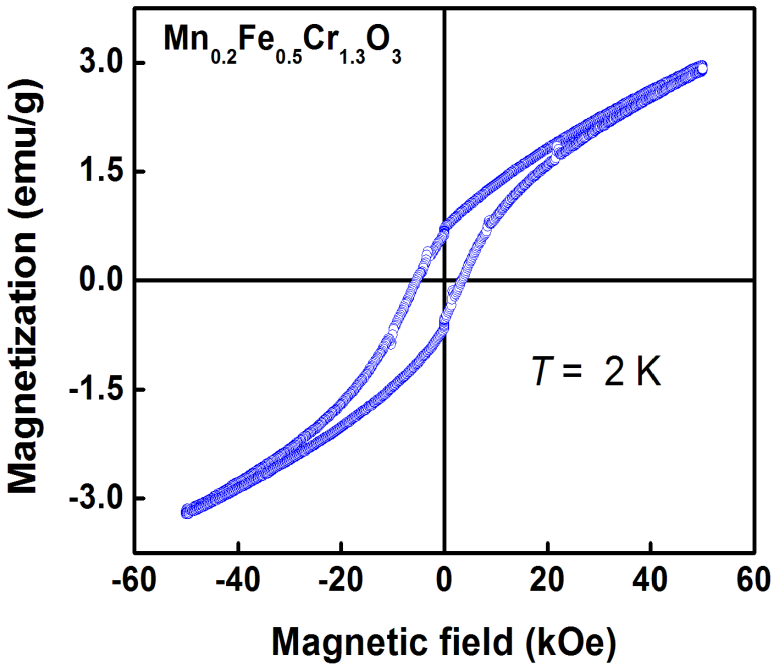

Figure 8.16: Hysteresis loops of $Mn_{0.2}Fe_{0.5}Cr_{1.3}O_3$ measured at 2 K.

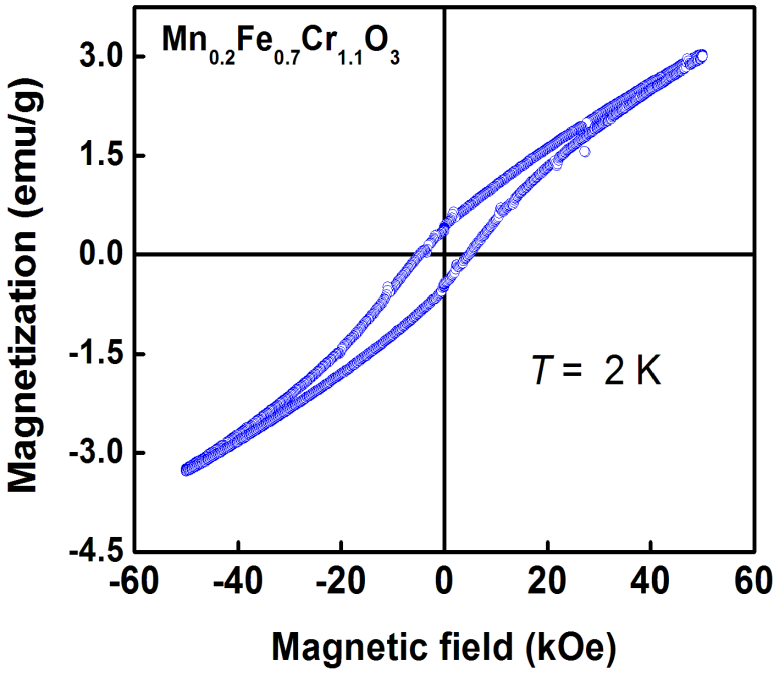

Figure 8.17: Hysteresis loops of $Mn_{0.2}Fe_{0.7}Cr_{1.1}O_3$ measured at 2 K.

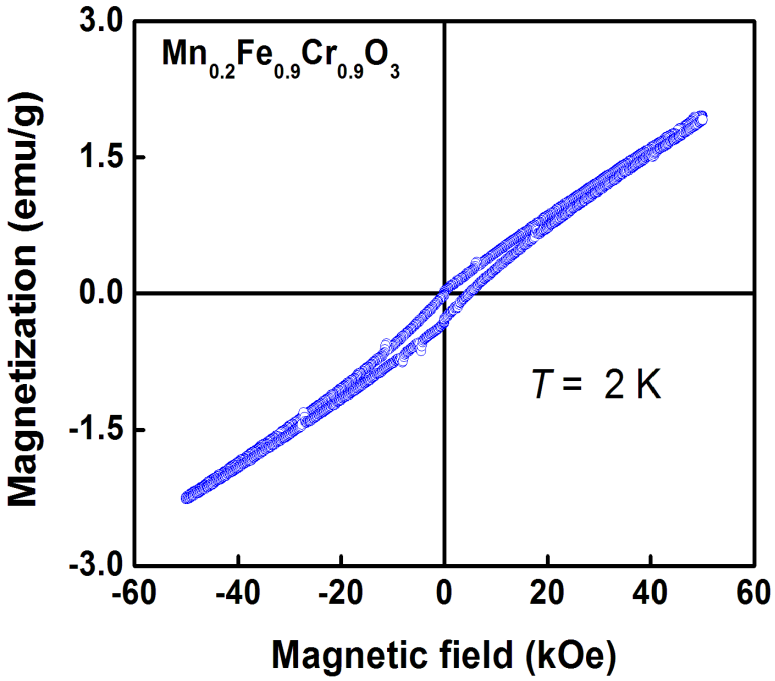

Figure 8.18: Hysteresis loops of $Mn_{0.2}Fe_{0.9}Cr_{0.9}O_3$ measured at 2 K.

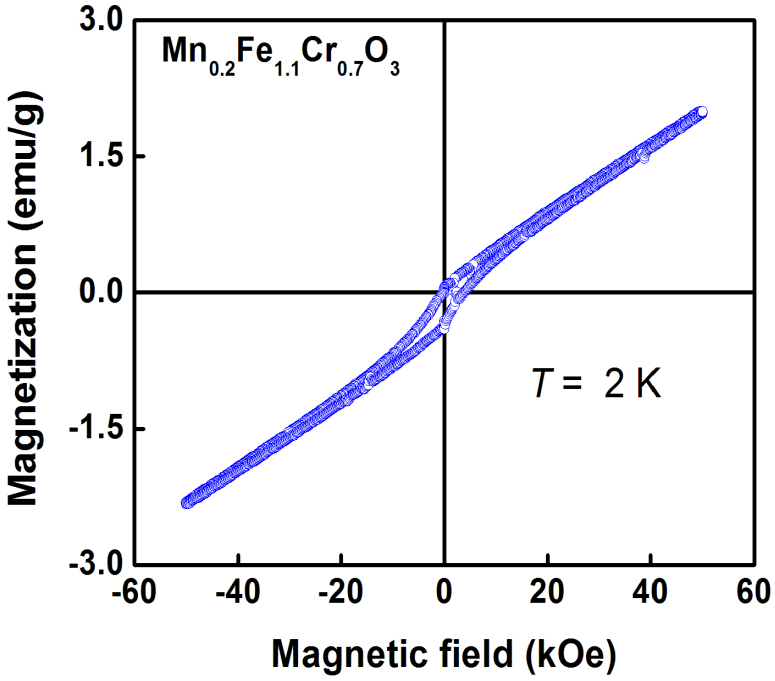

Figure 8.19: Hysteresis loops of $Mn_{0.2}Fe_{1.1}Cr_{0.7}O_3$ measured at 2 K.

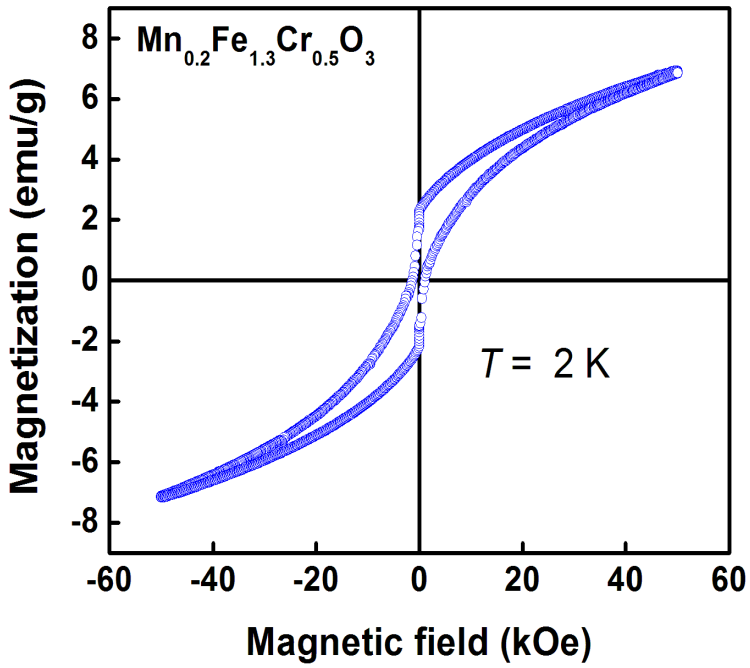

Figure 8.20: Hysteresis loops of $Mn_{0.2}Fe_{1.3}Cr_{0.5}O_3$ measured at 2 K.

There is no more shift in the hysteresis loop for $Mn_{0.2}Fe_{1.3}Cr_{0.5}O_3$ in Figure 8.20. This implies that there is no more interaction between the AFM host and the ferromagnetic clusters compared to Figures 8.18 or 8.19.

8.3.4 Conclusion

We successfully prepared $Mn_{0.2}Fe_xCr_{1.8-x}O_3$ nanoparticle alloys by hydrothermal process. We found much reduced magnetizations for the Mn-based samples compared to Sn-based samples. The composition dependence of the hysteresis loops is not very significant for Mn-based samples. Evidence of successful Mn incorporation into the corundum structure is obtained [20]. The nanoparticle oxides have been found to exhibit exchange bias effects at room temperature which disappear at low temperatures. Strong linear correlation between the exchange bias field H_{EB} with Fe content and particle sizes have been observed. The H_{EB} in the present case disappears at the particle

size of about 34 nm. The exchange bias in the present case arises from the exchange interaction between the AFM host and ferrimagnetic clusters. Mn^{2+} ions which occupy both interstitial and substitutional sites establish ferrimagnetic clusters inside an AFM background. The present findings of exchange bias at room temperature in $Mn_{0.2}Cr_{1.8-x}Fe_xO_3$ samples is interesting and unexpected. The AFM component appears to be more significant at room temperature and less important in the present series of alloys at lower temperature. However, these results are still under investigation in order to provide additional results and explanation.

Chapter 9

Final conclusions and future work

We have investigated the synthesis, structural and magnetic properties of nanosized $Sn_{0.2}Fe_xCr_{1.8-x}O_3$, $Mg_{0.2}Fe_xCr_{1.8-x}O_3$, $Mn_{0.2}Fe_xCr_{1.8-x}O_3$ alloys using X-ray diffraction (XRD), Mössbauer spectroscopy and magnetization measurements. The alloys studied were produced by hydrothermal methods in a reflux vessel and in a pressure reactor. In all samples prepared by hydrothermal process, single phase corundum structure formation as indicated by XRD was incomplete at the initial synthesis temperature of 100 °C and was complete after annealing at 600 °C. In addition, we reduced the size of the $Sn_{0.2}Fe_{1.3}Cr_{0.5}O_3$ alloy using high-energy ball milling.

Significant reductions in magnetization and changes in coercive fields when particle sizes are reduced from about 28 nm to about 17 nm are induced by mechanical milling. The results show transformation from multidomain to single domain structure at a critical size of about 23 nm [158]. The particle sizes of the as-prepared alloys were found between 25.3 and 34.8 nm in $Sn_{0.2}Fe_xCr_{1.8-x}O_3$, 38.8 and 55.6 nm in $Mg_{0.2}Fe_xCr_{1.8-x}O_3$ and 14.2 and 32.8 nm in $Mn_{0.2}Fe_xCr_{1.8-x}O_3$. The particle sizes appear to be sensitive to a particular composition. The magnetic properties derived from magnetization and Mössbauer spectroscopy measurements are sensitive to the microstructure and the doping atoms. The accomodation of tin, magnesium and manganese into the corrundum-related structure did not induce a change in the Fe^{3+} oxidation state of iron.

In the $Sn_{0.2}Fe_xCr_{1.8-x}O_3$ alloys, we find that the general trend for particle sizes for different samples are similar. However, the samples made in a pressure reactor appear to have slightly reduced particle sizes than those made in a glass reflux system. The differences can be attributed to the preparation method. In a pressure reactor, the samples are more homogeneously mixed because stirring continues while the mixtures are heated under pressure. The ability of the samples to form bigger particles seems to be affected by continuous stirring. We also suspect that closer proximity of the reacting ions is achieved in a pressure reactor. The differences in particle size in the two methods is also reflected in the magnetic hyperfine fields. We observe that the samples made in a reflux vessel show higher magnetic hyperfine fields than the samples made in a pressure reactor. These decreasing tendencies of the magnetic hyperfine fields at smaller particle sizes may be due to both the surface effect and the size effect. As the particle size decreases to nanoscale, the volume of the surface atoms is expected to be an appreciable fraction of the total volume and both the small-size effect and the surface effect would perturb the structure and the properties of the nanoparticles [167]. The magnetization curves of $Sn_{0.2}Fe_xCr_{1.8-x}O_3$ with low coercive fields are indicative of the onset of superparamagnetic like-behaviour.

Low temperature measurements in the $Mg_{0.2}Fe_xCr_{1.8-x}O_3$ alloys show evidence of spin freezing as confirmed by zero-field cooling (ZFC) and field cooling (FC) magnetizations measurements. Spin freezing at low temperature appears to be associated with increased magnetic hardness. The linear fits for the temperature dependence of the inverse magnetization show that the samples exhibit Curie-Weiss type behavior. The corresponding extrapolated paramagnetic Weiss temperatures θ_p are -722 K. The large negative values of θ_p indicate that the antiferromagnetic (AFM) interactions in $Mg_{0.2}Fe_xCr_{1.8-x}O_3$ alloys are stronger. Furthermore, shifts of the hysteresis loops along the field axis associated with exchange bias effects [149] are observed at low temperature in $Mg_{0.2}Fe_xCr_{1.8-x}O_3$ samples. The exchange bias in the present case arises from

exchange interaction between the AFM host and ferrimagnetic clusters. There is no correlation between the exchange bias H_{EB} and the iron content x while a strong correlation between H_{EB} and particle size D independent of composition for all samples annealed at 600 °C is observed [21].

After annealing at 700 °C we find significant changes between H_{EB} and D_{XRD}. At first, the H_{EB} increases with decreasing particle size from 66.55 nm ($x = 0.7$) to 44.01 nm ($x = 0.5$) then decreases with further reduction in particle size. However, we still find very strong correlation for samples at $x = 0.5$, 0.3 and 0.7 [168].

In contrast with what has been observed in the $Mg_{0.2}Fe_xCr_{1.8-x}O_3$ alloys, the $Mn_{0.2}Fe_xCr_{1.8-x}O_3$ alloys exhibit exchange bias at room temperature. In this case there is a strong decreasing correlation between the exchange bias and particle sizes. The exchange bias seems also to correlate very well with iron content x [169]. Magnetization measurements show positive exchange interaction with increasing iron content in tin samples while the magnesium and manganese samples collapse the magnetic order.

Our investigations have provided us with useful information on the synthesis, structural, and magnetic properties of nano oxides [20], [21]. Future work can involve the study of $Sn_{0.2}Fe_xCr_{1.8-x}O_3$ samples not measured at low temperature, the chemical disorder by Mössbauer technique and the investigation of the exchange bias phenomenon by magnetoresistance measurements [170].

Bibliography

[1] Dr. Arup Roy. *Nanotechnology in industrial wastewater treatment*, page 5. IWA Publishing, 2015.

[2] A. I. Martinez, M .A. Garcia-Lobato, and D. L. Perry. Study of the properties of iron oxide nanostructures. *Research in Nanotechnology Developments. A. Barranon Editor. Nova Science*, 2009.

[3] C. M. Niemeyer. Nanoparticles, proteins, and nucleic acids: Biotechnology meets materials science. *Angewandte Chemie International Edition*, 40(22):4128–4158, 2001.

[4] A. Kihal, B. Bouzabata, G. Fillion, and D. Fruchart. Magnetic and structural properties of nanocrystalline iron oxides. *Physics Procedia*, 2(3):665–671, 2009. Proceedings of the JMSM 2008 Conference.

[5] M. Faraji, Y. Yamini, and M. Rezaee. Magnetic nanoparticles: Synthesis, stabilization, functionalization, characterization, and applications. *Journal of the Iranian Chemical Society*, 7(1):1–37, 2010.

[6] T.P. Raming, A.J.A. Winnubst, C.M. van Kats, and A.P. Philipse. The Synthesis and Magnetic Properties of Nanosized Hematite α-Fe_2O_3 Particles. *Journal of Colloid and Interface Science*, 249(2):346–350, 2002.

[7] R. Chandra, A. Kumar, D. Kaur, and P. Ayub. Structural, optical and electronic properties of nanocrystalline Tin films. *Nanotechnology*, 16(12):3053, 2005.

[8] R. Chandra, D. Kaur, A. Kumar Chawla, N. Phinichka, and Z.H. Barber. Texture development in Ti–Si–N nanocomposite thin films. *Materials Science and Engineering: A*, 423(1):111–115, 2006.

[9] M. Gheisari, M. Mozaffari, M. Acet, and J. Amighian. Preparation and investigation of magnetic properties of wüstite nanoparticles. *Journal of Magnetism and Magnetic Materials*, 320(21):2618–2621, 2008.

[10] F. Padella, C. Alvani, A. La barbera barbera barbera barbera, G. Ennas, R. Liberatore, and F. Varsano. Mechanosynthesis and process characterization of nanostructured manganese ferrites. *Materials Chemistry and Physics*, 90(1):172–177, 2005.

[11] J. Y. Tang, X. Y. Hu, and Y. C. Zhang. Controllable synthesis and magnetic properties of pure hematite and maghemite nanocrystals from a molecular precursor. *Journal of Alloys and Compounds*, 462(24-28), 2008.

[12] I. Hiroyuki and T. Sugimoto. Systematic control of size, shape, structure, and magnetic properties of uniform magnetite and maghemite particles. *Journal of Colloid and Interface Science*, 265(2):283–295, 2003.

[13] Dale L. Huber. Synthesis, properties, and applications of iron nanoparticles. *Small*, 1(5):482–501, 2005.

[14] H. Andrew Latham and M. Elizabeth William. Controlling Transport and Chemical Functionality of Magnetic Nanoparticles. *Acc. Chem. Res.,*, 41(3):411–420, 2008.

[15] J.E. Greedon. *Magnetic Oxides*. John Wiley & Sons, 1994.

[16] A. S. Teja and K. Pei-Yoong. Synthesis, properties, and applications of magnetic iron oxide nanoparticles. *Progress in Crystal Growth and Characterization of Materials*, 55(1–2):22–45, 2009.

[17] T. Ericsson, A. Krisnhamurthy, and B. K. Srivastava. Morin-Transition in Ti-Substituted Hematite: A Mössbauer Study. *Physica Scripta*, 33(1):88, 1986.

[18] F. Vander Woude. Mössbauer effect in α-Fe_2O_3. *Physica Status Solidi (b)*, 17(1):417–432, 1966.

[19] S.J. Stewart, R.A. Borzi, E.D. Cabanillas, G. Punte, and R.C. Mercader. Effects of milling-induced disorder on the lattice parameters and magnetic properties of hematite. *Journal of Magnetism and Magnetic Materials*, 260(3):447–454, 2003.

[20] K. Mbela, T.Moyo, and J.Z. Msomi. Tin, manganese doped chromium iron oxides of composition α-$Sn_{0.2}Cr_{1.8-x}Fe_xO_3$ and $Mn_{0.2}Cr_{1.8-x}Fe_xO_3$. *Journal of Superconductivity and Novel Magnetism*, 25:2637–2641, 2012.

[21] K. Mbela, T. Moyo, J.Z. Msomi, M. Öztürk, and N. Akdogan. Synthesis and magnetic properties of $Mg_{0.2}Cr_{1.8-x}Fe_xO_3$ nanoparticles. *Journal of Magnetism and Magnetic Materials*, 330(0):159–162, 2013.

[22] *www.webmineral.com.*

[23] www.emeraldinsight.com/content-images.

[24] Y. Kim and T. Hsu. A reflection electron microscopic (REM) study of α-Al_2O_3 (0001) surfaces. *Surface Science*, 258:131–146, 1991.

[25] A. K. Giri, E. M. Kirkpatrick, P. Moongkhamklang, S. A. Majetich, and V. G. Harris. Photomagnetism and structure in cobalt ferrite nanoparticles. *Applied Physics Letters*, 80(13), 2002.

[26] P. C. Morais. Using Mössbauer spectroscopy as a key tecnique in the investigation of nanosized particles for drug delivery. *Hyperfine Interact*, 2008.

[27] Q. Chen and Z. J. Zhang. Size-dependent superparamagnetic properties of $MgFe_2O_4$ spinel ferrite nanocrystallites. *Appl. Phys. Lett*, 73:3156–3158, 1998.

[28] L. Hong-Ling, K. S. Pil, W. Jun-Hua, J. Myung-Hwa, J. H. Min, J. H. Lee, B. H. An, and Y. K. Kim. One-pot polyol synthesis of monosize pvp-coated Fe_3O_4 nanoparticles for biomedical applications. *Journal of Magnetism and Magnetic Materials*, 310(2, Part 3):e815–e817, 2007. Proceedings of the 17th International Conference on Magnetism The International Conference on Magnetism.

[29] C. M. Hurd. Varietes of magnetic order in solids. *Contemporary Phys*, 23(5):469–493, 1982.

[30] M. Hansen, M.F. Kotch, and S. Morup. Magnetic dynamics of weakly and strongly interacting hematite nanoparticles. *Phys. Rev. B*, 62:1123–1135, 2000.

[31] C. Frandsen and S. Morup. Thermoinduced magnetization in nanoparticles of antiferromagnetic materials. *Phys. Rev. Lett*, 94:027202, 2005.

[32] L.T Kuhn, K. Lefmann, C.H.R Bahl, S.N. Ancona, and S. Morup. Neutron study of magnetic excitations in 8 nm α-Fe_2O_3 nanoparticles. *Phys. Rev. B*, 74:184406, 2006.

[33] Z. L. Lu, J. M. Zhu, S. D. Li, X. C. Liu, W. Q. Zou, F. M. Zhang, and Y. W. Du. Magnetic and transport property studies of nanocrystalline $Zn_xFe_{3-x}O_4$. *Solid State Communications*, 137(10):528–532, 2006.

[34] S. Bedanta and W. Kleemann. Superparamagnetism. *Journal of Physics D: Applied Physics*, 42(013001), 2009.

[35] C. Frandsen, L.T Kuhn, K. Lefmann, C.H.R Bahl, B. Lebech, L.T. Keller, and S. Morup. Oriented attachement and exchange coupling of α-Fe_2O_3 nanoparticles. *Phys. Rev. B*, 72:2114406, 2005.

[36] J. Andre-Filho, L. Leon-Felix, and J.A.H. Coaquira. Size dependence of the magnetic and hyperfine properties of nanostructured hematite powders prepared by the ball milling technique. *Hyperfine Interact*, 2013.

[37] L. S. Khim, Z. G. Char, and S. Kim. Synthesis and magnetic studies of uniform iron nanorods and nanospheres. *Journal of the American Chemical Society*, 122(35):8581–8582, 2000.

[38] F. Dumestre, B. Chaudret, C. Amiens, M. Fromen, M. Casanove, P. Renaud, and P. Zurcher. Shape control of thermodynamically stable cobalt nanorods through organometallic chemistry. *Angewandte Chemie International Edition*, 41(22):4286–4289, 2002.

[39] J. K. Srivastava, G. K. Shenoy, and R. P. Sharma. Magnetic structure of Cr_2O_3 - Fe_2O_3 system. *Solid State Communications*, 6(2):73–76, 1968.

[40] J. Rack Sohn and J. Seob Lim. Catalytic properties of $NiSO_4ZrO_2$ promoted with Fe_2O_3 for acid catalysis. *Materials Research Bulletin*, 41(7):1225–1241, 2006.

[41] M.D. Lima, R. Bonadimann, M.J. de Andrade, J.C. Toniolo, and C.P. Bergmann. Nanocrystalline Cr_2O_3 and amorphous Cr_2O_3 produced by solution combustion synthesis. *Journal of the European Ceramic Society*, 26(7):1213–1220, 2006.

[42] N. Apostolescu, B. Geiger, K. Hizbullah, M.T. Jan, S. Kureti, D. Reichert, F. Schott, and W. Weisweiler. Selective catalytic reduction of nitrogen oxides by ammonia on iron oxide catalysts. *Applied Catalysis B: Environmental*, 62(1–2):104–114, 2006.

[43] L. Duk-Dong and C. Dong-Han. Thick-film hydrocarbon gas sensors. *Sensors and Actuators B: Chemical*, 1(1–6):231–235, 1990.

[44] K. vSirok'y, J. Jirevsov'a, and H. Lubom'ir. Iron oxide thin film gas sensor. *Thin Solid Films*, 245(1–2):211–214, 1994.

[45] G. Neri, A. Bonavita, S. Galvagno, P. Siciliano, and S. Capone. CO and NO_2 sensing properties of doped-Fe_2O_3 thin films prepared by LPD. *Sensors and Actuators B: Chemical*, 82(1):40–47, 2002.

[46] H. Kanai, H. Mizutani, T. Tanaka, T. Funabiki, S. Yoshida, and M. Takano. X-ray absorption study on the local structures of fine particles of α-Fe_2O_3-SnO_2 gas sensors. *Journal of Materials Chemistry*, 2(7):703–707, 1992.

[47] C. V. Gopal, W. Cao, O. K. Tan, and W. Zhu. Preparation of Fe_2O_3 (0.9)-SnO_2 (0.1) by hydrazine method: application as an alcohol sensor. *Sensors and Actuators B: Chemical*, 81(2–3):170–175, 2002.

[48] C.A. Barrero, J. Arpe, E. Sileo, L.C. Sanchez, R. Zysler, and C. Saragovi. Ni-and Zn-doped hematite obtained by combustion of mixed metal oxinates. *Physica B: Condensed Matter*, 354(1):27–34, 2004.

[49] D. Christopher, K. Amit Agrawal, C. Erick Walter, and D. Mark Vaudin. Effect of Tin doping on hematite photoanodes for water splitting. *Journal of Physical Chemistry C*, 116(29):15290–15296, 2012.

[50] R. J. Willey, H. Lai, and J. B. Peri. Investigation of iron oxide-chromia-alumina aerogels for the selective catalytic reduction of nitric oxide by ammonia. *Journal of Catalysis*, 130(2):319–331, 1991.

[51] A. Muan and S. Omiya. Phase relations in the system iron oxide Cr_2O_3 in air. *Journal of the American Ceramic Society*, 43(4):204–209, 1960.

[52] Y. Shimizu, S. Kusano, H. Kuwayama, K. Tanaka, and M. Egashira. Oxygen-sensing properties of spinel-type oxides for stoichiometric air/fuel combustion control. *Journal of the American Ceramic Society*, 73(4):818–824, 1990.

[53] D. G. Rancourt, J. E. Dutrizac, G. Lamarche, R. Provencher, and M. Z. Dang. Interplay of surface conditions, particle size, stoichiometry, cell parameters, and magnetism in synthetic hematite-like materials. *Hyperfine Interact*, 117(271), 1998.

[54] C. L. Bruzzone and R. Ingalls. Mössbauer-effect study of the Morin transition and atomic positions in hematite under pressure. *Phys. Rev. B*, 28:2430–2440, Sep 1983.

[55] E. E. Sileo, D. Pérez Daroca, A. César, L. Larralde, S. Mariela, and C. Saragovi. Influence of the genesis on the structural and hyperfine properties of Cr-substituted hematites. *Chemical Geology*, 238(1–2):84–93, 2007.

[56] F. J. Morin. Electrical properties of Fe_2O_3 and α-Fe_2O_3 containing titanium. *Phys. Rev.*, 83:1005–1010, Sep 1951.

[57] M. Watanabe, K. Kaneko, N. Uekawa, and F. Mizukami. Mixed-valence formation in highly oriented Ti-doped iron oxide film. *J. Chem. Soc*, 91:2161, 1995.

[58] P. B. Fabritchnyi, E. V. Lamykin, A. M. Babechkin, and A. N. Nesmeianov. Study of Morin transition by Mössbauer effect in hematite contening Tin impurity. *Solid State Communications*, 11(2):343–348, 1972.

[59] K. Melzer, H. Mehner, F. Schneider, and G. Deke. Mössbauer study of local spin structure in singly substituted YIG ferrites. *Phys. Stat. Sol. (a)*, 39(2):643–650, 1977.

[60] S. Popovic, M. Metikos-Hukovic, S. Music, and G. Gvozdic. X-ray absorption study on the local structures of fine particles of α-Fe_2O_3 gas sensors. *J. Mater. Chem.*, 2:703, 1992.

[61] E. D. Grave, D. Chambaere, and L. H. Bowen. Nature of the Morin transition in Al-substituted hematite. *Journal of Magnetism and Magnetic Materials*, 30(3):349–354, 1983.

[62] S. A. Fysh and P. E Clark. Aluminous hematite: A Mössbauer study. *Physics and Chemistry of Minerals*, 8(6):257–267, 1982.

[63] S. Musić, S. Popović, and M. Ristić. X-ray diffraction and Mössbauer spectra of the system Ga_2O_3. *Journal of Materials Science*, 24:2722–2726, 1989.

[64] M. Risti'c, S. Popovi'c, M. Tonkovi'c, and S. Musi'c. Chemical and structural properties of the system Fe_2O_3-In_2O_3. *Journal of Materials Science*, 26(15):4225–4233, 1991.

[65] M. Takano, Y. Bando, N. Nakanishi, M. Sakai, and H. Okinaka. Magnetic nanoparticles: synthesis, stabilization, functionalization, characterization, and applications. *Journal of Solid State Chemistry*, 68(1):153–162, 1987.

[66] W. Zhu, M.S. Tse, Y. Liu, and S.Y. Shen. Study of new alcohol gas sensors made from ultrafine SnO_2-Fe_2O_3. *Journal of Materials Sciences Letters*, 249(14):1185–1187, 1995.

[67] J. Z. Jiang, R. Lin, K. Nielsen, S. Morup, D. G. Rickerby, and R. Clasen. Interstitial positions of tin ions in α-$FeSn_2O_3$ solid solutions prepared by mechanical alloying. *Phys. Rev. B*, 55(22):14830–14835, 1997.

[68] Frank J. Berry, Örn Helgason, Thomas Moyo, and Xiaolin Ren. Tin doping of α-Cr_2O_3 and α-$(FeCr)_2O_3$. *Materials Letters*, 59(26):3241–3245, 2005.

[69] F.M. Filho, A.Z. Simes, A. Ries, L. Perazolli, E. Longo, and J.A. Varela. Nonlinear electrical behaviour of the Cr_2O_3, ZnO, CoO and Ta_2O_5-doped SnO_2 varistors. *Ceramics International*, 32(3):283–289, 2006.

[70] Arvids Stashans and Soraya Jácome. Local structure, magnetic and electronic properties of N-doped α-Cr_2O_3 from the first-principles. *Computational Materials Science*, 81:353–357, 2014.

[71] K. Zakrzewska. Mixed oxides as gas sensors. *Thin Solid Films*, 391(2):229–238, 2001. Proceedings of the 2nd International Seminar on Semiconductor Gas Sensors.

[72] P. T. Moseley and D. E. Williams. A selective ammonia sensor. *Sensors and Actuators B: Chemical*, 1(1–6):113–115, 1990.

[73] W. Zeng, T. Liu, D. Liu, and E. Han. Hydrogen sensing and mechanism of M-doped SnO_2 nanocomposite. *Sensors and Actuators B: Chemical*, 160(1):455–462, 2011.

[74] I. Ayub, F. J., C. Johnson, D. A. Johnson, E. A. Moore, X. Ren, and H. M. Widatallah. Tin-, titanium-, and magnesium-doped α-Cr_2O_3: characterisation and rationalisation of the structures. *Solid State Communications*, 123(3–4):141–145, 2002.

[75] A. K. Bhattacharya, C. K. Majumdar, D. Chintalapudi, and A. Hartridge. A Mössbauer study of Fe_2O_3-Cr_2O_3 nanocrystals dispersed in a silica matrix. *J. Magn. Magn. Mater.*, 183, 1998.

[76] J. Keränam, P. Vuoristo, T. Mäntylä, S. Virtanen, P. Schmuki, M. Büchler, H. Böhni, and T. Stenberg. Characterisation of r.f. sputtered Fe-Cr-oxide films. *Phys. Lett.*, 52(477), 1999.

[77] F. J. Berry, T. Moyo, and Ö. Helgason. Tin doping of *alpha*-Cr_2O_3 and α-$(FeCr)_2O_3$. *Material Letters*, 59:3241–3245, 2005.

[78] Dynamic periodic table (www.ptable.com) .

[79] A. Lakshman, P. S. V. Subba Rao, and K. H. Rao. Mössbauer spectroscopic analyses of $Mg_{0.9}Mn_{0.1}In_xFe_{2-x}O_4$ spinel ferrites. *Journal of Magnetism and Magnetic Materials*, 284(0):352–357, 2004.

[80] J.M.D. Coey. Magnetism and magnetic materials. *Contemporary Phys*, 52(1), 2011.

[81] A.P. Guimaraes and I.S. Oliveira. *Magnetism and Magnetic Resonance in Solids*. John Wiley and Sons, Chichester, 1998.

[82] S. Chikazumi and S. H. Charap. *Physics of magnetism*. John Wiley and Sons, New York, 1964.

[83] J. Crangle. *The Magnetic Properties of Solids*. Edward Arnold, London, 1977.

[84] H. P. Myers. *Introductory Solid State Physics*. Taylor and Francis Ltd., London, second edition edition, 1997.

[85] A. Abraham. *The Principles of Nuclear Magnetism*, volume p. 161. London-New York: Oxford University Press, Claredon, 1961.

[86] S. Chikazumi. *Physics of ferromagnetism*. Oxford University Press, 2009.

[87] L. Néel. Ferromagnetism and antiferromagnetism. *Annales de Physique (Paris)*, 3:137–138, 1948.

[88] N. A. Spaldin. *Magnetic materials : Fundamentals and applications*. Cambridge University Press, 2010.

[89] M. Jalaly, M. H. Enayati, and F. Karimzadeh. Investigation of structural and magnetic properties of nanocrystalline $Ni_{0.3}Zn_{0.7}Fe_2O_4$ prepared by high energy ball milling. *Journal of Alloys and Compounds*, 480(2):737–740, 2009.

[90] W. C. Nunes, L. M. Socolovsky, E. De Biasi, J. M. Vargas, M. Knobel, and J. C. Deardin. Superparamagnetism and other magnetic features in granular materials: a review on ideal and real systems. *J. Nanosci. Nanotechnol*, 8:2836, 2008.

[91] S. P. Gubin. *Magnetic Nanoparticles*. WILEY-VCH Verlag, Weinheim, 2009.

[92] E. Manova, B. Kunev, D. Paneva, I. Mitov, L. Petrov, C. Estournès, C. D'Orléan, J. L. Rehspringer, and M. Kurmoo. Mechanochemical synthesis and character-

ization of nanodimensional iron-cobalt spinel oxides. *Chemistry of Materials*, 16(26):5689–5696, 2004.

[93] M. Sertkol, Y. Köseoğlu, A. Baykal, H. Kavas, and A. C. Başaran. Synthesis and magnetic characterization of $Zn_{0.6}Ni_{0.4}Fe_2O_4$ nanoparticles via a polyethylene glycol-assisted hydrothermal route. *Journal of Magnetism and Magnetic Materials*, 321(3):157–162, 2009.

[94] S. R. Elliott. *The Physics and Chemistry of Solids*. John Wiley and Sons, England, 1998.

[95] J. N. Chapman and K. J. Kirk. *Magnetic Hysteresis in Novel Magnetic Materials*, volume 338. Springer Netherlands, 1997.

[96] T. Moyo. *T. Moyo, Lectures notes in Magnetism, University of KwaZul-Natal*.

[97] W. F. Brown. Criterion for uniform micromagnetization. *Phys. Rev.*, 105:1479–1482, Mar 1957.

[98] J. Nogués, J. Sort, V. Langlais, V. Skumryev, S. Suriñach, J.S. Muñoz, and M.D. Baró. Exchange bias in nanostructures. *Physics Reports*, 422(3):65–117, 2005.

[99] K. Woo, J. Hong, S. Choi, H. W. Lee, J. P. Ahn, C. S. Kim, and S. W. Lee. Easy synthesis and magnetic properties of iron oxide nanoparticles. *Chemistry of Materials*, 16(14):2814–2818, 2004.

[100] J. Nogués, C. Leighton, and Ivan K. Schuller. Correlation between antiferromagnetic interface coupling and positive exchange bias. *Phys. Rev. B*, 61:1315–1317, Jan 2000.

[101] N. C. Koon. Calculations of exchange bias in thin films with ferromagnetic/antiferromagnetic interfaces. *Phys. Rev. Lett.*, 78:4865–4868, Jun 1997.

[102] J. Noguès, C. Leighton, and Ivan K. Schuller. Exchange bias. *Journal of Magnetism and Magnetic Materials*, 192(2):203–232, 1999.

[103] D. Paccard. A new property of ferromagnetic-antiferromagnetic coupling. *Stat. Solidi*, (16):301, 1966.

[104] T. C. Gibbs. *Principles of Mössbauer spectroscopy*, volume 159 of *p.22-43*. Chapman and Hall, London, 1976.

[105] G. Burns. *Solid State Physics*, volume 599 of *p.564-594*. Academic Press, London, 1985.

[106] N. N. Greenwood and T. C. Gibbs. *Mössbauer Specroscopy*, volume 46 of *p.1-25*. Chapman and Hall, London, 1971.

[107] V. Wigner and E. Z. Weisskopf. Deutsche gesellschaft für tecnische physik. *Physik*, 63(54), 1930.

[108] H.R. Verma. *Atomic and Nuclear Analytic Methods*, volume 46. Springer, 2007.

[109] M. A. Amer and O. M. Hemeda. Mössbauer and infrared studies of the system $Co^{57}Cd_{1-x}Fe_xO_{24}$. *Hyperfine Interactions*, 96(1):99–109, 1995.

[110] X. M. Lin and A. C. S. Samia. Synthesis, assembly and physical properties of magnetic nanoparticles. *Journal of Magnetism and Magnetic Materials*, 305(1):100–109, 2006.

[111] *www.parrinst.com.*

[112] *www.retsch.com.*

[113] R. H. Jenkins and B. de Vries. *Worked examples in X ray spectrometry*, pages 124–126, 1970.

[114] JCPDS, USA. *Mineral Powder Diffraction File, JCPDS*, 1980. p. 590.

[115] K. Thomas. *Lecture note on Practical X-Ray Diffraction, School of Materials Engineering, Purdue University Indiana.*

[116] B.D. Cullity and S.R. Stock. *Elements of X-ray diffraction.* Prentice-Hall Inc, 2001. p. 167-171.

[117] L. B. McCusker. *Journal of Applied Crystallography*, 32:36–50, 1999.

[118] R. F. Egerton. *Physical Principles of Electron Microscopy: An Introduction to TEM, SEM and AEM.* Springer, New York, USA, 2005. p. 1-16.

[119] *http://cnx.org/content/m22963/1.5/.*

[120] C. G. Shull, W. A. Strauser, and E. O. Wollan. Neutron diffraction by paramagnetic and antiferromagnetic substances. *Phys. Rev.*, 83:333–345, Jul 1951.

[121] Recoil: Mössbauer Spectral Analysis Software for Windows. Version 1.0 by Ken Lagarec under direction of Professor G. Rancourt. Department of Physics. University of Ottawa.

[122] W. Burgei, M. J. Pechan, and H. Jaeger. A simple vibrating sample magnetometer for use in a materials physics course. *American Journal of Physics*, 71(8):825–828, 2003.

[123] S. R. Hoon and S. N. M. Willcock. The design and operation of an automated double-crank vibrating sample magnetometer. *Journal of Physics E: Scientific Instruments*, 21(8):772, 1988.

[124] Lake Shore Cryotronics USA (www.lakeshore.com) Lake Shore 7300 Series VSM Software.

[125] C. Shanshan, F. Kang, X. yang yang yang yang, and Z. Zhen. Influence of Al substitution on magnetism and adsoption properties of hematite. *Journal of Solid State Chemistry*, 228(2):82–89, 2015.

[126] W. Zhong, S. Yang, Z. Yu, X. Liu, Y. Du, and B. Gu. Influence of La^{3+} substitution of the structure and magnetic properties of M-type strontium ferrites. *Journal of Magnetism and Magnetic Materials*, 238(207), 2002.

[127] A. Mumtaz, S. K. Hasanain, K. Maaz, and A. Ceylan. Synthesis and magnetic properties of cobalt ferrite nanoparticles prepared by wet chemical route. *Journal of Magnetism and Magnetic Materials.*, 308(2):289–295, 2007.

[128] S. Singhal, S. K. Barthwal, and K. Chandra. Structural, magnetic and Mossbauer spectral studies of nanosize aluminium substituted Nickel-zinc ferrites. *Journal of Magnetism and Magnetic Materials*, 296(2):94–103, 2006.

[129] M. Grigorova, H.J. Blythe, V. Blaskov, V. Rusanov, V. Petkov, V. Masheva, D. Nihtianova, Ll.M. Martinez, J.S. Muñoz, and M. Mikhov. Magnetic properties and Mössbauer spectra of nanosized $CoFe_2O_4$ powders. *Journal of Magnetism and Magnetic Materials*, 183(1–2):163–172, 1998.

[130] T. D. Shen, R. B. Schwarz, and J. D. Thompson. Soft magnetism in mechanically alloyed nanocrystalline materials. *Phys. Rev. B*, 72:014431, Jul 2005.

[131] K. Malviya, D. Kirtiman, and H. Dotan. Systematic comparison of different dopants in thin film hematite photoanodes for solar water splitting. *J. Mater. Chem. A,*, 4(8):3091–3099, 2016.

[132] F. J. Berry, C. Greaves, J. G. McManus, M. Mortimer, and G. Oates. An investigation of the local environments of tin-doped α-Fe_2O_3. *Journal of Solid State Chemistry*, 130(2):272–276, 1997.

[133] F. J. Berry, C. Greaves, Ö. Helgason, J. McManus, H. M. Palmer, and R. T. Williams. Structural and magnetic properties of Sn-, Ti-, and Mg-substituted α-Fe_2O_3: A study by neutron diffraction and Mössbauer spectroscopy. *Journal of Solid State Chemistry*, 151(2):157–162, 2000.

[134] L. W. Finger and R.M. Hazem. Crystal structure and isothermal compression of Fe_2O_3, Cr_2O_3 and V_2O_3. *Journal of App. Physics*, 51:5362–5367, 1980.

[135] T.K. Nguyen Thanh, N. Maclean, and S. Mahiddine. Mechanisms of nucleation and growth of nanoparticles in solution. *Chemical Reviews*, 114(15):7610–7630, 2014. PMID: 25003956.

[136] Ilka-Marina Grabs, Christian Bradtmöller, Dirk Menzel, and Georg Garnweitner. Formation mechanisms of iron oxide nanoparticles in different nonaqueous media. *Crystal Growth & Design*, 12(3):1469–1475, 2012.

[137] Y.W. Duan, X.L. Kou, and J.G. Li. Size dependence of structure and magnetic properties of $La_{0.7}Sr_{0.3}MnO_3$ nanoparticles. *Physica B: Condensed Matter*, 355(1–4):250–254, 2005.

[138] A. Mumtaz, S. K. Hasanain, K. Maaz, and A. Ceylan. Synthesis and magnetic properties of cobalt ferrite nanoparticles prepared by wet chemical route. *Journal of Magnetism and Magnetic Materials.*, 308:1907–1911, 2007.

[139] Lone, A. Gaffar, and R.N. Bhowmik. Effect of magnetic spins flipping process on the dielectric properties of $\alpha Fe_{1.6}Ga_{0.4}O_3$. *AIP Advances,*, 5, 2015.

[140] N. Kumari, V. Kumar, and S.K. Singh. Chemical synthesis and magnetic investigations on Cr^{3+} substituted Zn-ferrite superparamagnetic nano-particles. *Ceramics international,*, 41(1):1907–1911, 2015.

[141] J. Msomi and T. Moyo. Effect of domain transformation on the magnetic properties of $Cu_xNi_{1-x}Fe_2O_4$ ferrites. *Journal of Magnetism and Magnetic Materials*, 321(9):1246–1250, 2009.

[142] C. Otero and E. Garcia. Crystal chemistry of cadmium-zinc ferrites. *J. Solid State Chem*, 77:275, 1988.

[143] E.C. Sousa, M.H. Sousa, and G.F. Goya. Mossbauer spectroscopy in nickel ferrite nanoparticles. *Journal of Magnetism and Magnetic Materials.*, 272:175, 2004.

[144] C. Cannasc, G. Concasa, D. Gatteschib, A. Falquia, A. Musinuc, G. Piccaluga, C. Sangregoriob, and G. Spanoa. Mossbauer investigation of γ-Fe_2O_3 nanocrystals in silica matrix prepared by sol-gel method. *Journal of Physical Chemistry*, 3(832), 2001.

[145] L. Diandra, L. Pelecky, and R. D. Rieke. Magnetic properties of nanostructured materials. *Chemistry of Materials*, 8(8):1770–1783, 1996.

[146] J. M. D. Coey. Noncollinear spin arrangement in ultrafine ferrimagnetic crystallites. *Phys. Rev. Lett.*, 27:1140–1142, Oct 1971.

[147] R. H. Kodama, A. E. Berkowitz, J. E. J. McNiff, and S. Foner. Surface effects in magnetic nanoparticles. *Phys. Rev. Lett.*, 77:394–397, Jul 1996.

[148] D. Kluwer. *Surface Effects in Magnetic Nanoparticles*. 2005.

[149] W. H. Meiklejohn and C. P. Bean. New magnetic anisotropy. *Phys. Rev.*, 102:1413–1414, Jun 1956.

[150] M. Özturk, R.Topkaya, S.Kazan, N. Akdŏgan, M. Obaida, K. Westerholt, and E. Demirci. Effect of exchange bias on magnetic anisotropies in Fe/CoO bilayers. *Journal of Superconductivity and Novel Magnetism*, 25(8):2597–2603, 2012.

[151] X. H. Huang, J. F. Ding, G. Q. Zhang, Y. Hou, Y. P. Yao, and X. G. Li. Size dependent exchange bias in $La_{0.25}Ca_{0.75}MnO_3$. *Phys. Rev. B*, 78:224408, Dec 2008.

[152] D. Fiorani, L. Del Bianco, A. M. Testa, and K. N. Trohidou. Exchange bias in Co nanoparticles embedded in an Mn matrix. *Journal of magnetism and magnetic materials*, 316(2):155–158, 2007.

[153] M. Gruyters. Surface structure of ultrafin Fe films on Cu(001) revisited. *Phys. Rev. Lett.*, 95:077204, Aug 2005.

[154] C. Martínez-Boubeta, K. Simeonidis, M. Angelakeris, N. Pazos-Pérez, M. Giersig, A. Delimitis, L. Nalbandian, V. Alexandrakis, and D. Niarchos. Critical radius for exchange bias in naturally oxidized Fe nanoparticles. *Physical Review B*, 74(5):054430, 2006.

[155] W. Luo and F. Wang. *Appl. Phys. lett*, 90, 2007.

[156] D. Niebieskikwiat and M. B. Salamon. Intrinsic interface exchange coupling of ferromagnetic nanodomains in a charge ordered manganite. *Phys. Rev. B*, 72:174422, Nov 2005.

[157] T. Zhang, T. F. Zhou, T. Qian, and X. G. Li. Inorganic nanowires: Applications, properties and characterization. *Phys. Rev. B*, 76:174415, Nov 2007.

[158] K. Mbela, T. Moyo, and J.Z. Msomi. Magnetic studies of $Sn_{0.2}Cr_{1.8-x}Fe_xO_3$ compounds prepared via the hydrothermal route. *Journal of Magnetism and Magnetic Materials*, 385(0):282–285, 2015.

[159] N. Moutis, C. Christides, I. Panagiotopoulos, and D. Niarchos. Exchange coupling properties of $La_{1-x}Ca_xMnO_3$ ferromagnetic/antiferromagnetic multilayers. *Phys. Rev. B*, 64:094429, Aug 2001.

[160] T. Moyo. Pressure and temperature variation of coercive field in Fe-rich FeZr amorphous alloys. *Journal of Magnetism and Magnetic Materials*, 154(2):201–206, 1996.

[161] A. Ślawska-Waniewska, P. Didukh, J.M. Greneche, and P. C. Fannin. Mossbauer and magnetisation studies of $CoFe_2O_4$ particles in a magnetic fluid. *Journal of Magnetism and Magnetic Materials*, 215–216(0):227–230, 2000.

[162] H. Hiroyoshi and K. Fukamichi. Spin-glass-like behavior in a Fe-Zr amorphous alloy. *Physics Letters A*, 85(4):242–244, 1981.

[163] R. Malik, S. Annapoorni, S. Lamba, V. Raghavendra Reddy, A. Gupta, P. Sharma, and A. Inoue. Mossbauer and magnetic studies in nickel ferrite nanoparticles: Effect of size distribution. *Journal of Magnetism and Magnetic Materials*, 322(23):3742–3747, 2010.

[164] H. M. I. Abdallah and T. Moyo. Structural and magnetic properties of $Sr_{0.5}Co_{0.5}Fe_2O_4$ nanoferrite. *Journal of Alloys and Compounds*, 562(0):156–163, 2013.

[165] J. Löffler, W. Wagner, H. Van Swygenhoven, and A. Wiedenmann. Nanoscale characterization of magnetic properties in nanostructured Fe, Ni and Co by small angle neutron scattering. *Nanostructured Materials*, 9(1–8):331–334, 1997.

[166] R. H. Kodama. Magnetic nanoparticles. *Journal of Magnetism and Magnetic Materials*, 200(1–3):359–372, 1999.

[167] X. J. Huang, H. S. Im, D. H. Lee, H. S. Kim, and Y. K. Choi. Ferrocene functionalized single-walled carbon nanotube bundles. Hybrid interdigitated construction film for l-glutamate detection. *The Journal of Physical Chemistry C*, 111(3):1200–1206, 2007.

[168] K. Mbela, T. Moyo, and S.E Nadir Osman. Effects of annealing on exchange bias in $Mg_{0.2}Fe_xCr_{1.8-x}O_3$ compounds prepared via the hydrothermal route. *Submitted.*

[169] K. Mbela, T. Moyo, M. Öztürk, and N. Akdoǵan. Magnetic studies of $Mn_{0.2}Fe_xCr_{1.8-x}O_3$ compounds prepared via the hydrothermal route. *Submitted.*

[170] L.C.C.M. Nagamine, J.E. Schmidt, M.N. Baibich, E.B. Saitovitch, and J. Geshev. Field-dependent anisotropic magnetoresistance and magnetization measurements

of NiFe/FeMn exchange-biased bilayers. *Physica B: Condensed Matter*, 384(1–2):132–134, 2006. LAW3M-05Proceedings of the Seventh Latin American Workshop on Magnetism, Magnetic Materials and their Applications.